Material Development of Mixed Conducting Electrodes for Protonic Solid Oxide Electrolysis Cells

プロトン固体酸化物水蒸気電解セルに用いる混合伝導性電極の材料開発

Hajime Toriumi

Graduate School of Chemical Sciences and Engineering
Hokkaido University

September 2022

Table of contents

Chapter 1

General Introduction

Chapter 2

Evaluation of protonic solid oxide steam electrolysis cell with Zr-rich side $BaZr_{0.6}Ce_{0.2}Y_{0.2}O_{3-\delta}$ electrolyte

Chapter 3

Efficient anode based on high-valence-state manganate(V) $Ba_3Mn_2O_8$

Chapter 4

Hydrogen permeable cathode of barium indate zirconate perovskite oxyhydride with enhanced hydride ion conductivity

Chapter 5

H-SOEC using $BaZr_{0.5}In_{0.5}O_{2.25}H_{0.5}$ oxyhydride cathodes

Chapter 6

Chapter 1

General Introduction

1.1. Climate change due to global warming and its effects

Climate change is one of the most severe and urgent problems for human society in the 21st century. Its leading cause is the increase in global average temperature due to anthropogenic greenhouse gas (GHG) emissions such as CO_2, CH_4, and N_2O [1]. Global energy consumption has increased due to growing population and economies in recent years. According to the International Energy Agency (IEA), global energy consumption is estimated to increase by about 30% by 2030 compared to 2016 [2]. However, since most energy sources today rely on fossil fuels such as coal, oil, and natural gas, GHG emissions associated with fossil fuel consumption have increased dramatically since the Industrial Revolution, and this has led to the emergence of abnormal weather on a global scale, which has begun to cause severe damage around the world. The international panel on climate change (IPCC) reported in IPCC Fifth Assessment Report (AR5) in 2014 that there is no doubt that the increase in GHG concentrations observed since the Industrial Revolution around 1750 was caused by human activity [1]. At the same time, the report stated that the scenario without measures to reduce GHG emissions would result in a 3.2-5.5°C increase by the end of the 21st century compared to the 1850-1900 period, with a high likelihood of severe, widespread, and irreversible impacts on people and ecosystems through extreme weather events, ocean acidification, and sea-level rise [1]. Since 2011, atmospheric concentrations have continued to increase, reaching annual average values of 410 ppm for carbon dioxide (CO_2), 1866 ppb for methane (CH_4), and 332 ppb for dinitrogen monoxide (N_2O) in 2019. The 47% increase in CO_2 concentrations and 156% increase in CH_4 concentrations relative to 1750 were reported to far exceed the natural variability of several thousand years of glacial-interglacial periods over at least the past 800,000 years [3].

To reduce climate change, the Paris Agreement, involving 195 nations, was adopted at the 2015 United Nations Climate Change Conference, namely the 21st conference of parties (COP21); “Holding the increase in the global average temperature to well below 2°C above pre-industrial levels and to pursue efforts to limit the temperature increase to 1.5°C above pre-industrial levels, recognizing that this would significantly reduce the risks and impacts of climate change”. Subsequently, the IPCC's 2018 report "Global Warming 1.5°C" showed that limiting global warming to 1.5°C compared to 2°C would significantly reduce climate-related risks. However, it also showed that even if the temperature eventually settles down to +1.5°C, once the average temperature rises by more than 2°C during that period, i.e., overshoots, the irreversible ecological, human, and social impacts would be severe. Unfortunately, the anthropogenic increase in global average temperature from 1850-1900 to 2010-2019 is estimated to be about 1°C [0.8°C-1.3°C], and global warming is likely to reach 1.5°C between 2030 and 2052 if it continues to increase at the current rate of progress [4].

To limit global warming, cumulative global anthropogenic GHG emissions since pre-industrial times, generally quantified as CO_2-equivalent ones (Gt_{CO2}-eq) that include non-CO_2 contributions, must be kept down within a specific total carbon budget [5]. After 2018, the residual carbon budget to limit to 1.5°C is estimated to be approximately 420-580 Gt_{CO2}-eq [4] but is currently consumed at the rate of 52.4 Gt_{CO2}-eq/year, which was the annual GHG emissions in 2019 [5]. Therefore, to limit global warming to 1.5°C without overshooting or with limited overshooting, global GHG emissions must be reduced urgently and dramatically. This would be equivalent to reducing GHG emissions to 25-30 Gt_{CO2}-eq by 2030, a 40-50% reduction from 2010 levels (49 ± 4.5 Gt_{CO2}-eq/year), and to net-zero by around 2050 [4].

In recent years, many countries worldwide have adopted "zero GHG emissions by 2050" as legislation, bills, or policy documents to address this issue. Japan also declared carbon neutral by 2050 in October 2020 and has set a goal of reducing GHG emissions by 46% from the 2013 level by 2030. Furthermore, in May 2021, the revised Law Concerning the Promotion of the Measures to Cope with

Global Warming was enacted, which stipulates "the realization of a decarbonized society by 2050" as its fundamental principle.

1.2 Production of hydrogen

Hydrogen is an important raw material in the chemical industry. Pure hydrogen is in demand worldwide as a raw material for petroleum refining and ammonia production (mainly for fertilizer) at a rate of 70 million tons hydrogen (Mt_{H2}) in 2018 [6]. In addition, there is another demand for 45 Mt_{H2} used as a part of a mixed gases, such as synthesis gas, for fuel or feedstock. The main applications for hydrogen synthesis gas are methanol production and steel production. However, most pure hydrogen is currently produced by steam reforming or partial oxidation of fossil fuels. Natural gas accounts for about 75% of the world's annual hydrogen production of about 70 Mt_{H2}, using about 25 billion cubic metre of natural gas (6% of global natural gas use) [6]. Next comes coal, which plays a dominant role in China. Coal is estimated to account for 23% of global hydrogen production, using 107 Mt of coal (2% of global coal use). Thus, because of the heavy dependence on natural gas and coal, current hydrogen production emits large amounts of carbon dioxide. Natural gas emits 10 tons of carbon dioxide per ton of hydrogen (t_{CO2}/t_{H2}), petroleum products 12 t_{CO2}/t_{H2}, and coal 19 t_{CO2}/t_{H2} [6]. The CO_2 emissions associated with hydrogen production are approximately 830 Mt_{CO2}/year, equivalent to approximately 3% of global CO_2 emissions [7]. Hydrogen produced in these ways is called "gray hydrogen" due to CO_2 emissions during its production.

On the other hand, water electrolysis is an electrochemical process that splits water into hydrogen and oxygen, and when renewable energy is used, the CO_2 emissions associated with hydrogen production are zero. Therefore, this type of hydrogen is called "green hydrogen" because no CO_2 emissions are involved in the hydrogen production process. Hydrogen production by water electrolysis accounts for less than 0.1% of global hydrogen production in 2018 [6]. If all current hydrogen production processes could be replaced by water electrolysis, it would reduce global CO_2 emissions by 3%.

Hydrogen is also expected to be a next-generation energy source because hydrogen can be transported and stored without environmental impact and do not emit CO_2 during the utilization phase. Producing hydrogen using water electrolysis as a flattening and storage technology for renewable energy and using it for power generation could contribute to the realization of a power generation system without CO_2 emissions in the future. Furthermore, if this could be achieved, it would reduce 13 Gt_{CO2}/year emissions from coal- and gas-fired power generation, which amounts to ~38% of the total CO_2 emissions of 33.5 Gt_{CO2}/year in 2018 [8]. Therefore, it is essential to construct power-to-gas technology to convert renewable energy into hydrogen in a highly efficient and economical way in order to achieve zero GHG emissions in near future.

1.3. High-temperature steam electrolysis

Water electrolysis has been attracting attention as a power-to-gas technology in recent years, which enables producing hydrogen fuels by means of renewable energy without CO_2 emission. Three methods are technologically viable: (1) alkaline water electrolysis (AWE), (2) polymer electrolyte (proton exchange) membrane (PEM) or anion-exchange membrane (AEM) water electrolysis, and (3) solid oxide steam electrolysis. (SOE). Methods (1) and (2) are performed with liquid water near room temperature, while method (3) is performed with steam gas at high temperatures. The features of these three processes are summarized in Table 1-1. Since the discovery of the electrolytic phenomenon by Troostwijk and Diemann in 1789 [9], alkaline water electrolysis has matured sufficiently as a hydrogen production technology up to the megawatt level and nowadays is the most widely-used at the commercial level [10]. Meanwhile, alkaline water electrolysis has some issues: intermixing of gaseous products, limited current density and low operating pressure. PEM electrolysis cells is also commercial electrolysis technology as is the case with AWE, whereas the former can yield much higher current densities than latter. Moreover, PEM electrolysis avoids intermixing of cathode and anode gases and thus produces high purity hydrogen [11]. The largest drawbacks of PEM electrolysis are a use of amounts of Pt metal catalysts in both the anode and cathode [12], which hinders its application in the

industrial level. AEM electrolysis has been known to achieve the much higher current than PEM electrolysis at relatively low potentials. The champion data of the AEM has recently been reported to gain an electrolysis current of 7.68 A cm^{-2} at 2.0 V with the cell comprising poly(fluorenyl-*co*-terphenyl piperidinium)-base polymer electrolyte membrane and Pt/C cathode and IrO_2 anodes [13]. Pt-free electrodes such as Ni-Fe alloys and $NiFe_2O_4$ can be applicable for AEM electrolysis, because transition metals are not corroded by basic polymer electrolyte, unlike the case of acidic NAFION polymer electrolyte. The electrolysis currents of AEM cells have been still limited to 0.2-0.8 A cm^{-2} even at 1.8 V bias. Furthermore, the stability of the trimethylamine-base polymer electrolyte is not high because the trimethyl ammonium functional groups of anion exchange polymer is not thermodynamically stable under high electrochemical potential [13,14]. Hence, most of the cell has been reported to be persistent only for 100-200 h electrolysis and there exist only few reports for the durability exceeding 1000 h [13-16]. The durability times are much shorter than those of other system (about 10,000-90,000 h).

Table 1-1 Features of various electrolysis methods [17-21].

	Room temperature liquid electrolysis			High temperature Solid oxide steam Electrolysis (SOE)	
	(1)	(2)		(3)	
	Alkaline Electrolysis Cell (AWEC)	Polymer Electrolyte Membrane Electrolysis Cell (PEMEC)	Anion Exchange Membrane Electrolysis Cell (AEMEC)	Oxide-ionic Solid Oxide steam Electrolysis Cell (O-SOEC)	Protonic Oxide steam Electrolysis Cell (H-SOEC)
Charge carrier	OH^-	H^+	OH^-	O^{2-}	H^+
Electrolyte	Aqueous KOH/NaOH (20–40 wt%)	Proton exchange ionomer	Anion exchange ionomer	Ceramic (YSZ)	Proton conducting Ceramic
temperature	60-80°C	50-80°C	50-80°C	700-1000°C	400-700°C
Anodic reaction (OER)	$2OH^- \rightarrow 1/2O_2 + H_2O + 2e^-$	$H_2O \rightarrow 1/2O_2 + 2H^+ + 2e^-$	$2OH^- \rightarrow 1/2O_2 + H_2O + 2e^-$	$O^{2-} \rightarrow ½\ O2 + 2e^-$	$H_2O \rightarrow 1/2O_2 + 2H^+ + 2e^-$
Anode materials	Ni, Ni–Co alloys	RuO_2, IrO_2,	Ni, Fe, Co oxides, (IrO_2)	Perovskite-type O^{2-}/e^- conductor	$H^+/O^{2-}/e^-$ triple conductor
Cathodic reaction (HER)	$2H_2O + 2e^- \rightarrow H_2 + 2OH^-$	$2H^+ + 2e^- \rightarrow H_2$	$2H_2O + 2e^- \rightarrow H_2 + 2OH^-$	$H_2O + 2e^- \rightarrow H_2 + O^{2-}$	$2H^+ + 2e^- \rightarrow H_2$
Cathode materials	Ni, Ni–Mo alloys	Pt/C	Ni and Ni-Fe alloys, (Pt/C)	Ni-YSZ	Ni-ceramics cermet
Applicability	Commercial	Commercial	Laboratory scale	Demonstration	Laboratory scale
Advantage	Low capital cost, Mature technology	Compact design, Fast response / start-up, High-purity H	Low cost due to using non-Pt group metal, High-purity H	Enhanced kinetics, thermodynamics: lower energy demand, Low capital cost, High energy efficiency	
Disadvantage	Corrosive electrolyte, Gas permeation, Slow dynamics	High cost, Noble-metal utilization, Acidic	Low performance and durability	Mechanically unstable electrodes (cracking), Safety issues: improper sealing	

This thesis focuses on hydrogen production by method (3), i.e., SOE because of the great advantages on thermodynamic and kinetic aspects, as mentioned below.

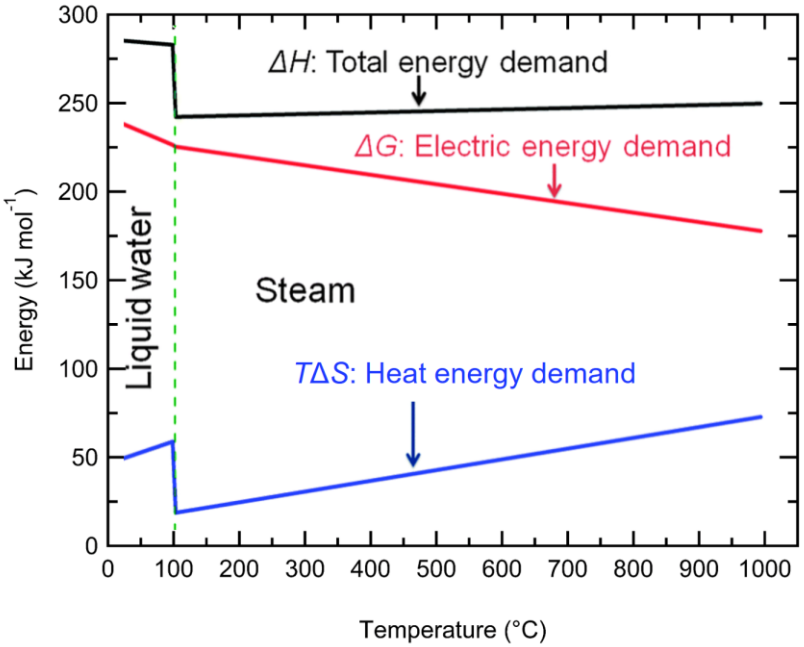

Figure 1-1. Electric, heat and total energy demand for H_2O electrolysis as a function of temperature, showing the electric energy demand decreasing considerably which is compensated by the heat energy with increasing working temperatures.

Figure 1-1 shows the temperature dependence of the thermodynamic parameters for water splitting reaction (1-1).

$$H_2O \rightarrow H_2 + 1/2O_2 \qquad (1\text{-}1)$$

The total energy demand, i.e., the standard enthalpy of reaction (Δ_rH) abruptly drops at below and above 100°C, attributed to the enthalpy of vaporization ($\Delta_{vap}H$). Δ_rH tends to increase with increasing temperature in the range above 100°C, because the heat term, i.e., $T\Delta_rS$ increases with temperature. Δ_rS is the standard entropy of reaction. Therefore, the standard Gibbs energy of reaction (Δ_rG) decrease

with increasing temperature. The standard electrochemical potentials (E) required for water splitting reaction (1-1) is represented with $\Delta_r G$ as follows.

$$E = \Delta_r G / zF \tag{1-2}$$

Where z is the number of electrons involved per reaction for the electrolysis reaction (z is equal to 2 in the case of Equation (1-1)), and F is Faraday's constant (96485 C mol^{-1}). Hence E is lowered with increasing temperature according to the relationship of E and $\Delta_r G$ in Equation (1-2) [22].

$\Delta_r G$ of Equation (1-1) is 237.2 kJ mol^{-1} at 25°C, so that the standard potential of water electrolysis by Equation (1-1) is calculated to 1.23 V. The thermal neutral voltage (E_{ne}) of water electrolysis can be calculated with $\Delta_r H$ by Equation (1-3), resulting in 1.48 V (denoted as $E_{ne,\ water}$) at 25°C.

$$E_{ne} = \Delta_r H / zF \tag{1-3}$$

The electron charge transfer process needs to be activated with electrical potentials, so that the overpotentials are required to promote the reactions in the cathode and anode. For room temperature water electrolysis, a voltage of over 1.6 V must be applied from an external power supply to yield electrolysis current of 1 A cm^{-2} with precious metal electrocatalysts [23].

High temperature SOE apparently has some thermodynamic advantages in comparison to room temperature water electrolysis. $\Delta_r H$ of steam electrolysis is lower than that of water electrolysis by about 40 kJ mol^{-1} due to the contribution of $\Delta_{vap} H$ (Figure 1-1), so that E_{ne} of the former, equaling to 1.28 V (denoted as $E_{ne,\ steam}$) at 600°C, is smaller than that of the latter by about 0.2 V. The contribution of the heat energy demand $T\Delta S$ increases and thus the minimal electrochemical energy demand ($\Delta_r G$) decreases with the temperatures according to the relationship of Equation (1-4), as displayed in Figure 1-1.

$$\Delta H = T\Delta S + \Delta G \tag{1-4}$$

Hence, SOE can produce green hydrogen with much lower electrochemical potential than water electrolysis near room temperature if there exist sufficient heat sources to supply the heat energy for

$T\Delta_r S$ and $\Delta_{vap}H$. The cathode and anode overpotentials of SOE are much lower than those of conventional liquid water electrolysis, because the electrode reactions are significantly activated at elevated temperatures. In fact, SOE cells (SOECs) do not need precious metal catalysts [24,25]. SOECs based on a transition metal oxide electrolyte and electrode can yield 1.0 A cm^{-2} near $E_{ne,\ steam}$ (1.3 V) at 600°C [24]. The heat for $\Delta_{vap}H$ can be supplied by waste feats at industry, nuclear plants, incinerator plant and so on, and the heat corresponding to $T\Delta_r S$ is utilized to keep the operation temperature. These features suggest that SOECs is industrially-feasible technology to produce green hydrogen with an assist of heat energy.

Figure 1-2 shows the summary for the relationship between the voltage and electrolysis currents of AWEC, PEMEC, AEMEC, and SOEC. Room temperature water electrolysis (AWEC, PEMEC, AEMEC) requires much higher voltages than $E_{ne,\ water}$ (1.48 V) due to the large electrode overpotential. Consequently, the efficiency given by the ratio of actual electrolysis voltage to $E_{ne,\ water}$ is less than 70% [6] (Table 1-2). In contrast, SOECs can conduct electrolysis at around $E_{ne,\ steam}$ (~1.3 V) with sufficiently high currents (> 1 A cm^{-2}), thereby achieving the efficiency of more than 90% [26]. Based on the relatively low electrolysis voltage, the electricity consumption per kg of hydrogen results in 35−55 kWh kgH_2^{-1}f for SOECs, which is smaller than the values of 50−83 kWh kgH_2^{-1} for water electrolysis [27] (Table 1-2).

Table 1-2. Comparison of characteristics of commercialized or demonstrated different electrolysis systems [6,26,27].

	AWEC system	PEMEC system	SOEC system
Efficiency [a] (%)	63-70	56-60	up to 90
Electricity consumption ($kWh\ kg_{H2}^{-1}$)	50-78	50-83	35-55

Note: [a] Lower heating value of hydrogen produced divided by the electrical energy to the electrolysis cell.

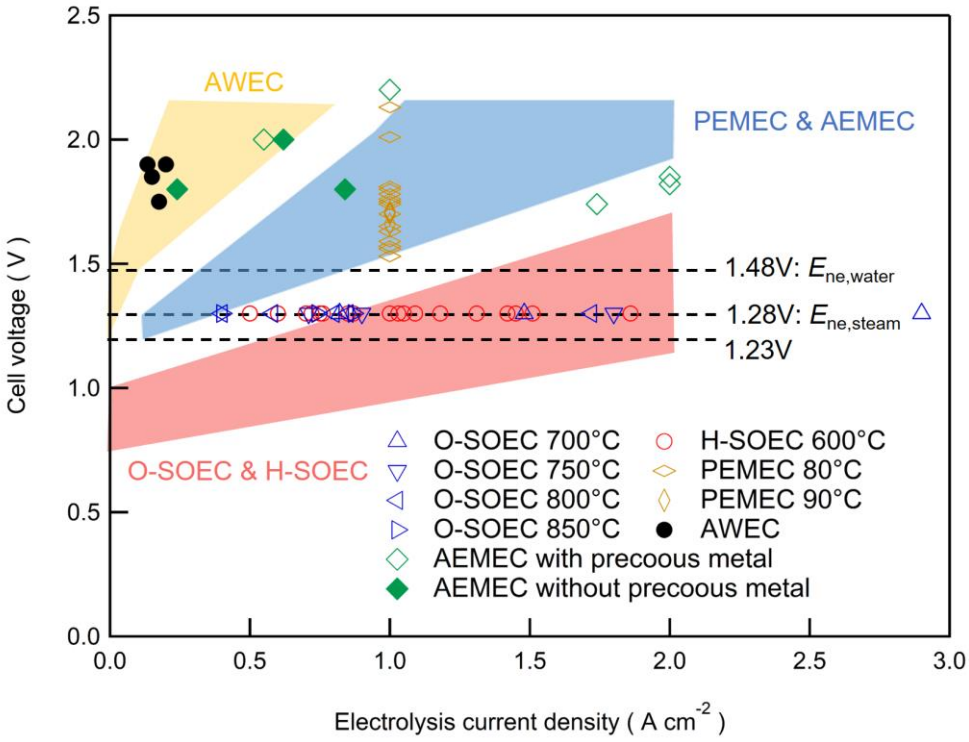

Figure 1-2. Typical ranges of polarization curves for different types of water (or steam) electrolysis cells based on [28]: each color represents AWEC (yellow), PEMEC & AEMEC (blue) and O-SOEC & H-SOEC. Plots represent relationships between cell voltages and electrolysis currents of O-SOEC [29-42], H-SEOC [43-58], PEMEC [59-74], AEMEC [13-16,75-78], AWEC [79].

1.4. Protonic Solid Oxide Steam Electrolysis Cell (H-SOEC)

There exist two types of SCECs: oxide-ionic solid oxide steam electrolysis cell (O-SOEC) and protonic solid oxide steam electrolysis cell (H-SOEC). Their features are summarized in Table 1-3. Conventional O-SOECs using O^{2-} ion-conducting yttria-stabilized zirconia (YSZ) as electrolyte material is commercially available and is normally operated at high temperatures above 800°C because of large activation energy (about 1 eV) for the O^{2-} ion conduction [80,81]. The operation at such high temperatures is thermodynamically advantageous, as described in chapter 1.3, but it decreases the cell life owing to the heat degradation of the constituent materials [82,83]. In addition, such an O-SOEC module needs to be constructed with high temperature steel of Cr or Ni alloys or ceramics and combine with the heat management/recycling systems, which limit the application field due to increased cost and volumes [84,85]. These issues exert strong demand to decrease the operation temperature of SOECs to below 600ºC. H^+-conducting $BaZr_xCe_{1-x-y}M_yO_{3-\delta}$ (BZCM; M=Y, Yb, etc.) perovskites have lower activation energy for ion conduction (about 0.5 eV) than that of YSZ [86], resulting in higher conductivity even in the temperature range [87,88]. Therefore, H-SOECs with proton-conducting perovskite oxides are an attractive alternative to O-SOECs because the relatively low operation temperatures (< 600ºC) are advantageous for various applications.

1.4.1. Advantages of H-SOEC

In a H-SOEC, the cathode and anode reactions are given by (1-5) and (1-6), respectively (Table 1-3). In the following, the electrode that produces hydrogen is called the fuel electrode or cathode, and the electrode that produces oxygen is called the air electrode or anode.

Fuel electrode (cathode): $2H^+$ (electrolyte) + $2e^- \rightarrow H_2$ (g) (1-5)

Air electrode (anode): $H_2O(g) \rightarrow 1/2\ O_2(g) + 2H^+$ (electrolyte) + $2e^-$ (1-6)

When steam is supplied to the anode, the protons generated by the water-splitting reaction migrate through the electrolyte and are reduced to hydrogen gases at the cathode. The hydrogen products are

diluted by steam in O-SOECs because steam gases are supplied to the cathode side, which results in the difficulty in producing high pressure, pure hydrogen gases. Since SOECs normally uses Ni cathode as a porous cermet [89-92], O-SOECs involves a risk of the degradation of the cathode due to oxidizing Ni metal by high temperature steam [82,83,92]. These problems related to the cathodes can be avoided in H-SOECs. H-SOECs produce directly high pressure, pure hydrogen at the cathode because hydrogen product according to Equation (1-5) is not diluted by steam and related impurities (CO_2) [93]. Therefore, downstream separation apparatus is not necessary, and thus the system can be simplified. Similarly, Ni oxidation is not severe in H-SOECs because of the relatively low temperature and water vapor pressure.

1.4.2. Mechanism of Proton Conduction in Perovskites

Y-doped $BaCeO_3$ (BCY) perovskite is well-known proton conductors with very high proton conductivity [88]. In this material, a part of the Ce^{4+} cations occupying the B sites are replaced by acceptor, i.e., Y^{3+} cations, and thus oxygen vacancy defects are generated by the defect reaction (1-7) for the charge neutrality condition. All the defects are represented using the Krögger–Vink notation.

$$Y_2O_3 \rightarrow 2Y_{Ce}' + 3O_O^{\times} + V_O^{\bullet\bullet} \quad (1\text{-}7)$$

Where $V_O^{\bullet\bullet}$ represents oxygen vacancies, and $O_O^{\times}$ represents lattice oxygen. The hydration reaction proceeds in BCY in a humidified atmosphere via association of water molecules and oxygen vacancy defects by Equation (1-8), resulting in formation of a proton defect ($OH_O^{\bullet}$).

$$H_2O + V_O^{\bullet\bullet} + O_O^{\times} \rightleftarrows 2\,OH_O^{\bullet} \quad (1\text{-}8)$$

The proton defects thus developed causes proton conductivity by hopping through repeated cleavage and formation of O–H bonds [94,95].

Table 1-3. Characteristics of O-SOEC and H-SOEC [80-88].

	Oxide-ionic Solid Oxide steam Electrolysis Cell (O-SOEC)	Protonic Solid Oxide steam Electrolysis Cell (H-SOEC)
	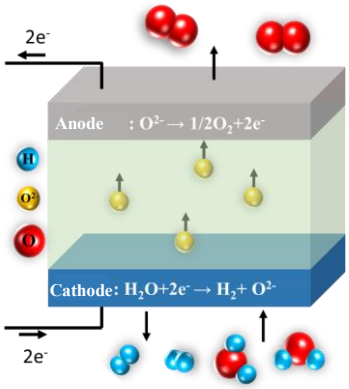	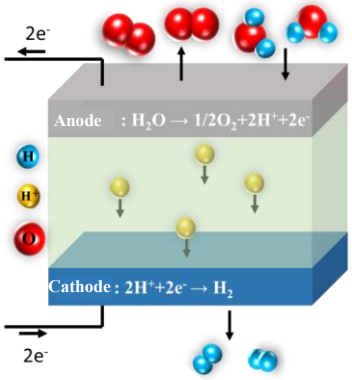
Charge carrier	O^{2-}	H^+
Electrolyte	Yttria-stabilized zirconia (YSZ)	$BaZr_xCe_{1-x-y}M_yO_{3-\delta}$ (BZCM; M = Y, Yb, etc.)
temperature	700-1000℃	400-600℃
Anodic reaction	$O^{2-} \rightarrow 1/2O_2 + 2e^-$	$H_2O \rightarrow 1/2O_2 + 2H^+ + 2e^-$
Anode materials	O^{2-}/e^- conductor; perovskite (La, Sr, Ba(Mn, Co, Fe)$O_{3-\delta}$	$H^+/O^{2-}/e^-$ triple conductor; layered perovskite Pr(Ba, Sr)(Co, Fe)$O_{5+\delta}$
Cathodic reaction	$H_2O + 2e^- \rightarrow H_2 + O^{2-}$	$2H^+ + 2e^- \rightarrow H_2$
Cathode materials	Ni-YSZ	Ni-BZCM cermet
Applicability	Demonstration	Laboratory scale
Advantage	High Faradaic efficiency, PGM-free electrocatalysts available, Tolerant for CO_2	Pure dry H_2, Cost effective due to lowering operating temperature, Prevents Ni oxidation in cathodes
Disadvantage	Expensive thermal-resistant components, Short lifetime, Dilution of hydrogen	Low Faradaic efficiency, Large anode overpotential, Cell processing

1.4.3. Thermodynamic properties of BZCM

$BaZr_{0.1}Ce_{0.7}Y_{0.2}O_{3-\delta}$ (BZCY172) has been applied to proton ceramic fuel cells (PCFC) as an electrolyte due to the high proton conductivity, and the corresponding cells have obtained a high peak power density of 587 mW cm^{-2} even at 500°C [96], which was the champion data for a decade. This material is also attractive for H-SOECs. However, the BZCM electrolytes tend to be thermodynamically unstable in a relatively high water vapor pressure (p_{H2O}) at temperatures below 800°C and Ce-rich side phase such as BZCY172 decompose into $Ba(OH)_2$ and CeO_2 phases, as shown in the following Equation (1-9) [97].

$$BaCeO_3 + H_2O \rightarrow Ba(OH)_2 + CeO_2 \quad (1\text{-}9)$$

$$BaZrO_3 + H_2O \rightarrow Ba(OH)_2 + ZrO_2 \quad (1\text{-}10)$$

On the other hand, Zr-rich side phase, such as $BaZr_{0.8}Y_{0.2}O_{3-\delta}$ (BZY82) shows a positive change of the Gibbs free energy in Equation (1-10) at temperatures above 100°C and thus very stable under high p_{H2O} [98]. Similar trends also appear in concern with the tolerance to CO_2: Ce-rich side phase decomposes into $BaCO_3$ and CeO_2 in presence of CO_2 while Zr-rich one does not [97,99]. Therefore, Zr-rich side BZCY phase is favorable for steam electrolysis applications in the intermediate temperature ranges [97,100]. H-SOECs with Zr-rich side BZCM have been, unfortunately, reported to exhibit lower performance than ones with Ce-rich side BZCM, because BZCM ceramics tend to show poor sinterability with increasing Zr contents due to the highly refractory nature of $BaZrO_3$ moieties [101] and their coarse-grained microstructures involve large grain-boundary resistances of electrolytes. Normally, Zr-rich side phase requires sintering temperatures over 1600°C for sufficient grain growth [102], but such high-temperature sintering causes BaO evaporation and undesired reaction at the interface between the electrolyte and cermet cathodes, which significantly increases electrolyte resistances of electrolysis cells. Hence, it is intensely demanding to fabricate highly efficient anode-supported cells with large-grained electrolyte films using higher Zr-content $BaZr_xCe_{1-x-y}M_yO_{3-\delta}$ ($1 - x - y \leq x$) under moderate sintering conditions.

1.5. Major issue of H-SOEC: Hole leak current

1.5.1 Lowered efficiency of H-SOECs

The performances of the current H-SOECs lags far behind O-SOECs even in the temperature ranges, where the proton conductivity of BZCM is much higher than oxide ion conductivity of YSZ [103,104]. The biggest issue of H-SOECs is low Faradaic efficiency due to the minor hole conduction in BZCM electrolyte. Table 1-4 shows a list of recent papers on H-SOECs regarding to Faradaic efficiencies. The efficiency of the thin-film electrolyte cells is below 70% in many cases, when the hydrogen partial pressure at the cathode is less than 5 MPa [105]. The efficiency of cells using bulk electrolytes (~several millimeters in thickness) is 80% at the highest [51, 54, 106-115]. This is a crucial issue for the H-SOEC application to a grid-scale hydrogen energy storage technology.

Table 1-4 Summary of H-SOEC Faradaic efficiencies reported in recent years.

Cell configuration (Thickness of electrolyte)	Voltage (V)	*T* (°C)	Anode atmosphere	Faradaic efficiency (%)	Ref.
4 wt% Fe_2O_3-LSM-BCZYZ /BCZYZ/ LSCM-BCZYZ (~15 μm)	1.6	800	5% H_2O, 95% air	65	[106]
LSCF-BCZYZ | BCZYZ | Ni-BCZYZ (20 μm)	2.0	800	3% H_2O, 97% Ar	50	[107]
BSCF-BCZYZ | BCZYZ | Ni-BCZYZ (20 μm)	2.0	800	3% H_2O, 97% Ar	64	[107]
PNC | BZCYYb4411 | Ni-BZCYYb (15 μm)	1.3	600	15% H_2O, 85% air	78	[54]
LSCF | LSC/ BZY82/BZCY172 | Pd (~2 μm)	1.22-1.28	500	50% H_2O, 50% Air	70-79	[108]
BLC | $BZCY(54)_{8/9}2$ | Ni-SZCY541 (17 μm)	1.78	550	80% H_2O, 0.2% O_2, 19.8% Ar	67	[109]
BLC | SZCY541 | Ni-SZCY541 (17 μm)	1.93	550	80% H_2O, 0.2% O_2, 19.8% Ar	65	[109]

BCFZY | BCZYYb7111| Ni-BCZYYb1711 (~10 μm)	(400 mA cm^{-2})	600	20% H_2O, 80% air	77.8	[51]
BCFZY | BCZYYb7111| Ni-BCZYYb1711 (~10 μm)	(400 mA cm^{-2})	600	85% H_2O, 15% air	98.6	[51]
SFM-BZY82 | BZY82 | Ni-BZY82 (16 μm)	1.3	600	3% H_2O, 97% air	63.6	[110]
LSCM-BZCYZ | BZCYZ | Ni-BCZYZ (75 μm)	2.0	700	5% H_2O, 95% N_2	22	[111]
BLC | SZCY541 | Ni-SZCY541 (20 μm)	1.74	600	80% H_2O, 0.2% O_2, 19.8% Ar	78	[112]
BGLC | SZCY541 | Ni-SZCY541 (20 μm)	1.93	600	80% H_2O, 0.2% O_2, 19.8% Ar	72	[112]
LSMS- BCZYZ | BCZYZ | LSCM- BCZYZ (2 mm)	2.0	700	5% H_2O, 95% Ar	80	[113]
SSC | BZCY442 | Pt (2 mm)	1.3	600	20% H_2O, 80% air	80	[114]
LSM-BCZYZ/BCZYZ/Ni-BCZYZ (2 mm)	1.4	800	10% H_2O, 90% air	46	[115]

Note: $La_{0.8}Sr_{0.2}MnO_{3-\delta}$ (LSM), $La_{0.75}Sr_{0.25}Cr_{0.5}Mn_{0.5}O_{3-\delta}$ (LSCM), $BaCe_{0.5}Zr_{0.3}Y_{0.16}Zn_{0.04}O_{3-\delta}$ (BCZYZ), $La_{0.8}Sr_{0.2}Mn_{0.95}Sc_{0.05}O_{3-\delta}$ (LSMS),$La_{0.6}Sr_{0.4}Co_{0.2}Fe_{0.8}\ O_{3-\delta}$ (LSCF), $Ba_{0.5}Sr_{0.5}Co_{0.8}Fe_{0.2}\ O_{3-\delta}$ (BSCF), $PrNi_{0.5}Co_{0.5}O_{3-\delta}$(PNC), $BaZr_{0.4}Ce_{0.4}Y_{0.1}Yb_{0.1}O_{3-\delta}$(BZCYYb4411), $La_{0.5}Sr_{0.5}CoO_{3-\delta}$(LSC), $BaZr_{0.1}Ce_{0.7}Y_{0.2}O_{3-\delta}$ (BZCY172), $BaZr_{0.8}Y_{0.2}O_{3-\delta}$ (BZY82), $Ba_{0.5}La_{0.5}CoO_{3-\delta}$ (BLC), $Ba(Zr_{0.5}Ce_{0.4})_{8/9}Y_{0.2}O_{3-\delta}$ (BZCY(54)$_{8/9}$2), $SrZr_{0.5}Ce_{0.4}Y_{0.1}O_{3-\delta}$ (SZCY541), $BaCo_{0.4}Fe_{0.4}Zr_{0.1}Y_{0.1}O_{3-\delta}$ (BCFZY), $BaCe_{0.7}Zr_{0.1}Y_{0.1}Yb_{0.1}O_{3-\delta}$(BCZYYb7111), $BaZr_{0.3}Ce_{0.5}Y_{0.16}Zn_{0.04}O_{3-\delta}$ (BZCYZ), $BaGd_{0.8}La_{0.2}Co_2O_{6-\delta}$ (BGLC), $La_{0.8}Sr_{0.2}Mn_{0.95}Sc_{0.05}O_{3-\delta}$ (LSMS), $Sm_{0.5}Sr_{0.5}Co_{0.5}O_{3-\delta}$ (SSC), $BaZr_{0.4}Ce_{0.4}Y_{0.2}O_{3-\delta}$ (BZCY442).

1.5.2 Formation of hole carries in BZCM

The relatively low Faradaic efficiency of H-SOECs is attributed to the conduction of the hole minor carries. BZCM involves the proton conductivity through the hydration reaction (1-8), as mentioned above, meanwhile it involves minor conduction of hole carriers (h•) which are generated through the oxidation reaction (1-11) via association of oxygen vacancies and oxygen gas, as shown in the defect reaction Equation (1-11).

$$V_O^{\bullet\bullet} + 1/2\ O_2 \rightleftarrows O_O^{\times} + 2h^{\bullet} \quad (1\text{-}11)$$

Equation (1-8) and (1-11) reveal that BZCM are mixed conductors with three types of charge carriers: proton, hole, and oxygen vacancy [116]. The O^{2-} ion conductivity of BZCM is normally about two orders of magnitude smaller than the proton conductivity under a humidified atmosphere, attributed to the small diffusivity of the former [117]. On the other hand, hole conductivity becomes predominant to proton conductivity at relatively high oxygen partial pressure (p_{O2}) in dry atmosphere [116]. Coupling of Equation (1-8) and (1-11) gives the hole carrier concentration at the electrolyte surface as follows.

$$[h^{\bullet}] = {K_{\mathrm{OX}}}^{\frac{1}{2}} {K_{\mathrm{hyd}}}^{-\frac{1}{2}} [\mathrm{OH_O^{\bullet}}][\mathrm{O_O^{\times}}]^{-1} {p_{\mathrm{H_2O}}}^{-\frac{1}{2}} {p_{\mathrm{O_2}}}^{\frac{1}{4}} = {K_{\mathrm{OX}}}^{\frac{1}{2}} {K_{\mathrm{hyd}}}^{-\frac{1}{2}} {K_{\mathrm{W}}}^{\frac{1}{2}} [\mathrm{OH_O^{\bullet}}][\mathrm{O_O^{\times}}]^{-1} {p_{\mathrm{H_2}}}^{-\frac{1}{2}} \quad (1\text{-}12)$$

Here, the electrolyte is assumed to be fully hydrated and K_{hyd} and K_{ox} are equilibrium constant of defect reaction (1-8) and (1-11), respectively. K_w is equilibrium constant of water dissociation reaction. The terms of $[\mathrm{OH_O^{\bullet}}][\mathrm{O_O^{\times}}]^{-1} {p_{\mathrm{H_2O}}}^{-\frac{1}{2}} {p_{\mathrm{O_2}}}^{\frac{1}{4}}$ are represented by Nernst potential of the anode reaction $\left(\frac{1}{2}\mathrm{O_2} + 2e^{-} + 2[\mathrm{OH_O^{\bullet}}] \rightarrow \mathrm{H_2O} + 2[\mathrm{O_O^{\times}}]\right)$ as follows.

$$E = E^0 - \frac{RT}{2F} \ln\left(\frac{p_{\mathrm{H_2O}}[\mathrm{O_O^{\times}}]^2}{{p_{\mathrm{O_2}}}^{\frac{1}{2}}[\mathrm{OH_O^{\bullet}}]^2}\right) = E^0 + \frac{RT}{F} \ln\left(\frac{{p_{\mathrm{O_2}}}^{\frac{1}{4}}[\mathrm{OH_O^{\bullet}}]}{{p_{\mathrm{H_2O}}}^{\frac{1}{2}}[\mathrm{O_O^{\times}}]}\right) \quad (1\text{-}13)$$

$$[\mathrm{OH_O^{\bullet}}][\mathrm{O_O^{\times}}]^{-1} {p_{\mathrm{H_2O}}}^{-\frac{1}{2}} {p_{\mathrm{O_2}}}^{\frac{1}{4}} = exp\left(\frac{F(E - E^0)}{RT}\right) \quad (1\text{-}14)$$

Here, E^0 is the standard potential for the anode reaction and E is the anode potential and thus (E– E^0) represents anode overpotential. Finally, (1-15) introduced to (1-12).

$$[h^{\bullet}] = {K_{\mathrm{OX}}}^{\frac{1}{2}} {K_{\mathrm{hyd}}}^{-\frac{1}{2}} exp\left(\frac{F(E - E^0)}{RT}\right) \quad (1\text{-}15)$$

The applied anode overpotential thus increases hole concentration in the electrolyte near the anode, which significantly reduces the Faradaic efficiency of H-SOECs [118-121]. In order to improve Faradaic efficiency, therefore, it is effective to reduce the anode overpotential by applying efficient anode materials.

Hole conduction can also be suppressed by lowering the operating temperature. The proton transport number of BZCM electrolytes increases with decreasing temperatures. Table 1-4 summarizes the temperature dependence of the proton transport number of $BaCe_{0.8}Y_{0.2}O_{3-\delta}$ (BCY82), $BaZr_{0.4}Ce_{0.4}Y_{0.2}O_{3-\delta}$ (BZCY442), and $BaCe_{0.8}Y_{0.2}O_{3-\delta}$ (BZY82) [122], which are investigated in wet hydrogen concentration cells. Table 1-4 shows that the proton transport number approaches one as temperature decreases to 500°C, which indicates that H-SOECs should be operated at lower temperatures to improve Faradaic efficiency. However, under fuel cell atmosphere (p_{O2} = 0.2 atm at anode side), the proton transport number decreases to 0.88 even at 600°C for $BaZr_{0.7}Ce_{0.2}Y_{0.1}O_{3-\delta}$ [123]. This imply lowering operating temperature does not completely prevent hole conduction.

Table 1-4. Proton transport number (t_H) of $BaCe_{0.8}Y_{0.2}O_{3-\delta}$ (BCY82), $BaZr_{0.4}Ce_{0.4}Y_{0.2}O_{3-\delta}$ (BZCY442), and $BaCe_{0.8}Y_{0.2}O_{3-\delta}$ (BZY82) measured in wet hydrogen [122].

T /°C	BCY82	BZCY442	BZY82
500	0.95	0.96	0.98
600	0.94	0.95	0.96
700	0.92	0.92	0.93
800	0.90	0.90	0.92

1.5.2. Low Faradaic efficiency of H-SOECs with Zr-rich side BZCM

According to the thermodynamic stability (chapter 1.4.3.), it is desirable to use high Zr-content BZCM electrolytes for long life H-SOECs system. Nevertheless, the studies of high Zr-content H-SOECs are quite few in comparisons to the high Ce-content one, and moreover, their performances are still limited. Figure 1-3 show the electrolysis current at around the thermal neutral point of H-SOECs with $BaZr_xCe_{1-x-y}M_yO_{3-\delta}$ ($2x \geq 1 - y$), which have been reported in a recent year [43, 51, 53, 54, 98, 105, 109, 110, 124-126]. Practically, H-SOECs are acquired to reach a hydrogen production rate of 1 $Nm^3\ h^{-1}$, which is corresponding to the electrolysis of about 1 A cm^{-2} at the thermal neutral point (1.3 V) by using the standard 1 kW class SOFC stacks (25-30 cell stacks; cell sizes 10 × 10 cm^2) [127, 128]. Unfortunately, the highest value at 500°C is 400 mA cm^{-2}, which is far below from the target value. Figure 1-4 shows the relationship between Faradaic efficiency and the electrolysis current of H-SOECs with Zr-rich side electrolytes [43, 54, 105-107, 109, 110, 112, 115]. The Faradaic efficiency tends to decrease with higher current density, and all cells do not exceed 80% at around 1 A cm^{-2}. In conclusion, it is urgent task to develop highly efficient H-SOECs with Zr rich side BZCM electrolyte for industrial green hydrogen production.

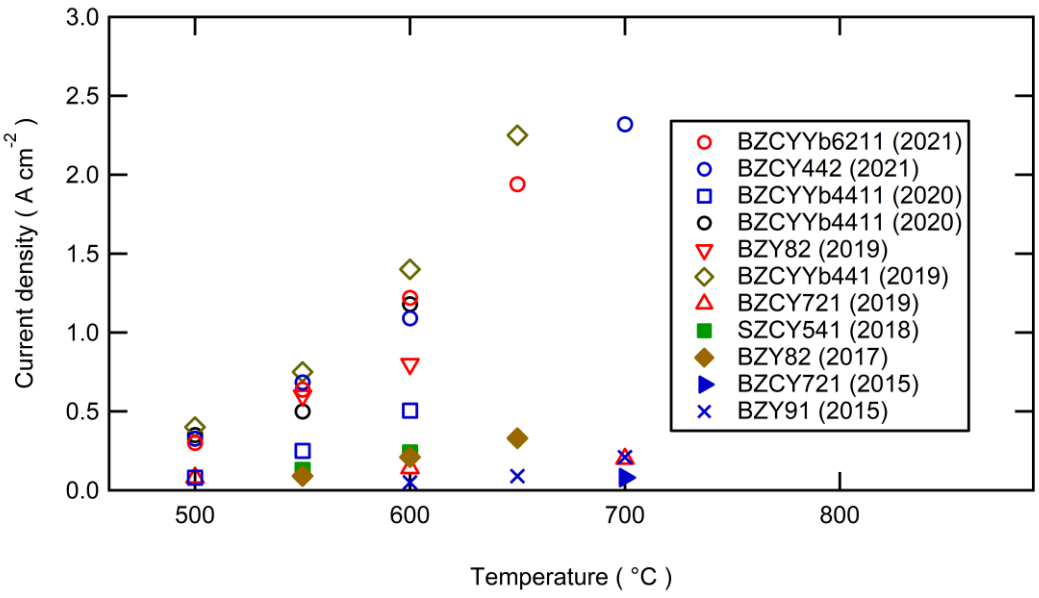

Figure 1-3. The relationship between the electrolysis current density and operating temperature at the thermal neutral point of H-SOECs with Zr-rich side electrolytes[43, 51, 53, 54, 98, 105, 109, 110, 124-126].

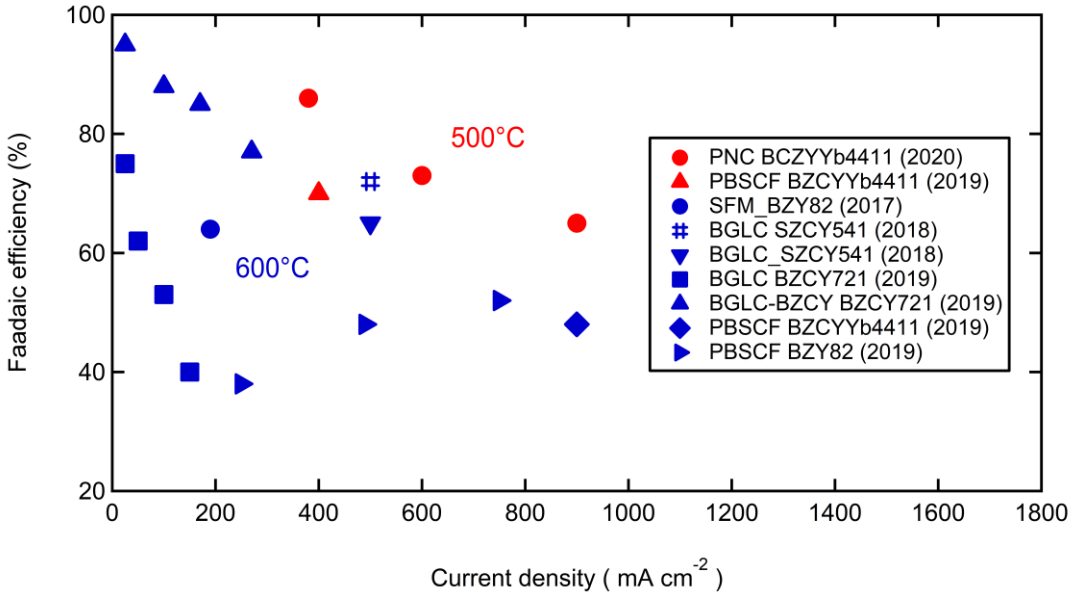

Figure 1-4. The relationship between Faradaic efficiency and the electrolysis current density of H-SOECs with Zr-rich electrolytes [43, 54, 105, 109, 110, 112].

1.6. Objectives of this thesis

The main objective of this study is to improve the Faradaic efficiency of H-SOECs comprising of Zr-rich side BZCM. For this, I attempted the following two approaches: 1) reduction of the anode overpotentials by developing a highly active anode electrodes with a $H^+/O^{2-}/e^-$ triple conductivity (or hydration capability), and 2) implementation of hydrogen permeable membrane cathode based on H^-/e^- mixed conductors which generates hydride ion (H^-) carriers through association of anion vacancies and molecular hydrogen by Equation (1-16). Prior to the studies on cathode and anode design for the increase of Faradaic efficiency, I investigated the performances of the porous cermet support type thin film cells with high Zr-content BZCM electrolytes because the studies on the fabrications of such cells are very rare and the knowledges for processing were still missing. Details of these approaches are described below.

1.6.1. Fabrication of H-SOEC with Zr-rich side BZCY electrolyte

Zr-rich side BZCM is a candidate for practical H-SOEC electrolytes because of its chemical stability to H_2O and CO_2, as mentioned in chapter 1.4.3. Meanwhile, there exists a few reports on H-SOECs with Zr-rich side electrolytes [43, 51, 53, 54, 98, 105, 109, 110, 124-126] because its poor sintering properties make it challenging to fabricate large-grain electrolyte thin films, and thus, the Faradaic efficiency of such cells still unclear. Recently, Jeong et al. reported the successful fabrication of thin film fuel cells of Zr-rich side $BaZr_{0.6}Ce_{0.2}Y_{0.2}O_{3-\delta}$ (BZCY622) with using a sinter aid of $Zn(NO_3)_2$ at relatively low sintering temperature (1400°C) [129]. In this thesis, a cathode-supported BZCY622 thin-film electrolyte cell was fabricated using a similar method, and its electrolysis performance was evaluated .

1.6.2. Reduction of the anode overpotentials by applying $H^+/O^{2-}/e^-$ triple conducting anode: development of high-valence-state manganate(V) $Ba_3Mn_2O_8$

According to Equation (1-15), it is important to reduce the considerable anode overpotential associated with the anode reaction, i.e., oxygen evolution reaction (OER) at the anode, in order to decrease hole concentration in the electrolyte. Well-established anode materials of solid oxide fuel cells (SOFCs), i.e., perovskite cobaltites and manganites have been also employed to H-SOECs, whereas these could not significantly reduce the anode overpotentials of H-SOECs in comparison with those of the cathodes of SOFCs [107, 130]. These transition metal perovskites are typical O^{2-}/e^- mixed conductors [30, 132, 133], so that the mismatch of major ion carriers between the anode and the electrolyte in H-SOECs confine the effective reaction area near gas–anode–electrolyte triple phase boundary (TPB), which results in relatively large polarization resistance in the anode (Figure 1-5a) [22, 133]. The anode polarization resistances of H-SOEC reported before starting this study are listed in Table 1-4. Hence, it is highly motivated to explore alternative anode candidates for highly efficient anode electrode of H-SOECs.

Recently, $H^+/e^-/O^{2-}$ triple conducting materials are attractive as an anode of H-SOECs since it extends the proton-accessible reaction areas from TPB to overall electrode surfaces [134-136] as shown in Figure 1-5b. Such materials were rather few, and the general guidelines to the corresponding materials design was still missing when I started this study. High-valence state transition metal oxides are known to show high reactivity towards OER and ORR in neutral or alkaline solutions owing to their unique electronic structures [137-140]. $Ba_3Mn_2O_8$ ($Ba_3(MnO_4)_2$) is a high-valence-state Mn(V) oxide that is known to be thermodynamically stable up to 1000°C in air, regardless of its unusual highly oxidized state [141]. In addition, $Ba_3(MnO_4)_2$ has a potential for proton conduction, because the crystal structure is similar to that of the scheelite-type proton conductor $LnTaO_4$ (Ln = La, Nd, Gd, Er) [142] with excellent hydration capability. Therefore, $Ba_3(MnO_4)_2$ is expected to reduce large anode polarization resistances by combining the electrocatalytic activity for the related charge transfer and extended reaction sites over the electrode surface due to the partial proton conductivity. Based on these, this thesis evaluates the performances and Faradaic efficiency of H-SOECs using $Ba_3(MnO_4)_2$ anodes.

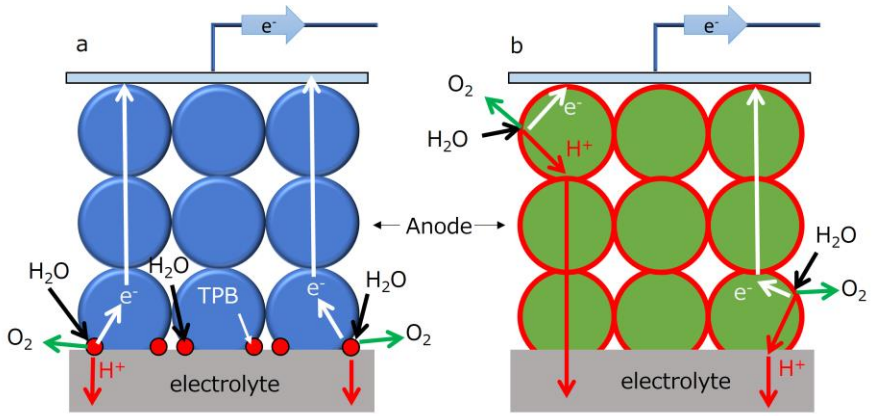

Figure 1-5. Working mechanism of different anode materials for H-SOECs. (a) mixed electron and oxygen-conducting electrodes. The active reaction sites are limited in vicinity of TPB. (b) Anode electrode with simultaneous proton and electron conduction. The active reaction sites extend over the whole electrode surface.

Tamle1-3. Polarization resistance of H-SOECs at 600°C under open circuit voltage (OCV).

Configuration of electrolysis cell: Anode/electrolyte (thickness)/cathode	Polarization resistance (Ω cm^2)	year	Ref.
SSC-BZCY352 | BZCY352 (20 μm) | Ni-BZCY352	2.41	2010	[130]
SFM-BZY82 | BZY82 (16 μm) | Ni-BZY82	0.65	2017	[110]
PBSCF | BZCYYb (20 μm) | Ni-BZCYYb	0.30	2017	[142]
SSC | BZCY442 (1.5 mm) | Pt	17.9	2018	[115]
SLF | BZCY352 (20 μm) | Ni-BZCY352	2.22	2018	[44]
LSN | BZCY172 (15 μm) | Ni-BZCY172	1.47	2018	[143]
PSN | BZCY172 (15 μm) | Ni-BZCY172	2.17	2018	[143]
PNO-BZCY262 | BZCY262 (20 μm) | Ni-BZCY262	0.40	2018	[47]
SEFC-BZCY352 | BZCY352 (15 μm) | Ni-BZCY352	0.89	2018	[24]

Note: $Sm_{0.5}Sr_{0.5}CoO_{3-\delta}$ (SSC), $BaZr_{0.3}Ce_{0.5}Y_{0.2}O_{3-\delta}$ (BZCY352), $Sr_2Fe_{1.5}Mo_{0.5}O_{6-\delta}$ (SFM), $BaZr_{0.8}Y_{0.2}O_{3-\delta}$ (BZY82), $PrBa_{0.5}Sr_{0.5}Co_{2-x}Fe_xO_{5+\delta}$ (PBSCF), $BaZr_{0.1}Ce_{0.7}Y_{0.2-x}Yb_xO_{3-\delta}$ (BZCYYb), $BaZr_{0.4}Ce_{0.4}Y_{0.2}O_{3-\delta}$ (BZCY442), $Sr_{2.8}La_{0.2}Fe_2O_{7-\delta}$ (SLF), $La_{1.2}Sr_{0.8}NiO_4$ (LSN), $BaZr_{0.1}Ce_{0.7}Y_{0.2}O_{3-\delta}$ (BZCY172), $Pr_{1.2}Sr_{0.8}NiO_4$ (PSN), $Pr_2NiO_{4+\delta}$ (PNO), $BaZr_{0.2}Ce_{0.6}Y_{0.2}O_{3-\delta}$ (BZCY262), $SrEu_2Fe_{1.8}Co_{0.2}O_{7-\delta}$ (SEFC).

1.6.3. Hole depression near the cathode/electrolyte interface: development of hydrogen permeable cathode based on H^-/e^- mixed conducting oxyhydrides

The hole carriers in BZCM could be decreased by decreasing p_{O2} in the electrolyte according to the Equation (1-12). Therefore, another possible approach for lowering hole leakage is to decrease the p_{O2} near the interface between BZCM/cathode. In a recent year, the power gains of protonic solid oxide fuel cells (H-SOFC) have been significantly improved by using a Pd foil as a hydrogen permeable solid anode [144, 145]. In this cell (so-called hydrogen-permeable metal-support fuel cell (HMFC)), oxide ions are accumulated near the interface between BZCM/Pd interface because Pd solid anode blocks the conduction of the secondary oxide ions which migrate from the cathode to the anode side under fuel cell conditions. Hence the BZCM electrolyte is forced to gain extra protons to compensate for the charge from the oxide ions accumulating via blocking, resulting in extremely low p_{O2} near the electrolyte/Pd interface [144, 145]. Based on this, p_{O2} near the electrolyte/Pd interface must be significantly decreased if HMFC is operated in the electrolysis mode. In the electrolysis mode of such

a cell, i.e., hydrogen-permeable metal-support electrolysis cell (HMEC) [108], oxygen vacancies accumulate near the Pd/electrolyte interface because the Pd cathode, a hydrogen-permeable alloy, prevents the migration of oxygen vacancies. As a result, the equilibrium of the oxidation reaction in Equation (1-11) tilts to the left, which results in decreasing the hole concentration and forming a depletion layer of holes near the cathode (Figure 1-6a). Hence this type of cells is speculated to suppress the hole leakage current.

Unfortunately, Pd is not favorable as a practical cathode because of the poor adhesion with oxide [108], together with the resource scarcity. Proton conducting BZCM-Ni composite membranes has been known to show hydrogen permeability in humidified atmosphere due to the ambipolar diffusion of protons and electrons [146-149]. When the steam electrolysis is conducted with the HMEC using Ni-BZCM solid cathode by feeding the humidified cathode gas, the association of water and oxygen vacancies must proceed at the cathode/electrolyte interface by the reaction (1-8), and thus the oxygen vacancies do not accumulate near the interface (Figure 1-6b). On the other hand, the electrolysis performances would be deteriorated if dry cathode gas is fed, because the proton carriers in the cathode is lowered due to the low p_{H2O} and thus Ni-BZCM composite cathode shows low hydrogen permeability (Figure 1-6c). Accordingly, it is strongly motivated to develop the cathode materials that can allow the reversible adsorption/desorption of hydrogen without relying on the hydration reaction (1-8).

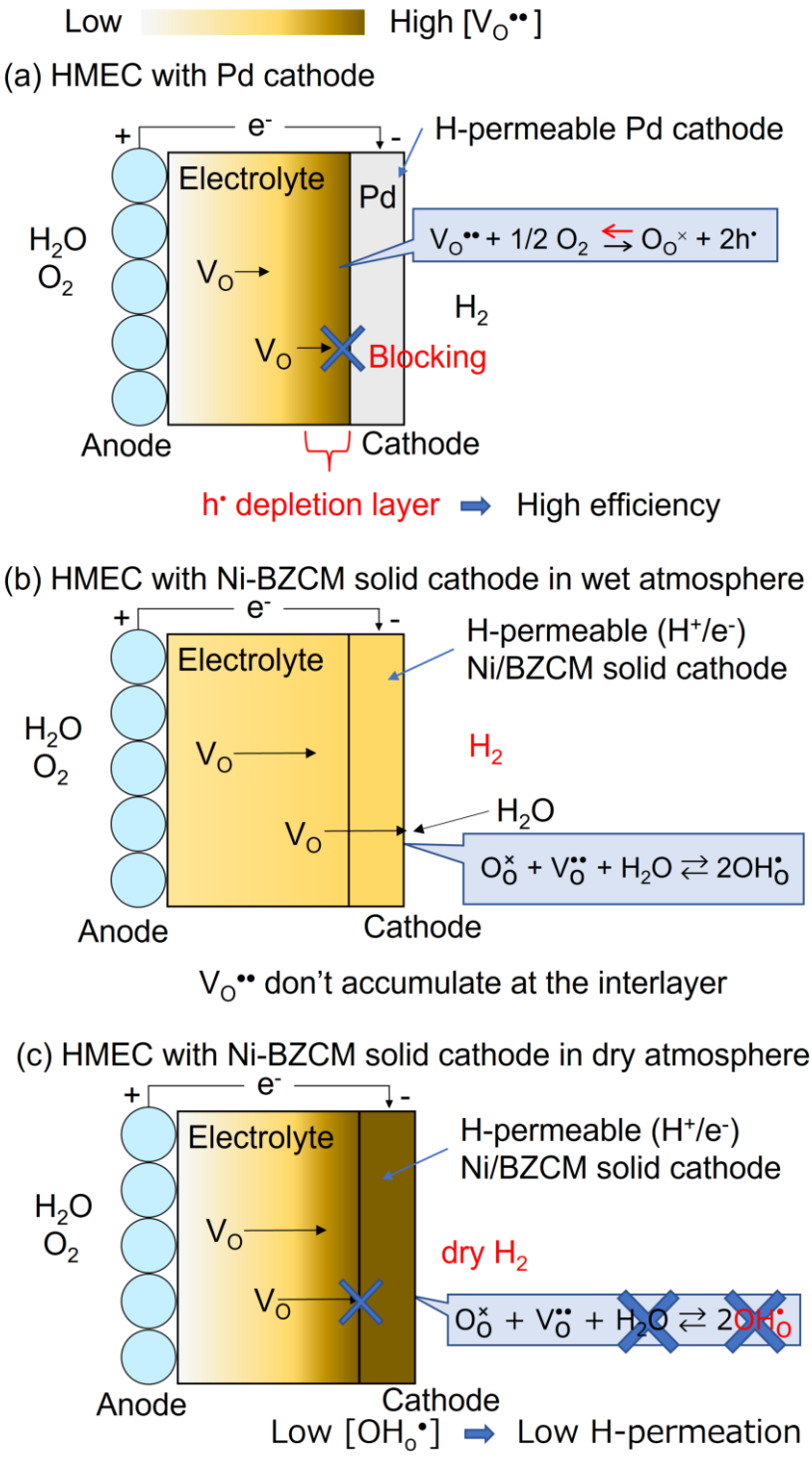

Figure 1-6. Schematic diagrams of HMEC with hydrogen-permeable (a) Pd cathode, and (b, c) Ni-BZCM solid cathode in (b) dry and (c) wet atmosphere.

Some pioneer works have predicted the possibility for the formation of H^- ion defects in perovskites, such as $SrTi_{1-x}Fe_xO_{3-x/2}$ at very low oxygen partial pressure [150-152]. In the oxides, H^- ion defects are speculated to form via association of anion vacancies and hydrogen molecules as follows.

$$H_2 + 2\,V_O^{\bullet\bullet} + 2e' \rightleftarrows 2\,H_O^{\bullet} \quad (1\text{-}16)$$

Where $H_O^{\bullet}$ represents H^- ion defects in the oxygen site and e' is electron. The feature of equation (1-16) reveals that the oxyhydrides with enhanced hydride ion (H^-) conductivity is a promising candidate of hydrogen-permeable cathode of H-SOECs because these intake H^- ion carriers without relying on hydration reaction. In recent years, several oxyhydrides have been synthesized, some of which have been found to show high H^- ion conductivity [153-160] (described in detail in chapter 4). However, their harsh preparation conditions and pyrolytic nature at elevated temperature are serious problems in applications to H-SOEC. In a recent year, cubic perovskite $BaTiO_{1-x}H_x$ ($x \leq 0.6$) have been synthesized by the chemical reaction between parent oxides ($BaTiO_3$) and hydrogen sources (CaH_2) via O^{2-}/H^- anion substitution [161]. The oxyhydrides were air stable and persistent without decomposition by boiling in a hot water [161]. Unfortunately, the bulk diffusivity of H^- ions was relatively low [162, 163]. Nevertheless, these findings implies that the perovskite oxyhydride systems are potential candidate of H^- ion conductors combing relatively high conductivity and durability [161-163]. In this thesis, I aimed to explore the hydrogen permeable materials based on H^- ion-conducting oxyhydrides.

1.7. Contents of this thesis

This thesis consists of 6 chapters as follows.

Chapter 1 gave an overview of the green hydrogen production and a summary for the recent achievements of protonic ceramics steam electrolysis technologies. The motivations and objectives in these studies were also described.

In chapter 2, porous cathode support type electrolysis cells based on high Zr-content $BaZr_{0.6}Ce_{0.2}Y_{0.2}O_{3-\delta}$ (BZCY622) electrolytes were fabricated via one step co-firing process with

$Zn(NO_3)_2$ additives at relatively low sintering temperature. The cells with $La_{0.6}Sr_{0.4}Co_{0.2}Fe_{0.8}O_{3-\delta}$ (LSCF) anode and $La_{0.5}Sr_{0.5}CoO_{3-\delta}$ (LSC) anode functional layer (AFL; 40 nm thickness) produced relatively high electrolysis current of 0.87 A cm^{-2} at a 1.3 V bias at 600°C, but the Faradaic efficiency was limited to 65% under 400 mA cm^{-2}. The Faradaic efficiency of the cell studied here was similar to previous reports for H-SOECs with Zr-rich side BZCM electrolytes, although the current density of the former was higher than that of the latter. These suggested the necessity the improvement of Faradaic efficiency of the H-SOECs.

In chapter 3, high-valence-state transition metal oxides $Ba_3(MnO_4)_2$ anode was demonstrated to be useful for H-SOECs. $Ba_3(MnO_4)_2$ was found to cause hydration at around 700°C in humidified air at water partial pressure of 2.3 kPa. $Ba_3(MnO_4)_2$ caused a conductivity jump by one order of magnitude at approximately 600°C owing to the antiferromagnetic/paramagnetic phase transition, accompanied by a shape change of the tetrahedral MnO_4^{3-} anions from C_{3v} to T_d symmetry. The $Ba_3(MnO_4)_2$ anode with a conductive filler of $Sn_{0.95}Sb_{0.05}O_{2-\delta}$ was applied to H-SOECs based on $BaZr_{0.4}Ce_{0.4}Y_{0.2}O_{3-\delta}$ bulk electrolytes. The corresponding cells exhibited higher electrolysis current than the cells with $Sm_{0.5}Sr_{0.5}CoO_{3-\delta}$ anode, which was a well-known SOEC anode material. Impedance analysis in terms of oxygen and water partial pressure revealed that the superior performance of the $Ba_3(MnO_4)_2$ base anode can be attributed to the extended reaction area. $Ba_3(MnO_4)_2$ was hound to have relatively large negative hydration enthalpy (−140 kJ mol^{-1}), thereby exhibiting the partial proton conductivity. This ability could make the oxygen evolution reaction occur directly over the electrode surface, and thus the reaction sites were not limited to the gas–anode–electrolyte triple phase boundary. Hence the anode reaction resistances were significantly decreased with the extended active reaction areas

In chapter 4, I discovered highly nonstoichiometric oxyhydride perovskite $BaZr_{0.5}In(II)_{0.5}O_{2.25}H_{0.5}$ with enhanced H^- ion electron mixed conductivity. $BaZr_{0.5}In(III)_{0.5}O_{2.75}$, as the parent phase, was hydrogenated via simple H_2 gas annealing at 800°C under ambient pressure. The lattice contraction by the hydrogenation is only -0.07%, so that $BaZr_{0.5}In(III)_{0.5}O_{2.75}$ sinters were converted to

$BaZr_{0.5}In(II)_{0.5}O_{2.25}H_{0.5}$ one without structural collapse. Th hydrogen pumping tests with $BaZr_{0.5}In(II)_{0.5}O_{2.25}H_{0.5}$ sintered disc confirms the H^- ion conduction. Membrane devices comprising dense $BaZr_{0.5}In_{0.5}O_{2.25}H_{0.5}$ films on porous Ni-cermet supports were fabricated by conventional sintering method. The resultant devices exhibited higher hydrogen permeability than protonic ceramic ones at 500°C, which is equivalent to H^- ion conductivity of 10^{-3} S cm^{-1}. The relatively high H^- ion conductivity and structural features indicated that $BaZr_{0.5}In(II)_{0.5}O_{2.25}H_{0.5}$ allowed H^- ion hopping along the nearest neighbor anion vacancy cites due to the high oxygen deficiency over the site percolation threshold (0.75). Given their superior H^- ion conductivity and ease of manufacturing, the synthesized materials have great potential for applications in mixed conducting electrodes and hydrogen permeable membrane supports of ceramic electrochemical cells.

In chapter 5, the performance of H-SOEC with Ni-$BaZr_{0.5}In_{0.5}O_{2.25}H_{0.5}$ cermet support cathode was evaluated for the operation in dry cathode condition. {NiO-$BaZr_{0.5}In_{0.5}O_{2.75}$ | $BaZr_{0.5}In_{0.5}O_{2.75}$/AFL | anode} precursor cells were pretreated by feeding dry hydrogen to the cathode side and thus, {Ni-$BaZr_{0.5}In_{0.5}O_{2.25}H_{0.5}$ | $BaZr_{0.5}In_{0.5}O_{2.75}$/AFL | anode} cells were obtained. The H-SOECs with $BaZr_{0.5}In_{0.5}O_{2.25}H_{0.5}$ cermet cathode exhibited pronounced performances, achieving electrolysis current of 0.84 A cm^{-2} in 1.3 V at 500°C with Faradaic efficiency equaling over 90%, which was much higher than the previously reported H-SOECs. It was demonstrated that the introduction of the ionic heterojunction of H^+–electrolyte/H^--cathode can increase Faradaic efficiency to over 90% in Zr-rich side electrolyte cells.

In chapter 6, the overall summary and conclusion of this thesis are presented.

1.8. References

1. IPCC, 2014: *Climate Change 2014: Synthesis Report. Contribution of Working Groups I, II and III to the Fifth Assessment Report of the Intergovernmental Panel on Climate Change* [Core Writing Team, R.K. Pachauri and L.A. Meyer (eds.)]. IPCC, Geneva, Switzerland, 151 pp.
2. IEA, "World Energy Outlook 2016". https://iea.blob.core.windows.net/assets/ 680c05c8-1d6e-42ae-b953-8e0420d46d5/WEO2016.pdf
3. IPCC, 2021: Summary for Policymakers. In: *Climate Change 2021: The Physical Science Basis. Contribution of Working Group I to the Sixth Assessment Report of the Intergovernmental Panel on Climate Change* [Masson-Delmotte, V., P. Zhai, A. Pirani, S. L. Connors, C. Péan, S. Berger, N. Caud, Y. Chen, L. Goldfarb, M. I. Gomis, M. Huang, K. Leitzell, E. Lonnoy, J.B.R. Matthews, T. K. Maycock, T. Waterfield, O. Yelekçi, R. Yu and B. Zhou (eds.)]. Cambridge University Press. In Press.
4. IPCC, 2018: *Global Warming of 1.5°C.An IPCC Special Report on the impacts of global warming of 1.5°C above pre-industrial levels and related global greenhouse gas emission pathways, in the context of strengthening the global response to the threat of climate change, sustainable development, and efforts to eradicate poverty* [Masson-Delmotte, V., P. Zhai, H.-O. Pörtner, D. Roberts, J. Skea, P.R. Shukla, A. Pirani, W. Moufouma-Okia, C. Péan, R. Pidcock, S. Connors, J.B.R. Matthews, Y. Chen, X. Zhou, M.I. Gomis, E. Lonnoy, T. Maycock, M. Tignor, and T. Waterfield (eds.)]. In Press.
5. Secretariat, U. N. F. C. C. C. Nationally determined contributions under the Paris Agreement-Synthesis Report. (2021).
6. IEA. The Future of Hydrogen, IEA, Paris https://www.iea.org/reports/the-future-of-hydrogen, (2019).
7. Rozyyev, V., Thirion, D., Ullah, R., Lee, J., Jung, M., Oh, H., *et al*. High-capacity methane storage in flexible alkane-linked porous aromatic network polymers. *Nature Energy*, *4*(7), 604-611 (2019).
8. IEA, Global Energy & CO2 Status Report 2019, IEA, Paris https://www.iea.org/reports/global-energy-co2-status-report-2019, (2019).
9. Trasatti, S. Water electrolysis: who first? *Journal of Electroanalytical Chemistry, 476*(1), 90-91 (1999).
10. Ursua, A., Gandia, L. M., & Sanchis, P. Hydrogen production from water electrolysis: current status and future trends. *Proceedings of the IEEE*, *100*(2), 410-426 (2011).
11. Barbir, F. PEM electrolysis for production of hydrogen from renewable energy sources. *Solar Energy*, *78*(5), 661-669 (2005).
12. Carmo, M., Fritz, D. L., Mergel, J., & Stolten, D. A comprehensive review on PEM water

electrolysis. *International Journal of Hydrogen Energy*, *38*(12), 4901-4934 (2013).

13. Chen, N., Paek, S. Y., Lee, J. Y., Park, J. H., Lee, S. Y., & Lee, Y. M. High-performance anion exchange membrane water electrolyzers with a current density of 7.68 A cm^{-2} and a durability of 1000 hours. *Energy & Environmental Science*, *14*(12), 6338-6348 (2021).
14. Li, D., Park, E. J., Zhu, W., Shi, Q., Zhou, Y., Tian, H., *et al*. Highly quaternized polystyrene ionomers for high performance anion exchange membrane water electrolysers. *Nature Energy*, *5*(5), 378-385 (2020).
15. Motealleh, B., Liu, Z., Masel, R. I., Sculley, J. P., Ni, Z. R., & Meroueh, L. Next-generation anion exchange membrane water electrolyzers operating for commercially relevant lifetimes. *International Journal of Hydrogen Energy*, *46*(5), 3379-3386 (2021).
16. Hu, X., Huang, Y., Liu, L., Ju, Q., Zhou, X., Qiao, X., *et al*. Piperidinium functionalized aryl ether-free polyaromatics as anion exchange membrane for water electrolysers: Performance and durability. *Journal of Membrane Science*, *621*, 118964 (2021).
17. Sapountzi, F. M., Gracia, J. M., Fredriksson, H. O., & Niemantsverdriet, J. H. Electrocatalysts for the generation of hydrogen, oxygen and synthesis gas. *Progress in Energy and Combustion Science*, *58*, 1-35 (2017).
18. Park, J. E., Kang, S. Y., Oh, S. H., Kim, J. K., Lim, M. S., Ahn, C. Y., *et al*. High-performance anion-exchange membrane water electrolysis. *Electrochimica Acta*, *295*, 99-106 (2019).
19. Ebbesen, S. D., Jensen, S. H., Hauch, A., & Mogensen, M. B. High temperature electrolysis in alkaline cells, solid proton conducting cells, and solid oxide cells. *Chemical Reviews*, *114*(21), 10697-10734 (2014).
20. Miller, H. A., Bouzek, K., Hnat, J., Loos, S., Bernäcker, C. I., Weißgärber, T., *et al*. Green hydrogen from anion exchange membrane water electrolysis: a review of recent developments in critical materials and operating conditions. *Sustainable Energy & Fuels*, *4*(5), 2114-2133 (2020).
21. Varcoe, J. R., Atanassov, P., Dekel, D. R., Herring, A. M., Hickner, M. A., Kohl, P. A., *et al*. Anion-exchange membranes in electrochemical energy systems. *Energy & Environmental Science*, *7*(10), 3135-3191 (2014).
22. Bi, L., Boulfrad, S., & Traversa, E. Steam electrolysis by solid oxide electrolysis cells (SOECs) with proton-conducting oxides. *Chemical Society Reviews*, *43*(24), 8255-8270 (2014).
23. Carmo, M., Fritz, D. L., Mergel, J., & Stolten, D. A comprehensive review on PEM water electrolysis. *International Journal of Hydrogen Energy*, *38*(12), 4901-4934 (2013).
24. Huan, D., Shi, N., Zhang, L., Tan, W., Xie, Y., Wang, W., *et al*. New, efficient, and reliable air electrode material for proton-conducting reversible solid oxide cells. *ACS Applied Materials &*

Interfaces, *10*(2), 1761-1770 (2018).

25. Chen, C. Y., Lai, W. H., Yan, W. M., Chen, C. C., & Hsu, S. W. Effects of nitrogen and carbon monoxide concentrations on performance of proton exchange membrane fuel cells with Pt–Ru anodic catalyst. *Journal of Power Sources*, *243*, 138-146 (2013).
26. David, M., Ocampo-Martínez, C., & Sánchez-Peña, R. Advances in alkaline water electrolyzers: A review. *Journal of Energy Storage*, *23*, 392-403 (2019).
27. Harman, J., Hjalmarsson, P., Mermelstein, J., Ryley, J., Sadler, H., & Selby, M. 1MW-Class Solid Oxide Electrolyser System Prototype for Low-Cost Green Hydrogen. *ECS Transactions*, *103*(1), 383 (2021).
28. Graves, C., Ebbesen, S. D., Mogensen, M., & Lackner, K. S. Sustainable hydrocarbon fuels by recycling CO_2 and H_2O with renewable or nuclear energy. *Renewable and Sustainable Energy Reviews*, *15*(1), 1-23 (2011).
29. Laurencin, J., Hubert, M., Sanchez, D. F., Pylypko, S., Morales, M., Morata, A., *et al*. Degradation mechanism of $La_{0.6}Sr_{0.4}Co_{0.2}Fe_{0.8}O_{3-\delta}/Gd_{0.1}Ce_{0.9}O_{2-\delta}$ composite electrode operated under solid oxide electrolysis and fuel cell conditions. *Electrochimica Acta*, *241*, 459-476 (2017).
30. Zhang, W., Yu, B., & Xu, J. Investigation of single SOEC with BSCF anode and SDC barrier layer. *International Journal of Hydrogen Energy*, *37*(1), 837-842 (2012).
31. Laguna-Bercero, M. A., Kinadjan, N., Sayers, R., El Shinawi, H., Greaves, C., & Skinner, S. J. Performance of $La_{2-x}Sr_xCo_{0.5}Ni_{0.5}O_{4\pm\delta}$ as an Oxygen Electrode for Solid Oxide Reversible Cells. *Fuel Cells*, *11*(1), 102-107 (2011).
32. Brisse, A., Schefold, J., & Zahid, M. High temperature water electrolysis in solid oxide cells. *International Journal of Hydrogen Energy*, *33*(20), 5375-5382 (2008).
33. Shimada, H., Yamaguchi, T., Kishimoto, H., Sumi, H., Yamaguchi, Y., Nomura, K., & Fujishiro, Y. Nanocomposite electrodes for high current density over 3 A cm^{-2} in solid oxide electrolysis cells. *Nature Communications*, *10*, 5432 (2019).
34. López-Robledo, M. J., Laguna-Bercero, M. A., Larrea, A., & Orera, V. M. Reversible operation of microtubular solid oxide cells using $La_{0.6}Sr_{0.4}Co_{0.2}Fe_{0.8}O_{3-\delta}$-$Ce_{0.9}Gd_{0.1}O_{2-\delta}$ oxygen electrodes. *Journal of Power Sources*, *378*, 184-189 (2018).
35. Lee, S. I., Kim, J., Son, J. W., Lee, J. H., Kim, B. K., Je, H. J., *et al*. High performance air electrode for solid oxide regenerative fuel cells fabricated by infiltration of nano-catalysts. *Journal of Power Sources*, *250*, 15-20 (2014).
36. Zhang, Y., Han, M., & Sun, Z. High performance and stability of nanocomposite oxygen electrode for solid oxide cells. *International Journal of Hydrogen Energy*, *45*(8), 5554-5564 (2020).

37. Chauveau, F., Mougin, J., Bassat, J. M., Mauvy, F., & Grenier, J. C. A new anode material for solid oxide electrolyser: The neodymium nickelate $Nd_2NiO_{4+\delta}$. *Journal of Power Sources*, *195*(3), 744-749 (2010).
38. Dong, D., Shao, X., Hu, X., Chen, K., Xie, K., Yu, L., *et al.* Improved gas diffusion within microchanneled cathode supports of SOECs for steam electrolysis. *International Journal of Hydrogen Energy*, *41*(44), 19829-19835 (2016).
39. Ai, N., He, S., Li, N., Zhang, Q., Rickard, W. D., Chen, K., & Zhang, T. uppressed Sr segregation and performance of directly assembled $La_{0.6}Sr_{0.4}Co_{0.2}Fe_{0.8}O_{3-\delta}$ oxygen electrode on Y_2O_3-ZrO_2 electrolyte of solid oxide electrolysis cells. *Journal of Power Sources*, *384*, 125-135 (2018).
40. Kim, D., Park, J. W., Chae, M. S., Jeong, I., Park, J. H., Kim, K. J., *et al.* An efficient and robust lanthanum strontium cobalt ferrite catalyst as a bifunctional oxygen electrode for reversible solid oxide cells. *Journal of Materials Chemistry A*, *9*(9), 5507-5521 (2021).
41. Zhang, S. L., Wang, H., Lu, M. Y., Zhang, A. P., Mogni, L. V., Liu, Q. *et al.* Cobalt-substituted $SrTi_{0.3}Fe_{0.7}O_{3-\delta}$: a stable high-performance oxygen electrode material for intermediate-temperature solid oxide electrochemical cells. *Energy & Environmental Science*, *11*(7), 1870-1879 (2018).
42. Park, B. K., Scipioni, R., Zhang, Q., Voorhees, P. W., & Barnett, S. A. Tuning electrochemical and transport processes to achieve extreme performance and efficiency in solid oxide cells. *Journal of Materials Chemistry A*, *8*(23), 11687-11694 (2020).
43. Choi, S., Davenport, T. C., & Haile, S. M. Protonic ceramic electrochemical cells for hydrogen production and electricity generation: exceptional reversibility, stability, and demonstrated faradaic efficiency. *Energy & Environmental Science*, *12*(1), 206-215 (2019).
44. Huan, D., Wang, W., Xie, Y., Shi, N., Wan, Y., Xia, C., *et al.* Investigation of real polarization resistance for electrode performance in proton-conducting electrolysis cells. *Journal of Materials Chemistry A*, *6*(38), 18508-18517 (2018).
45. Yoo, Y., & Lim, N. Performance and stability of proton conducting solid oxide fuel cells based on yttrium-doped barium cerate-zirconate thin-film electrolyte. *Journal of Power Sources*, *229*, 48-57 (2013).
46. Sun, C., Yang, S., Lu, Y., Wen, J., Ye, X., & Wen, Z. Tailoring a micro-nanostructured electrolyte-oxygen electrode interface for proton-conducting reversible solid oxide cells. *Journal of Power Sources*, *449*, 227498 (2020).
47. Li, W., Guan, B., Ma, L., Hu, S., Zhang, N., & Liu, X. High performing triple-conductive $Pr_2NiO_{4+\delta}$ anode for proton-conducting steam solid oxide electrolysis cell. *Journal of Materials*

Chemistry A, *6*(37), 18057-18066 (2018).

48. Kim, J., Jun, A., Gwon, O., Yoo, S., Liu, M., Shin, J., *et al.* Hybrid-solid oxide electrolysis cell: A new strategy for efficient hydrogen production. *Nano Energy*, *44*, 121-126 (2018).
49. Wu, W., Ding, H., Zhang, Y., Ding, Y., Katiyar, P., Majumdar, P. K., *et al.* 3D self-architectured steam electrode enabled efficient and durable hydrogen production in a proton-conducting solid oxide electrolysis cell at temperatures lower than 600 C. *Advanced Science*, *5*(11), 1800360 (2018).
50. Murphy, R., Zhou, Y., Zhang, L., Soule, L., Zhang, W., Chen, Y., & Liu, M. A New Family of Proton-Conducting Electrolytes for Reversible Solid Oxide Cells: $BaHf_x$ $Ce_{0.8-x}$ $Y_{0.1}Yb_{0.1}O_{3-\delta}$. *Advanced Functional Materials*, *30*(35), 2002265 (2020).
51. Duan, C., Kee, R., Zhu, H., Sullivan, N., Zhu, L., Bian, L., *et al.* Highly efficient reversible protonic ceramic electrochemical cells for power generation and fuel production. *Nature Energy*, *4*(3), 230-240 (2019).
52. Tang, W., Ding, H., Bian, W., Wu, W., Li, W., Liu, X., *et al.* Understanding of A-site deficiency in layered perovskites: promotion of dual reaction kinetics for water oxidation and oxygen reduction in protonic ceramic electrochemical cells. *Journal of Materials Chemistry A*, *8*(29), 14600-14608 (2020).
53. Wang, N., Toriumi, H., Sato, Y., Tang, C., Nakamura, T., Amezawa, K., *et al.* $La_{0.8}Sr_{0.2}Co_{1-x}Ni_xO_{3-\delta}$ as the Efficient Triple Conductor Air Electrode for Protonic Ceramic Cells. *ACS Applied Energy Materials*, *4*(1), 554-563 (2020).
54. Ding, H., Wu, W., Jiang, C., Ding, Y., Bian, W., Hu, B., *et al.* Self-sustainable protonic ceramic electrochemical cells using a triple conducting electrode for hydrogen and power production. *Nature Communications*, *11*, 1907 (2020).
55. Zhou, Y., Liu, E., Chen, Y., Liu, Y., Zhang, L., Zhang, W., *et al.* An active and robust air electrode for reversible protonic ceramic electrochemical cells. *ACS Energy Letters*, *6*(4), 1511-1520 (2021).
56. Shin, J. S., Park, H., Park, K., Saqib, M., Jo, M., Kim, J. H., *et al.* Activity of layered swedenborgite structured $Y_{0.8}Er_{0.2}BaCo_{3.2}Ga_{0.8}O_{7+\delta}$ for oxygen electrode reactions in at intermediate temperature reversible ceramic cells. *Journal of Materials Chemistry A*, *9*(1), 607-621 (2021).
57. Wang, W., Li, Y., Liu, Y., Tian, Y., Ma, B., Li, J., *et al*. Ruddlesden–Popper-Structured $(Pr_{0.9}La_{0.1})_2(Ni_{0.8}Cu_{0.2})O_{4+\delta}$: An Effective Oxygen Electrode Material for Proton-Conducting Solid Oxide Electrolysis Cells. *ACS Sustainable Chemistry & Engineering*, *9*(32), 10913-10919 (2021).
58. Bian, W., Wu, W., Wang, B., Tang, W., Zhou, M., Jin, C., *et al*. Revitalizing interface in protonic ceramic cells by acid etch. *Nature*, *604*(7906), 479-485 (2022).
59. Millet, P., Pineri, M., & Durand, R. New solid polymer electrolyte composites for water

electrolysis. *Journal of Applied Electrochemistry*, *19*(2), 162-166 (1989).

60. Millet, P., Alleau, T., & Durand, R. Characterization of membrane-electrode assemblies for solid polymer electrolyte water electrolysis. *Journal of applied electrochemistry*, *23*(4), 322-331 (1993).
61. Millet, P., Andolfatto, F., & Durand, R. Design and performance of a solid polymer electrolyte water electrolyzer. *International Journal of Hydrogen Energy*, *21*(2), 87-93 (1996).
62. Yamaguchi, M., Yagiuchi, K., & Okisawa, K. R&D of high performance solid polymer electrolyte water electrolyzer in WE-NET. *Hydrogen Energy Progress XI*, *1*(3), 781 (1996).
63. Yamaguchi, M., Okisawa, K., & Nakanori, T. Development of high performance solid polymer electrolyte water electrolyzer in WE-NET. In *IECEC-97 Proceedings of the Thirty-Second Intersociety Energy Conversion Engineering Conference (Cat. No. 97CH6203)*, 3, 1958-1965, IEEE (1997).
64. Kondoh, M., Yokoyama, N., Inazumi, C., Maezawa, S., Fujiwara, N., Nishimura, Y., *et al*. Development of solid polymer-electrolyte water electrolyser. *Journal of New Materials for Electrochemical Systems*, *3* (2000).
65. Mandal, M., Valls, A., Gangnus, N., & Secanell, M. Analysis of inkjet printed catalyst coated membranes for polymer electrolyte electrolyzers. *Journal of The Electrochemical Society*, *165*(7), F543 (2018).
66. Shao, Z., Yi, B., & Han, M. The membrane electrodes assembly for SPE water electrolysis. In *Mao ZQ, Veziroglu TN, Ed. Proc. 13th World Hydrog. Energy Conf. Hydrog. energy Prog. XIII, 1-2* (2000).
67. Ioroi, T., Yasuda, K., Siroma, Z., Fujiwara, N., & Miyazaki, Y. Thin film electrocatalyst layer for unitized regenerative polymer electrolyte fuel cells. *Journal of Power sources*, *112*(2), 583-587 (2002).
68. Han, S. D., Singh, K. C., Rana, R. K., & Park, K. B. Hydrogen production by water electrolysis using solid polymer electrolyte. *NISCAIR-CSIR*, *41*(5), 955-959 (2002).
69. Rasten, E., Hagen, G., & Tunold, R. Electrocatalysis in water electrolysis with solid polymer electrolyte. *Electrochimica acta*, *48*(25-26), 3945-3952 (2003).
70. Marshall, A., Børresen, B., Hagen, G., Tsypkin, M., & Tunold, R. Electrochemical characterisation of $Ir_xSn_{1-x}O_2$ powders as oxygen evolution electrocatalysts. *Electrochimica Acta*, *51*(15), 3161-3167 (2006).
71. Marshall, A., Børresen, B., Hagen, G., Tsypkin, M., & Tunold, R. Hydrogen production by advanced proton exchange membrane (PEM) water electrolysers—Reduced energy consumption by improved electrocatalysis. *Energy*, *32*(4), 431-436 (2007).

72. Song, S., Zhang, H., Ma, X., Shao, Z., Baker, R. T., & Yi, B. Electrochemical investigation of electrocatalysts for the oxygen evolution reaction in PEM water electrolyzers. *International Journal of Hydrogen Energy*, *33*(19), 4955-4961 (2008).
73. Antonucci, V., Di Blasi, A., Baglio, V., Ornelas, R., Matteucci, F., Ledesma-Garcia, J., *et al*. High temperature operation of a composite membrane-based solid polymer electrolyte water electrolyser. *Electrochimica Acta*, *53*(24), 7350-7356 (2008).
74. Cheng, J., Zhang, H., Chen, G., & Zhang, Y. Study of $Ir_xRu_{1-x}O_2$ oxides as anodic electrocatalysts for solid polymer electrolyte water electrolysis. *Electrochimica Acta*, *54*(26), 6250-6256 (2009).
75. Kraglund, M. R., Carmo, M., Schiller, G., Ansar, S. A., Aili, D., Christensen, E., & Jensen, J. O. Ion-solvating membranes as a new approach towards high rate alkaline electrolyzers. *Energy & Environmental Science*, *12*(11), 3313-3318 (2019).
76. Xiao, J., Oliveira, A. M., Wang, L., Zhao, Y., Wang, T., Wang, J., *et al*. Water-fed hydroxide exchange membrane electrolyzer enabled by a fluoride-incorporated nickel–iron oxyhydroxide oxygen evolution electrode. *ACS Catalysis*, *11*(1), 264-270 (2020).
77. Fortin, P., Khoza, T., Cao, X., Martinsen, S. Y., Barnett, A. O., & Holdcroft, S. High-performance alkaline water electrolysis using Aemion™ anion exchange membranes. *Journal of Power Sources*, *451*, 227814 (2020).
78. Park, H. J., Lee, S. Y., Lee, T. K., Kim, H. J., & Lee, Y. M. N3-butyl imidazolium-based anion exchange membranes blended with poly (vinyl alcohol) for alkaline water electrolysis. *Journal of Membrane Science*, *611*, 118355 (2020).
79. Zeng, K., & Zhang, D. Recent progress in alkaline water electrolysis for hydrogen production and applications. *Progress in energy and combustion science*, *36*(3), 307-326 (2010).
80. Korte, C., Peters, A., Janek, J., Hesse, D., & Zakharov, N. Ionic Conductivity and Activation Energy for Oxygen Ion Transport in Superlattices-The Semicoherent Multilayer System YSZ (ZrO_2 + 9.5 mol% Y_2O_3)/Y_2O_3. *Physical Chemistry Chemical Physics*, *10*(31), 4623-4635 (2008).
81. Gerstl, M., Friedbacher, G., Kubel, F., Hutter, H., & Fleig, J. The relevance of interfaces for oxide ion transport in yttria stabilized zirconia (YSZ) thin films. *Physical Chemistry Chemical Physics*, *15*(4), 1097-1107 (2013).
82. Yang, X., & Irvine, J. T. $(La_{0.75}Sr_{0.25})_{0.95}Mn_{0.5}Cr_{0.5}O_3$ as the cathode of solid oxide electrolysis cells for high temperature hydrogen production from steam. *Journal of Materials Chemistry*, *18*(20), 2349-2354 (2008).
83. Matsui, T., Kishida, R., Kim, J. Y., Muroyama, H., & Eguchi, K. Performance deterioration of Ni–YSZ anode induced by electrochemically generated steam in solid oxide fuel cells. *Journal of The*

Electrochemical Society, *157*(5), B776 (2010).

84. Ni, M., Leung, M. K., & Leung, D. Y. Technological development of hydrogen production by solid oxide electrolyzer cell (SOEC). *International Journal of Hydrogen Energy*, *33*(9), 2337-2354 (2008).
85. Brett, D. J., Atkinson, A., Brandon, N. P., & Skinner, S. J. Intermediate temperature solid oxide fuel cells. *Chemical Society Reviews*, *37*(8), 1568-1578 (2008).
86. Kreuer, K. D. Proton-conducting oxides. *Annual Review of Materials Research*, *33*(1), 333-359 (2003).
87. Yang, L., Wang, S., Blinn, K., Liu, M., Liu, Z., Cheng, Z., & Liu, M. Enhanced Sulfur and Coking Tolerance of a Mixed Ion Conductor for SOFCs: $BaZr_{0.1}Ce_{0.7}Y_{0.2-x}Yb_xO_{3-\delta}$. *Science*, *326*(5949), 126-129 (2009).
88. Zuo, C., Zha, S., Liu, M., Hatano, M., & Uchiyama, M. $Ba(Zr_{0.1}Ce_{0.7}Y_{0.2})O_{3-\delta}$ as an Electrolyte for Low-Temperature Solid-Oxide Fuel Cells. *Advanced Materials*, *18*(24), 3318-3320 (2006).
89. Chen, K., & Ai, N. Reasons for the high stability of nano-structured $(La,Sr)MnO_3$ infiltrated Y_2O_3–ZrO_2 composite oxygen electrodes of solid oxide electrolysis cells. *Electrochemistry communications*, *19*, 119-122 (2012).
90. Electrocatalysts, N. High-Performance Electrode for Steam Electrolysis. *Electrochemical and Solid-State Letters*, *7*(12), A500-A502 (2004).
91. Patro, P. K., Delahaye, T., Bouyer, E., & Sinha, P. K. Microstructural development of Ni-1Ce10ScSZ cermet electrode for Solid Oxide Electrolysis Cell (SOEC) application. *international Journal of Hydrogen Energy*, *37*(4), 3865-3873 (2012).
92. Eguchi, K., Hatagishi, T., & Arai, H. Power generation and steam electrolysis characteristics of an electrochemical cell with a zirconia-or ceria-based electrolyte. *Solid State Ionics*, *86*, 1245-1249 (1996).
93. Ni, M., Leung, M. K., & Leung, D. Y. Electrochemical modeling of hydrogen production by proton-conducting solid oxide steam electrolyzer. *International Journal of Hydrogen Energy*, *33*(15), 4040-4047 (2008).
94. Guo, Y., Lin, Y., Ran, R., & Shao, Z. Zirconium doping effect on the performance of proton-conducting $BaZr_yCe_{0.8-y}Y_{0.2}O_{3-\delta}$ $(0.0 \le y \le 0.8)$ for fuel cell applications. *Journal of Power Sources*, *193*(2), 400-407 (2009).
95. Matsushita, E. Tunneling mechanism on proton conduction in perovskite oxides. *Solid State Ionics*, *145*(1-4), 445-450 (2001).
96. Nien, S. H., Hsu, C. S., Chang, C. L., & Hwang, B. H. Preparation of $BaZr_{0.1}Ce_{0.7}Y_{0.2}O_{3-\delta}$ Based

Solid Oxide Fuel Cells with Anode Functional Layers by Tape Casting. *Fuel Cells*, *11*(2), 178-183 (2011).

97. Sawant, P., Varma, S., Wani, B. N., & Bharadwaj, S. R. Synthesis, Synthesis, stability and conductivity of $BaCe_{0.8-x}Zr_xY_{0.2}O_{3-\delta}$ as electrolyte for proton conducting SOFC. *International Journal of Hydrogen Energy*, *37*(4), 3848-3856 (2012).
98. Bi, L., Shafi, S. P., & Traversa, E. Y-doped $BaZrO_3$ as a chemically stable electrolyte for proton-conducting solid oxide electrolysis cells (SOECs). *Journal of Materials Chemistry A*, *3*(11), 5815-5819 (2015).
99. Fabbri, E., D'Epifanio, A., Di Bartolomeo, E., Licoccia, S., & Traversa, E. Tailoring the chemical stability of $Ba(Ce_{0.8-x}Zr_x)Y_{0.2}O_{3-\delta}$ protonic conductors for Intermediate Temperature Solid Oxide Fuel Cells (IT-SOFCs). *Solid State Ionics*, *179*(15-16), 558-564 (2008).
100. Guo, Y., Ran, R., & Shao, Z. Optimizing the modification method of zinc-enhanced sintering of $BaZr_{0.4}Ce_{0.4}Y_{0.2}O_{3-\delta}$-based electrolytes for application in an anode-supported protonic solid oxide fuel cell. *International Journal of Hydrogen Energy*, *35*(11), 5611-5620 (2010).
101. Lindman, A., Helgee, E. E., & Wahnstrom, G. Comparison of space-charge formation at grain boundaries in proton-conducting $BaZrO_3$ and $BaCeO_3$. *Chemistry of Materials*, *29*(18), 7931-7941 (2017).
102. Duval, S. B. C., Holtappels, P., Vogt, U. F., Stimming, U., & Graule, T. Characterisation of $BaZr_{0.9}Y_{0.1}O_{3-\delta}$ Prepared by Three Different Synthesis Methods: Study of the Sinterability and the Conductivity. *Fuel Cells*, *9*(5), 613-621 (2009).
103. Lei, L., Zhang, J., Yuan, Z., Liu, J., Ni, M., & Chen, F. Progress report on proton conducting solid oxide electrolysis cells. *Advanced Functional Materials*, *29*(37), 1903805 (2019).
104. Strandbakke, R., Cherepanov, V. A., Zuev, A. Y., Tsvetkov, D. S., Argirusis, C., Sourkouni, G., *et al*. Gd-and Pr-based double perovskite cobaltites as oxygen electrodes for proton ceramic fuel cells and electrolyser cells. *Solid State Ionics*, *278*, 120-132 (2015).
105. Vøllestad, E., Strandbakke, R., Tarach, M., Catalán-Martínez, D., Fontaine, M. L., Beeaff, D., *et al*. Mixed proton and electron conducting double perovskite anodes for stable and efficient tubular proton ceramic electrolysers. *Nature Materials*, *18*(7), 752-759 (2019).
106. Li, H., Chen, X., Chen, S., Wu, Y., & Xie, K. Composite manganate oxygen electrode enhanced with iron oxide nanocatalyst for high temperature steam electrolysis in a proton-conducting solid oxide electrolyzer. *International Journal of Hydrogen Energy*, *40*(25), 7920-7931 (2015).
107. Li, S., & Xie, K. Composite oxygen electrode based on LSCF and BSCF for steam electrolysis in a proton-conducting solid oxide electrolyzer. *Journal of The Electrochemical Society*, *160*(2),

F224 (2013).

108. Aoki, Y., Nishimura, S., Jeong, S., Kitano, S., & Habazaki, H. Development of hydrogen-permeable metal support electrolysis cells. *ACS Applied Energy Materials*, *5*(2), 1385-1389 (2022).

109. Leonard, K., Okuyama, Y., Takamura, Y., Lee, Y. S., Miyazaki, K., Ivanova, M. E., *et al*. Efficient intermediate-temperature steam electrolysis with $Y:SrZrO_3$–$SrCeO_3$ and $Y:BaZrO_3$–$BaCeO_3$ proton conducting perovskites. *Journal of Materials Chemistry A*, *6*(39), 19113-19124 (2018).

110. Lei, L., Tao, Z., Wang, X., Lemmon, J. P., & Chen, F. Intermediate-temperature solid oxide electrolysis cells with thin proton-conducting electrolyte and a robust air electrode. *Journal of Materials Chemistry A*, *5*(44), 22945-22951 (2017).

111. Gan, Y., Zhang, J., Li, Y., Li, S., Xie, K., & Irvine, J. T. Composite oxygen electrode based on LSCM for steam electrolysis in a proton conducting solid oxide electrolyzer. *Journal of The Electrochemical Society*, *159*(11), F763 (2012).

112. Leonard, K., Druce, J., Thoreton, V., Kilner, J. A., & Matsumoto, H. Exploring mixed proton/electron conducting air electrode materials in protonic electrolysis cell. *Solid State Ionics*, *319*, 218-222 (2018).

113. Gan, L., Ye, L., Liu, M., Tao, S., & Xie, K. A scandium-doped manganate anode for a proton-conducting solid oxide steam electrolyzer. *RSC Advances*, *6*(1), 641-647 (2016).

114. Kobayashi, T., Kuroda, K., Jeong, S., Kwon, H., Zhu, C., Habazaki, H., & Aoki, Y. Analysis of the anode reaction of solid oxide electrolyzer cells with $BaZr_{0.4}Ce_{0.4}Y_{0.2}O_{3-\delta}$ electrolytes and $Sm_{0.5}Sr_{0.5}CoO_{3-\delta}$ anodes. *Journal of The Electrochemical Society*, *165*(5), F342 (2018).

115. Li, S., Yan, R., Wu, G., Xie, K., & Cheng, J. Composite oxygen electrode LSM-BCZYZ impregnated with Co3O4 nanoparticles for steam electrolysis in a proton-conducting solid oxide electrolyzer. *International Journal of Hydrogen Energy*, *38*(35), 14943-14951 (2013).

116. Heras-Juaristi, G., Pérez-Coll, D., & Mather, G. C. Temperature dependence of partial conductivities of the $BaZr_{0.7}Ce_{0.2}Y_{0.1}O_{3-\delta}$ proton conductor. *Journal of Power Sources*, *364*, 52-60 (2017).

117. Han, D., Noda, Y., Onishi, T., Hatada, N., Majima, M., & Uda, T. Transport properties of acceptor-doped barium zirconate by electromotive force measurements. *International Journal of Hydrogen Energy*, *41*(33), 14897-14908 (2016).

118. Azimova, M. A., & McIntosh, S. On the reversibility of anode supported proton conducting solid oxide cells. *Solid State Ionics*, *203*(1), 57-61 (2011).

119. Matsumoto, H., Okubo, M., Hamajima, S., Katahira, K., & Iwahara, H. Extraction and production of hydrogen using high-temperature proton conductor. *Solid State Ionics*, *152*, 715-720 (2002).
120. Sakai, T., Matsushita, S., Matsumoto, H., Okada, S., Hashimoto, S., & Ishihara, T. Intermediate temperature steam electrolysis using strontium zirconate-based protonic conductors. *International Journal of Hydrogen Energy*, *34*(1), 56-63 (2009).
121. Pérez-Coll, D., Heras-Juaristi, G., Fagg, D. P., & Mather, G. C. Transport-number determination of a protonic ceramic electrolyte membrane via electrode-polarisation correction with the Gorelov method. *Journal of Power Sources*, *245*, 445-455 (2014).
122. Zhao, L., Tan, W., & Zhong, Q. The chemical stability and conductivity improvement of protonic conductor $BaCe_{0.8-x}Zr_xY_{0.2}O_{3-\delta}$. *Ionics*, *19*(12), 1745-1750 (2013).
123. Robinson, S., Manerbino, A., Grover Coors, W., & Sullivan, N. P. Fabrication and Performance of Tubular, Electrode-Supported $BaCe_{0.2}Zr_{0.7}Y_{0.1}O_{3-\delta}$ Fuel Cells. *Fuel Cells*, *13*(4), 584-591 (2013).
124. Babiniec, S. M., Ricote, S., & Sullivan, N. P. Characterization of ionic transport through $BaCe_{0.2}Zr_{0.7}Y_{0.1}O_{3-\delta}$ membranes in galvanic and electrolytic operation. *International Journal of Hydrogen Energy*, *40*(30), 9278-9286 (2015).
125. Zhu, L. L., Huang, Y. E., Gong, L. K., Huang, X. Y., Qi, X. H., Wu, X. H., & Du, K. Z. Ligand Control of Room-Temperature Phosphorescence Violating Kasha's Rule in Hybrid Organic–Inorganic Metal Halides. *Chemistry of Materials*, *32*(4), 1454-1460 (2020).
126. Tang, C., Akimoto, K., Wang, N., Fadillah, L., Kitano, S., Habazaki, H., & Aoki, Y. The effect of an anode functional layer on the steam electrolysis performances of protonic solid oxide cells. *Journal of Materials Chemistry A*, *9*(24), 14032-14042 (2021).
127. Kishimoto, M., Muroyama, H., Suzuki, S., Saito, M., Koide, T., Takahashi, Y., *et al*. Development of 1 kW-class Ammonia-fueled Solid Oxide Fuel Cell Stack. *Fuel Cells*, *20*(1), 80-88 (2020).
128. Aicart, J., Di Iorio, S., Petitjean, M., Giroud, P., Palcoux, G., & Mougin, J. Transition cycles during operation of a reversible solid oxide electrolyzer/fuel cell (rSOC) system. *Fuel Cells*, *19*(4), 381-388 (2019).
129. Jeong, S., Kobayashi, T., Kuroda, K., Kwon, H., Zhu, C., Habazaki, H., & Aoki, Y. Evaluation of thin film fuel cells with Zr-rich $BaZr_xCe_{0.8-x}Y_{0.2}O_{3-\delta}$ electrolytes ($x \geq 0.4$) fabricated by a single-step reactive sintering method. *RSC Advances*, *8*(46), 26309-26317 (2018).
130. He, F., Song, D., Peng, R., Meng, G., & Yang, S. Electrode performance and analysis of reversible solid oxide fuel cells with proton conducting electrolyte of $BaCe_{0.5}Zr_{0.3}Y_{0.2}O_{3-\delta}$. *Journal of Power Sources*, *195*(11), 3359-3364 (2010).
131. Zhou, W., Shao, Z., Ran, R., Zeng, P., Gu, H., Jin, W., & Xu, N.

$Ba_{0.5}Sr_{0.5}Co_{0.8}Fe_{0.2}O_{3-\delta}$ + $LaCoO_3$ composite cathode for $Sm_{0.2}Ce_{0.8}O_{1.9}$-electrolyte based intermediate-temperature solid-oxide fuel cells. *Journal of Power Sources*, *168*(2), 330-337 (2007).

132. Zhou, W., Shao, Z., Ran, R., Gu, H., Jin, W., & Xu, N. LSCF nanopowder from Cellulose–Glycine-Nitrate process and its application in Intermediate-Temperature Solid-Oxide fuel cells. *Journal of the American Ceramic Society*, *91*(4), 1155-1162 (2008).
133. Grimaud, A., Mauvy, F., Bassat, J. M., Fourcade, S., Rocheron, L., Marrony, M., & Grenier, J. C. Hydration properties and rate determining steps of the oxygen reduction reaction of perovskite-related oxides as H^+-SOFC cathodes. *Journal of The Electrochemical Society*, *159*(6), B683 (2012).
134. Grimaud, A., Diaz-Morales, O., Han, B., Hong, W. T., Lee, Y. L., Giordano, L., *et al*. Activating lattice oxygen redox reactions in metal oxides to catalyse oxygen evolution. *Nature Chemistry*, *9*(5), 457-465 (2017).
135. Suntivich, J., May, K. J., Gasteiger, H. A., Goodenough, J. B., & Shao-Horn, Y. A perovskite oxide optimized for oxygen evolution catalysis from molecular orbital principles. *Science*, *334*(6061), 1383-1385 (2011).
136. Grimaud, A., May, K. J., Carlton, C. E., Lee, Y. L., Risch, M., Hong, W. T., *et al*. Double perovskites as a family of highly active catalysts for oxygen evolution in alkaline solution. *Nature Communications*, *4*, 2439 (2013).
137. Calle-Vallejo, F., Díaz-Morales, O. A., Kolb, M. J., & Koper, M. T. Why is bulk thermochemistry a good descriptor for the electrocatalytic activity of transition metal oxides?. *ACS Catalysis*, *5*(2), 869-873 (2015).
138. Rong, X., Parolin, J., & Kolpak, A. M. A fundamental relationship between reaction mechanism and stability in metal oxide catalysts for oxygen evolution. *Acs Catalysis*, *6*(2), 1153-1158 (2016).
139. Yagi, S., Yamada, I., Tsukasaki, H., Seno, A., Murakami, M., Fujii, H., *et al*. Covalency-reinforced oxygen evolution reaction catalyst. *Nature Communications*, *6*, 8249 (2015).
140. Yamada, I., Takamatsu, A., Asai, K., Shirakawa, T., Ohzuku, H., Seno, A., *et al*. Systematic study of descriptors for oxygen evolution reaction catalysis in perovskite oxides. *The Journal of Physical Chemistry C*, *122*(49), 27885-27892 (2018).
141. Weller, M. T., & Skinner, S. J. Ba3Mn2O8 determined from neutron powder diffraction. *Acta Crystallographica Section C: Crystal Structure Communications*, *55*(2), 154-156 (1999).
142. Wu, W., Ding, D., & He, T. Development of high performance intermediate temperature proton-conducting solid oxide electrolysis cells. *ECS Transactions*, *80*(9), 167 (2017).

143. Yang, S., Wen, Y., Zhang, J., Lu, Y., Ye, X., & Wen, Z. Electrochemical performance and stability of cobalt-free $Ln_{1.2}Sr_{0.8}NiO_4$ (Ln= La and Pr) air electrodes for proton-conducting reversible solid oxide cells. *Electrochimica Acta*, *267*, 269-277 (2018).
144. Jeong, S., Yamaguchi, T., Okamoto, M., Zhu, C., Habazaki, H., Nagayama, M., & Aoki, Y. Proton pumping boosts energy conversion in hydrogen-permeable metal-supported protonic fuel cells. *ACS Applied Energy Materials*, *3*(1), 1222-1234 (2019).
145. Jeong, S., Wang, N., Kitano, S., Habazaki, H., & Aoki, Y. Metal/Oxide Heterojunction Boosts Fuel Cell Cathode Reaction at Low Temperatures. *Advanced Energy Materials*, *11*(37), 2102025 (2021).
146. Li, J., Yoon, H., & Wachsman, E. D. Hydrogen permeation through thin supported $SrCe_{0.7}Zr_{0.2}Eu_{0.1}O_{3-\delta}$ membranes; dependence of flux on defect equilibria and operating conditions. *Journal of Membrane Science*, *381*(1-2), 126-131 (2011).
147. Kim, J. H., Kang, Y. M., Kim, B. G., Lee, S. H., & Hwang, K. T. Preparation of dense composite membrane with Ba-cerate conducting oxide and rapidly solidified Zr-based alloy. *International Journal of Hydrogen Energy*, *36*(16), 10129-10135 (2011).
148. Oh, T. K., Yoon, H., & Wachsman, E. D. Effect of Eu dopant concentration in SrCe1− xEuxO3− δ on ambipolar conductivity. *Solid State Ionics*, *180*(23-25), 1233-1239 (2009).
149. Zhan, S., Zhu, X., Ji, B., Wang, W., Zhang, X., Wang, J., *et al*. Preparation and hydrogen permeation of $SrCe_{0.95}Y_{0.05}O_{3-\delta}$ asymmetrical membranes. *Journal of Membrane Science*, *340*(1-2), 241-248 (2009).
150. Steinsvik, S., Larring, Y., & Norby, T. Hydrogen Ion Conduction in Iron-Substituted Strontium Titanate, $SrTi_{1-x}Fe_xO_{3-x/2}$ ($0 \leq x \leq 0.8$). *Solid State Ionics*, *143*(1), 103-116 (2001).
151. Poulsen, F. W. Speculations on the existence of hydride ions in proton conducting oxides. *Solid State Ionics*, *145*(1-4), 387-397 (2001).
152. STEINSVIK, S., BUGGE, R., GjØNnes, J. O. N., TAFTØ, J., & Norby, T. The Defect Structure of $SrTi_{1-x}FexO_{3-y}$ (x = 0–0.8) Investigated by Electrical Conductivity Measurements and Electron Energy Loss Spectroscopy (EELS). *Journal of Physics and Chemistry of Solids*, *58*(6), 969-976 (1997).
153. Kobayashi, G., Hinuma, Y., Matsuoka, S., Watanabe, A., Iqbal, M., Hirayama, M., *et al*. Pure H^- conduction in oxyhydrides. *Science*, *351*(6279), 1314-1317 (2016).
154. Takeiri, F., Watanabe, A., Kuwabara, A., Nawaz, H., Ayu, N. I. P., Yonemura, M., *et al*. Ba_2ScHO_3: H^- conductive layered oxyhydride with H^- site selectivity. *Inorganic Chemistry*, *58*(7), 4431-4436 (2019).

155. Nawaz, H., Takeiri, F., Kuwabara, A., Yonemura, M., & Kobayashi, G. Synthesis and H^- conductivity of a new oxyhydride Ba_2YHO_3 with anion-ordered rock-salt layers. *Chemical Communications*, *56*(71), 10373-10376 (2020).

156. Ubukata, H., Broux, T., Takeiri, F., Shitara, K., Yamashita, H., Kuwabara, A., *et al*. Hydride conductivity in an anion-ordered fluorite structure LnHO with an enlarged bottleneck. *Chemistry of Materials*, *31*(18), 7360-7366 (2019).

157. Iwasaki, Y., Matsui, N., Suzuki, K., Hinuma, Y., Yonemura, M., Kobayashi, G., *et al*. Synthesis, crystal structure, and ionic conductivity of hydride ion-conducting Ln_2LiHO_3 (Ln = La, Pr, Nd) oxyhydrides. *Journal of Materials Chemistry A*, *6*(46), 23457-23463 (2018).

158. Ooya, K., Li, J., Fukui, K., Iimura, S., Nakao, T., Ogasawara, K., *et al*. Ruthenium Catalysts Promoted by Lanthanide Oxyhydrides with High Hydride-Ion Mobility for Low-Temperature Ammonia Synthesis. *Advanced Energy Materials*, *11*(4), 2003723 (2021).

159. Matsui, N., Hinuma, Y., Iwasaki, Y., Suzuki, K., Guangzhong, J., Nawaz, H., *et al*. The effect of cation size on hydride-ion conduction in $LnSrLiH_2O_2$ (Ln = La, Pr, Nd, Sm, Gd) oxyhydrides. *Journal of Materials Chemistry A*, *8*(46), 24685-24694 (2020).

160. Takeiri, F., Watanabe, A., Okamoto, K., Bresser, D., Lyonnard, S., Frick, B., *et al*. Hydride-ion-conducting K_2NiF_4-type Ba–Li oxyhydride solid electrolyte. *Nature Materials*, *21*(3), 325-330 (2022).

161. Kobayashi, Y., Hernandez, O. J., Sakaguchi, T., Yajima, T., Roisnel, T., Tsujimoto, Y., *et al*. An oxyhydride of BaTiO3 exhibiting hydride exchange and electronic conductivity. *Nature Materials*, *11*(6), 507-511 (2012).

162. Tang, Y., Kobayashi, Y., Shitara, K., Konishi, A., Kuwabara, A., Nakashima, T., *et al*. On hydride diffusion in transition metal perovskite oxyhydrides investigated via deuterium exchange. *Chemistry of Materials*, *29*(19), 8187-8194 (2017).

163. Uchimura, T., Takeiri, F., Okamoto, K., Saito, T., Kamiyama, T., & Kobayashi, G. Direct synthesis of barium titanium oxyhydride for use as a hydrogen permeable electrode. *Journal of Materials Chemistry A*, *9*(36), 20371-20374 (2021).

Chapter 2

Evaluation of protonic solid oxide steam electrolysis cell with Zr-rich side $BaZr_{0.6}Ce_{0.2}Y_{0.2}O_{3-\delta}$ electrolyte

2.1. Objective of chapter 2

As mentioned in the chapter 1, $BaZr_xCe_{1-x-y}M_yO_{3-\delta}$ (BZCM; M=Y, Yb, etc.) ceramics in Zr-rich side composition, i.e., $x > 0.4$ normally needs to be sintered at temperatures over 1600°C for sufficient grain growth and densification because of their high refractory nature [1]. Such high temperature sintering cause loss of Ba contents by vaporization, resulting in the deterioration of ion conductivity (vapor pressure of BaO is about 1.4×10^{-6} atm at 1400°C [2]). Recently, Jeong et al. reported the successful fabrication of thin film fuel cells based on high Zr content $BaZr_xCe_{1-x}Y_{0.2}O_3$ ($x > 0.4$) electrolyte by one step cofiring process at 1400°C [3] with a sintering aid of $Zn(NO_3)_2$. In this chapter, I first aimed to fabricate porous cermet supported thin film H-SOEC with $BaZr_{0.6}Ce_{0.2}Y_{0.2}O_{3-\delta}$ (BZCY622) electrolyte by similar technique. Recently, Tang et al. reported that the ohmic loss and anode polarization resistances of H-SOECs using the $BaZr_xCe_{0.8-x}Y_{0.1}Yb_{0.1}O_{3-\delta}$ ($x = 0.6$) can be significantly improved by introducing 40-nm-thick $La_{0.5}Sr_{0.5}CoO_{3-\delta}$ (LSC) thin films at the anode/electrolyte interface [4]. Such an interlayer call anode functional layer (AFL). For the second objective, I examined the effect of LSC AFL on the electrolysis current and Faradaic efficiency of BZCY622 base H-SOEC.

2.2. Experimental

2.2.1. Materials Preparation

In this experiment, BZCY622 thin film cells were also fabricated using a similar process as reported by Jeong et al [2]. The raw mixture of BZCY622 was prepared by mixing stoichiometric amounts of

$BaCO_3$ (High Purity Chemicals, 99.95%), CeO_2 (High Purity Chemicals, 99.99%), ZrO_2 (High Purity Chemicals, 98%), Y_2O_3 (High Purity Chemicals, 99.99%), and $Zn(NO_3)_2 \cdot 6H_2O$ (Wako Chemicals; 99.9%) additives as a sintering aid. The amount of additive was adjusted to a Zn/Ba molar ratio of 0.03. The starting materials were dispersed in ethanol, ball-milled for 24 h, and dried at 80°C. A BZCY622 raw mixture and NiO were mixed in ethanol at a weight ratio of 40:60. After drying, the resultant mixed powders were uniaxially pressed under 20 MPa and isostatically pressed under a hydrostatic pressure of 100 MPa to obtain green pellets (12 mm ϕ, 1.6–1.8 mm d) for Ni-BZCY622 cermet cathode supports. The precursor layers of the electrolyte films were spin-coated on the green pellets using a MISAKA 1H-D7 spin coater. The slurry was prepared by dispersing the BZCY622 raw mixture in a solution containing a dispersant (20 wt % polyethyleneimine (M_w = 28 000) dissolved in α-terpineol) and a binder (5 wt % surfactant dissolved in α-terpineol) at a weight ratio of 10:3:1. The mixture was spin-coated once or twice on the surfaces of the green pellets at 3000 rpm for 30 s. After spin coating, the pellets were dried at room temperature and cofired at 1400°C for 12 h to form half-cells. The backside of the sintered pellet was polished with SiC paper.

The LSC AFL was deposited on the electrolyte surface by radio frequency (RF) magnetron sputtering with an LSC target. RF sputtering was performed at a sputtering power of 50 W under a flow of 4%-O_2/Ar gas at 50 cm^3 min^{-1} while the substrate temperature was maintained at 500°C. Last, the $La_{0.6}Sr_{0.4}Co_{0.2}Fe_{0.8}O_{3-\delta}$ (LSCF) anode was screen-printed using an LSCF commercial ink (Fuel Cell Materials).

The phase purity was checked by X-ray diffraction (XRD) analysis in the 2θ range between 20° and 80° at a scan rate of 5° min^{-1} using a Rigaku Ultima IV (Cu Kα radiation). The microstructures of the fabricated cells were examined using a field emission scanning electron microscope (FESEM; SIGMA500, ZEISS) operated at 3 kV.

2.2.2. Electrochemical Measurements

Prior to conducting electrochemical measurements, the cathode side was exposed to a humidified 50%-H_2/Ar gas mix at 700°C for 6 h to convert NiO to metallic Ni and produce a porous Ni-BZCY622 cermet cathode. Steam electrolysis performance of cells was evaluated at 700 and 600°C with a wet 10%-H_2/Ar gas mix to the cathode and a 20%-H_2O/air mix to the anode. The 20%-H_2O/air mixture was prepared by passing air through a water bath maintained at approximately 60°C and subsequently supplied to the anode chamber through a stainless-steel tube heated at 150°C using a ribbon heater to prevent condensation. The *I–V* characteristics were measured using an electrochemical station (Biologic SP-300). The electrochemical impedance spectra of the SOECs were determined using a frequency response analyzer (Biologic SP-300) with a frequency range of 10^6 to 0.1 Hz and an AC amplitude of 30 mV. The hydrogen evolution rates (v) in the cathode were quantified by analyzing the cathode exhaust gas using gas chromatography (490 Micro GC, Agilent Technologies). The Faradaic efficiency, η, was calculated using the observed and theoretical hydrogen evolution rates (v_{meas} and v_{theo}, respectively) using the following equation:

$$\eta = \frac{v_{\text{meas}}}{v_{\text{theo}}} \times 100 = \frac{v_{\text{meas}}}{I \times (z \times F)^{-1}} \times 100\ (\%) \qquad (2\text{-}1)$$

where I is the applied current, z is the electron transport number of steam electrolysis, and F is Faraday's constant (96485 C mol^{-1}).

2.3. Results and Discussion

2.3.1. Morphology of Prepared Materials

Figure 2-1 shows the powder XRD pattern of pulverized thin film cell before screen printing the LSCF anodes (half-cell). Results show that all of the peaks generated during the XRD analysis were from NiO and BZCY622 phases, while the BaY_2NiO_5 secondary phase [5] was not observed. This confirms that the reaction between BZCY622 and NiO to produce BaY_2NiO_5 does not occur.

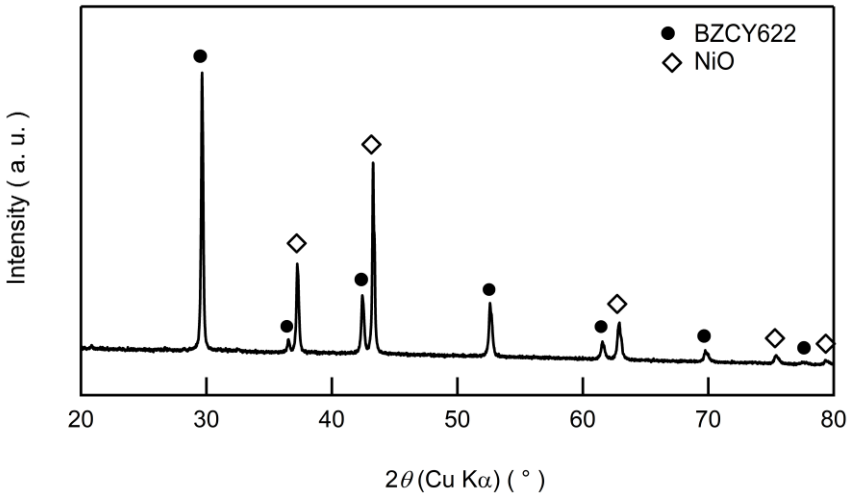

Figure 2-1. XRD pattern of pulverized half cells.

Figure 2-2a and 2b show the cross-sectional SEM images of H-SOEC with BZCY622 films prepared by spin-coating once and twice, respectively, after H_2 reduction of the cermet cathode. The cermet cathode is extremely porous with interconnected macropore networks that act as gas diffusion paths. The films prepared by spin-coating once and twice have a thickness of 15 and 30 μm, respectively, both of which are highly dense and formed uniformly over a porous cermet cathode. The LSCF anode is a porous layer composed of 50 nm diameter particles with a thickness of ~40 μm. Figure 2-2c shows the SEM image of the BZCY622 thin film bare surface on the porous Ni-BZCY662 cermet cathode after H_2 reduction at 700°C. The BZCY622 electrolyte layer maintains dense matrices without any crack formation and pinholes after reduction. This implies that the electrolyte film maintains adequate gas tightness. The BZCY622 grains grew up to 5 μm in diameter, which is larger than the BZCY622 grain size prepared by the sol–gel method [6]. Figure 2-2d and e show cross-sectional and surface SEM images of the LSC AFL on the BZCY622 thin film. The 40-nm-thick LSC layer, comprised of the nanoparticles with about 10 nm diameters, fully covers the electrolyte surface.

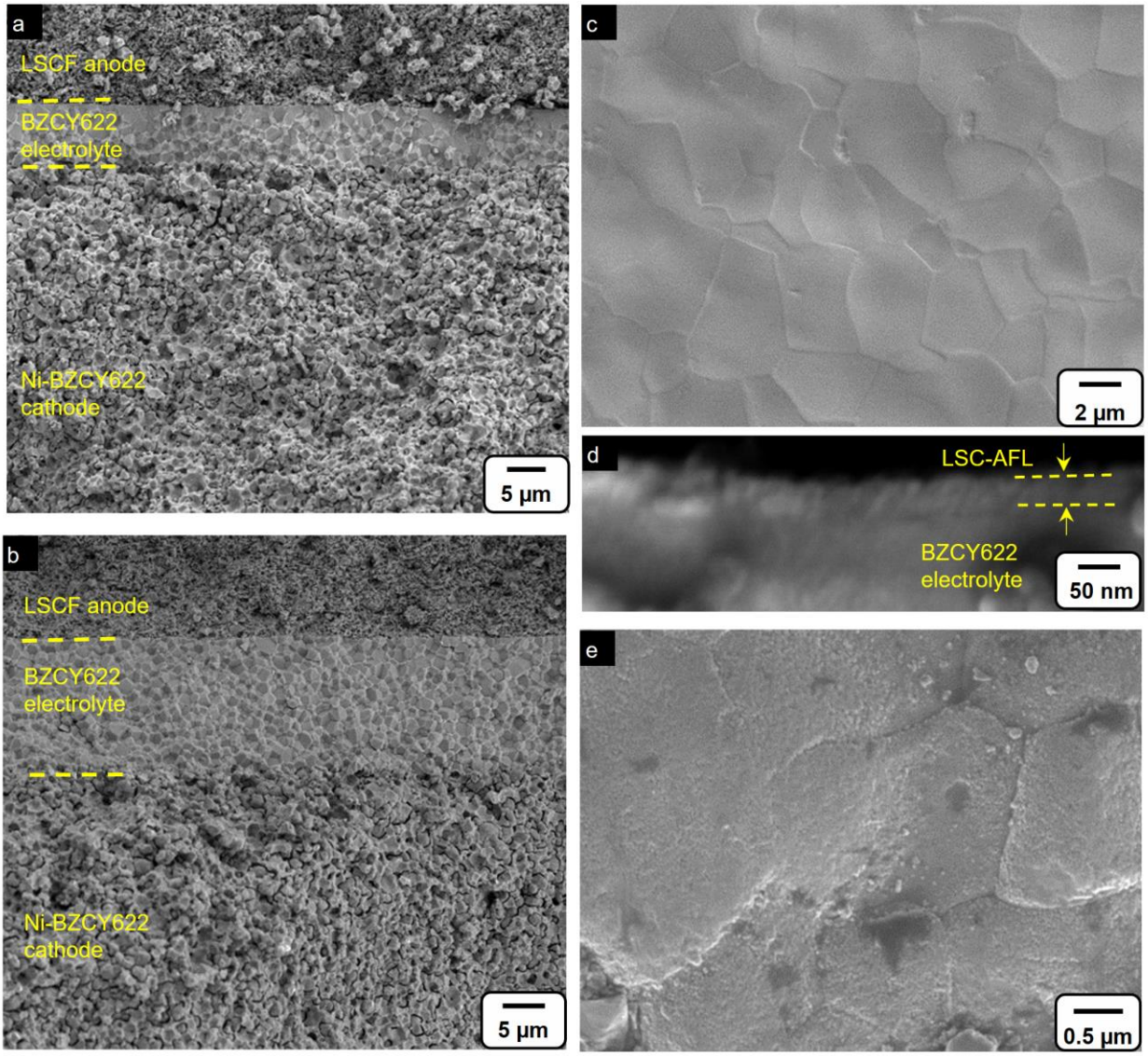

Figure 2-2. (a,b) Cross-sectional SEM image of cermet support H-SOEC with BZCY622 electrolyte films prepared by (a) once and (b) twice spin-coating. (c) Surface SEM image of BZCY622 electrolyte film prepared by once spin-coating. (d) Cross-sectional and (e) surface SEM images of LSC-AFL deposited on BZCY622 electrolyte.

2.3.2. Electrochemical Measurements

Figure 2-3 shows the current–voltage (*I–V*) curves for the cell without the AFL, i.e., {20%-H_2O/air, LSCF | BZCY622 (15 μm) | Ni-BZCY622, wet 10%-H_2/Ar}, at 700, 600 and 500°C. Open circuit voltage (OCV) at 700 and 600°C are measured to be 0.84 and 0.91 V, respectively, which is lower than the ideal value of 0.93 and 0.96 V. The relatively low OCV value for the current cells must be attributed to the partial hole conductivity of BZCY622. On the basis of the theoretical OCV of 0.93 V as calculated by the Nernst equation, the proton transport number of BZCY622 films can be roughly estimated to 0.89, which is in agreement with the proton transfer number of $BaZr_{0.7}Ce_{0.1}Y_{0.2}O_{3-\delta}$ (< 0.9) [7] at 700°C under $pO_2 \geq 0.01$. This clearly indicates that leakage by hole conduction occurs on the BZCY662 thin film at a relatively high temperature. The cells without AFL exhibited electrolysis currents of 0.92, 0.47 and 0.15 A cm^{-2} at 700, 600 and 500°C, respectively, at a 1.3 V bias. The OCV of the cell with AFL, i.e., {20%-H_2O/air, LSCF | LSC/BZCY622 (15 μm) | Ni-BZCY622, wet 10%-H_2/Ar}, is comparable to the results observed in cells without the AFL–OCV values are 0.82 and 0.92 V at 700 and 600°C, respectively. However, at 1.3 V, the electrolysis currents at 700, 600 and 500°C are 1.43, 0.87 and 0.33 A cm^{-2}, respectively, which are nearly twice higher than the corresponding values of the cells without AFL. The electrolysis current of the cell with the LSC-AFL at 600°C is similar to or higher than that of the H-SOECs using a Ce-rich side $BaZr_xCe_{1-x-y}M_yO_{3-\delta}$ (M = Yb, Y, Co; $x \sim 0.1$) thin film electrolyte at 1.3 V under similar conditions [8-11]. However, the electrolysis currents at 500°C are far from the target of 1 A cm^{-2}.

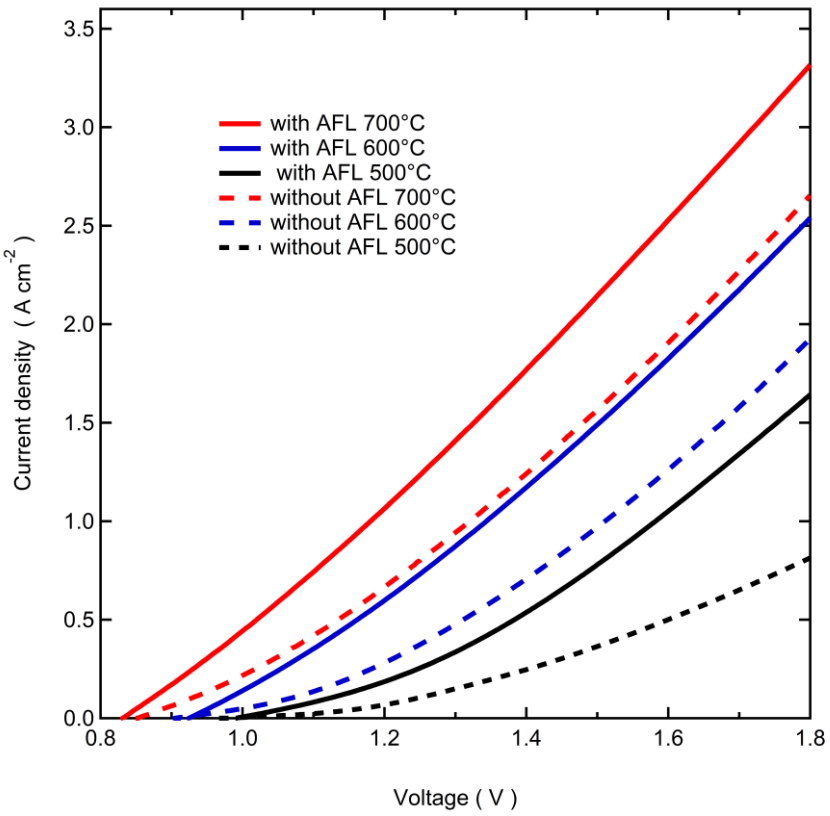

Figure 2-3. Performance (*I–V* curves) of the H-SOEC using 15 μm-thick BZCY622 film with and without LSC-AFL. Solid and dotted lines indicate the cell with and without LSC, respectively, and red, blue, and black denote 700°C, 600°C and 500°C, respectively.

Figure 2-4a and 4b show the AC impedance spectra for the cells of 15-μm-thick electrolyte with and without the AFL at 600°C subjected to different DC conditions. In the H-SOECs spectra, the high-frequency *x* intercept is normally attributed to the electrolyte's ohmic resistances (R_O), while the succeeding arcs denote the interfacial polarization mainly because of the anode reactions [12,13]. The R_O of the cells without and with the AFL at 600°C under OCV conditions are 0.81 Ω cm^2 and 0.30 Ω cm^2, respectively. This feature indicates that the R_O related to proton conduction efficiently decreases with the use of the AFL. Moreover, the R_O of H-SOEC was found to include the protonic resistances near the anode/electrolyte interfaces together with the bulk resistance of the electrolyte film. To separate interfacial resistance from bulk resistance of the electrolyte, the R_O is evaluated for the cells with different thicknesses of electrolyte films (Figure 2-4c). The R_O at 600°C of the cell without AFL increases from 0.81 to 0.92 Ω cm^2 when the thickness of the electrolyte increases from 15 to 30 μm. Assuming the linear dependence of R_O on electrolyte thickness reveals the existence of an R_O of about 0.7 Ω cm^2 at zero thickness. Recent studies reported that proton-conducting solid oxide fuel cells (H-SOFCs) possess large impedances (~10^5 Hz) due to slow proton transfer at the gas–anode–electrolyte TPB [14-18]. On the basis of these, the BZCY622 cells involve relatively large resistances related to the interfacial proton transfer from the electrolyte to the anode. The value estimated for the zero-thickness electrolyte cell without AFL, i.e., 0.7 Ω cm^2, is comparable to 80% of R_O for the 15-μm-thick electrolyte cell without AFL (0.81 Ω cm^2), which confirms that the interfacial resistances are a dominant component in the R_O of the BZCY622 base cells. The R_O for the 15-μm-thick electrolyte cells with AFL is only 0.30 Ω cm^2, which is much smaller than the value of the corresponding cell without AFL. These results unambiguously demonstrate that interfacial resistance is significantly reduced with the use of LSC–AFL.

The polarization resistances (R_p) are approximated using the total diameter of the impedance arcs. The calculated values for the cells without and with the AFL under OCV are 0.29 Ω cm^2 and 0.95 Ω cm^2, respectively. The R_p reduction caused by the AFL is more evident with the DC outputs.

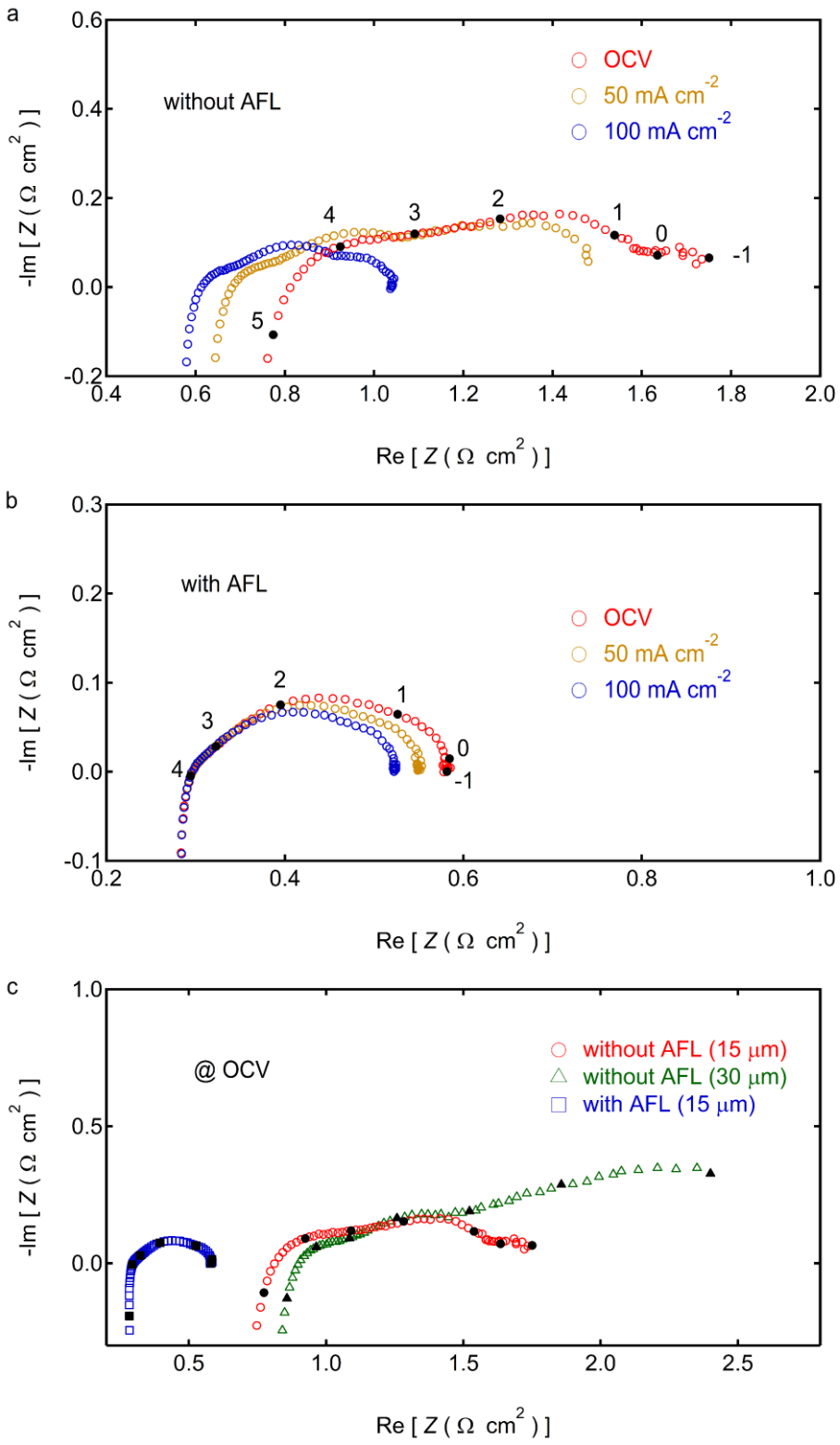

Figure 2-4. AC impedance spectra for H-SOEC of 15 μm-thick electrolyte (a) without and (b) with LSC-AFL, measured at 600°C under various DC conditions. (c) AC impedance spectra of H-SOEC of 15 μm-thick electrolyte without (red, ○) and with LSC-AFL (blue, □), and of 30 μm-thick electrolyte without LSC-AFL (green, △). In (a)-(c), digits show the frequencies at each blacken points in the spectra.

The R_p values with the AFL are 0.26 Ω cm^2 and 0.23 Ω cm^2 under a DC current of 50 and 100 mA cm^{-2}, respectively. These values are observed to be smaller by a factor of 0.33 and 0.53 than the values without the AFL. The results indicate that the LSC AFL can facilitate both interfacial proton transfer and other cathode reaction steps, such as charge transfer to adsorbed oxygen and/or oxygen desorption at the TPB.

The hydrogen production rate was calibrated using gas chromatography under galvanostatic electrolysis at 200 mA cm^{-2} and 400 mA cm^{-2}. Figure 2-5 illustrates the cell voltage transients, hydrogen evolution rate (v_{meas}), and Faradaic efficiency (η) at 600 and 700°C. The first electrolysis was conducted at 200 mA cm^{-2} for 30 min and at 400 mA cm^{-2} for 30 min subsequently. The voltages for cells without AFL are observed to be stable at 0.91 to 0.98 V during the electrolysis at 700°C using 200 mA cm^{-2} and 400 mA cm^{-2}, respectively. Higher cell voltage is observed at 600°C compared to the cell voltage at 700°C. This is primarily due to the increase in total cell resistance ($R_O + R_p$) with decreasing temperature. The cell voltage is 1.15 and 1.26 V at 200 mA cm^{-2} and 400 mA cm^{-2}, respectively. The nominal overpotentials, defined by the gap between the cell bias and the OCV, are equal to 0.24 and 0.36 for electrolysis at 600°C in 200 mA cm^{-2} and 400 mA cm^{-2}, respectively. v_{meas} achieves equilibrium within 20 min upon applying a constant current during electrolysis at 700 and 600°C. v_{meas} without the AFL is measured to be 3.6×10^{-5} mol cm^{-2} min^{-1} and 6.9×10^{-5} mol cm^{-2} min^{-1}, and η values of 58% and 56% were acquired for electrolysis conducted at 600°C using 200 mA cm^{-2} and 400 mA cm^{-2}, respectively. Similar results for v_{meas} and η at 700°C are observed under equilibrium conditions. These η results are consistent with the values reported in previous studies for H-SOECs with an acceptor-doped BZCM electrolyte [19-22,3,14,23-26]. Vøllestad et al. determined the theoretical Faradaic efficiency of H-SOEC with $BaZr_{0.1}Ce_{0.7}Y_{0.1}Yb_{0.1}O_{3-\delta}$ under different hydrogen partial pressures (p_{H2}) and water partial pressures (p_{H2O}) [26]. The approach employed numerical and experimental techniques and concluded that the efficiency is less than 70% when the anode's p_{H2O} and cathode's p_{H2} are below 100 kPa. Hole carrier concentration in the electrolyte is also

found above zero under similar conditions. These results confirm that the cells in this study conduct steam electrolysis and exhibited moderate Faradaic efficiency.

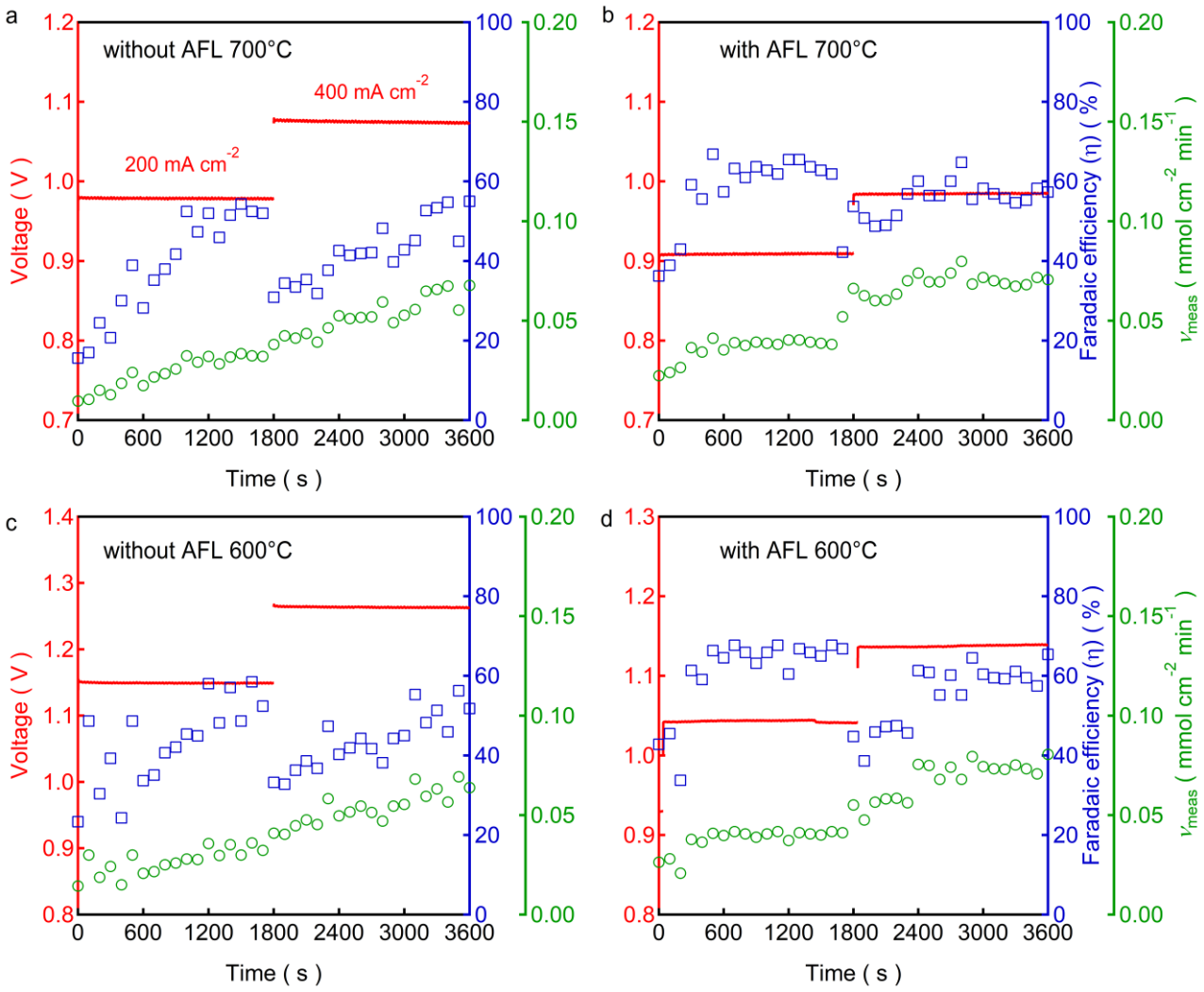

Figure 2-5. Faradaic efficiency (η) (blue, □), hydrogen evolution rate (v_{meas}) (green, ○) and cell voltage (red line) of (a,c) LSCF | BZCY622 (15 μm) | Ni-BZCY622 and (b,d) LSCF | LSC | BZCY622 (15 μm) | Ni-BZCY622 electrolysis cells at 600ºC and 700ºC under galvanostatic conditions at 200 and 400 mA cm^{-2}.

The cells with the LSC AFL exhibit stable voltages of 0.91 and 0.98 V at 700°C for the galvanostatic electrolysis in 200 mA cm^{-2} and 400 mA cm^{-2}, respectively. In contrast, 1.04 and 1.14 V are observed at 600°C under similar conditions. The cell overpotentials with the AFL at 600°C are calculated to 0.12 and 0.21 for electrolysis under 200 mA cm^{-2} and 400 mA cm^{-2}, respectively. This is approximately 49 and 59%, respectively, of the corresponding values for cells without the AFL. v_{meas} with the AFL reaches 4.1×10^{-5} mol cm^{-2} min^{-1} and 8.1×10^{-5} mol cm^{-2} min^{-1} for electrolysis at 600°C using 200 mA cm^{-2} and 400 mA cm^{-2}, respectively. The values are comparable with the results for cells without the AFL. In addition, η values are 67 and 65% for electrolysis at 600°C using 200 mA cm^{-2} and 400 mA cm^{-2}, respectively. These results demonstrate that LSC AFL lowers the overpotentials of H-SOEC efficiently by promoting interfacial proton transfer and anode reactions without increasing the hole leakage current. It was demonstrated in this study that the introduction of the AFL is an efficient way to improve the performance of H-SOEC-based Zr-rich side BZCY electrolytes. The results of this research demonstrate opportunities for future research on optimal AFL materials with excellent durability and high efficiency for H-SOECs.

2.4. Conclusions

H-SOECs with high Zr-content BZCY622 electrolyte were successfully fabricated by solid-state reactive sintering method with $Zn(NO_3)_2$ additives by a single sintering step at 1400°C. The cell with the 40-nm-thick LSC AFL can generate an electrolysis current of 0.87 A cm^{-2} at 600°C at 1.3 V. This is nearly twice higher than that of the cell without the AFL. The cells without the AFL at 600°C in OCV have ohmic resistance and polarization resistances of 0.81 Ω cm^2 and 0.95 Ω cm^2, respectively. Conversely, cells with the LSC AFL exhibited lower ohmic and polarization resistances of 0.30 Ω cm^2 and 0.29 Ω cm^2, respectively. The addition of AFL efficiently promoted interfacial proton transfer at the electrolyte/anode interface and corresponding anode reactions. The Faradaic efficiency was limited to ~65% at 600°C despite a use of LSC AFL.

2.5. References

1. Lindman, A., Helgee, E. E., & Wahnstrom, G. Comparison of space-charge formation at grain boundaries in proton-conducting $BaZrO_3$ and $BaCeO_3$. *Chemistry of Materials*, *29*(18), 7931-7941 (2017).
2. Inghram, M. G., Chupka, W. A., & Porter, R. F. Mass spectrometric study of barium oxide vapor. *The Journal of Chemical Physics*, *23*(11), 2159-2165 (1955).
3. Jeong, S., Kobayashi, T., Kuroda, K., Kwon, H., Zhu, C., Habazaki, H., & Aoki, Y. Evaluation of thin film fuel cells with Zr-rich $BaZr_xCe_{0.8-x}Y_{0.2}O_{3-\delta}$ electrolytes ($x \geq 0.4$) fabricated by a single-step reactive sintering method. *RSC Advances*, *8*(46), 26309-26317 (2018).
4. Tang, C., Akimoto, K., Wang, N., Fadillah, L., Kitano, S., Habazaki, H., & Aoki, Y. The effect of an anode functional layer on the steam electrolysis performances of protonic solid oxide cells. *Journal of Materials Chemistry A*, *9*(24), 14032-14042 (2021).
5. Tong, J., Clark, D., Bernau, L., Sanders, M., & O'Hayre, R. Solid-state reactive sintering mechanism for large-grained yttrium-doped barium zirconate proton conducting ceramics. *Journal of Materials Chemistry*, *20*(30), 6333-6341 (2010).
6. Bi, L., Shafi, S. P., & Traversa, E. Y-doped $BaZrO_3$ as a chemically stable electrolyte for proton-conducting solid oxide electrolysis cells (SOECs). *Journal of Materials Chemistry A*, *3*(11), 5815-5819 (2015).
7. Heras-Juaristi, G., Pérez-Coll, D., & Mather, G. C. Temperature dependence of partial conductivities of the $BaZr_{0.7}Ce_{0.2}Y_{0.1}O_{3-\delta}$ proton conductor. *Journal of Power Sources*, *364*, 52-60 (2017).
8. Azimova, M. A., & McIntosh, S. On the reversibility of anode supported proton conducting solid oxide cells. *Solid State Ionics*, *203*(1), 57-61 (2011).
9. Kim, J., Jun, A., Gwon, O., Yoo, S., Liu, M., Shin, J., *et al.* Hybrid-solid oxide electrolysis cell: A new strategy for efficient hydrogen production. *Nano Energy*, *44*, 121-126 (2018).
10. Wu, W., Ding, H., Zhang, Y., Ding, Y., Katiyar, P., Majumdar, P. K., *et al.* 3D self-architectured steam electrode enabled efficient and durable hydrogen production in a proton-conducting solid oxide electrolysis cell at temperatures lower than 600°C. *Advanced Science*, *5*(11), 1800360 (2018).
11. Li, W., Guan, B., Ma, L., Hu, S., Zhang, N., & Liu, X. High performing triple-conductive $Pr_2NiO_{4+\delta}$ anode for proton-conducting steam solid oxide electrolysis cell. *Journal of Materials Chemistry A*, *6*(37), 18057-18066 (2018).
12. Lin, J., Chen, L., Liu, T., Xia, C., Chen, C., & Zhan, Z. The beneficial effects of straight open large pores in the support on steam electrolysis performance of electrode-supported solid oxide

electrolysis cell. *Journal of Power Sources*, *374*, 175-180 (2018).

13. Huan, D., Shi, N., Zhang, L., Tan, W., Xie, Y., Wang, W., *et al.* New, efficient, and reliable air electrode material for proton-conducting reversible solid oxide cells. *ACS Applied Materials & Interfaces*, *10*(2), 1761-1770 (2018).
14. He, F., Wu, T., Peng, R., & Xia, C. Cathode reaction models and performance analysis of $Sm_{0.5}Sr_{0.5}CoO_{3-\delta}$–$BaCe_{0.8}Sm_{0.2}O_{3-\delta}$ composite cathode for solid oxide fuel cells with proton conducting electrolyte. *Journal of Power Sources*, *194*(1), 263-268 (2009).
15. Wu, T., Zhao, Y., Peng, R., & Xia, C. Nano-sized $Sm_{0.5}Sr_{0.5}CoO_{3-\delta}$ as the cathode for solid oxide fuel cells with proton-conducting electrolytes of $BaCe_{0.8}Sm_{0.2}O_{2.9}$. *Electrochimica acta*, *54*(21), 4888-4892. (2009).
16. Dailly, J., Mauvy, F., Marrony, M., Pouchard, M., & Grenier, J. C. Electrochemical properties of perovskite and A_2MO_4-type oxides used as cathodes in protonic ceramic half cells. *Journal of Solid State Electrochemistry*, *15*(2), 245-251 (2011).
17. Ricote, S., Bonanos, N., Rørvik, P. M., & Haavik, C. Microstructure and performance of $La_{0.58}Sr_{0.4}Co_{0.2}Fe_{0.8}O_{3-\delta}$ cathodes deposited on $BaCe_{0.2}Zr_{0.7}Y_{0.1}O_{3-\delta}$ by infiltration and spray pyrolysis. *Journal of Power Sources*, *209*, 172-179 (2012).
18. Jeong, S., Wang, N., Kitano, S., Habazaki, H., & Aoki, Y. Metal/Oxide Heterojunction Boosts Fuel Cell Cathode Reaction at Low Temperatures. *Advanced Energy Materials*, *11*(37), 2102025 (2021).
19. Zhu, H., Ricote, S., & Kee, R. J. Faradaic efficiency in protonic-ceramic electrolysis cells. *Journal of Physics: Energy*, *4*(1), 014002 (2022).
20. Wang, W., Medvedev, D., & Shao, Z. Gas humidification impact on the properties and performance of perovskite-type functional materials in proton-conducting solid oxide cells. *Advanced Functional Materials*, *28*(48), 1802592 (2018).
21. Su, H., & Hu, Y. H. Degradation issues and stabilization strategies of protonic ceramic electrolysis cells for steam electrolysis. *Energy Science & Engineering*, *10*(5), 1706-1725 (2022).
22. Lei, L., Zhang, J., Yuan, Z., Liu, J., Ni, M., & Chen, F. Progress report on proton conducting solid oxide electrolysis cells. *Advanced Functional Materials*, *29*(37), 1903805 (2019).
23. Duan, C., Kee, R., Zhu, H., Sullivan, N., Zhu, L., Bian, L., *et al.* Highly efficient reversible protonic ceramic electrochemical cells for power generation and fuel production. *Nature Energy*, *4*(3), 230-240 (2019).
24. Lei, L., Zhang, J., Guan, R., Liu, J., Chen, F., & Tao, Z. Energy storage and hydrogen

production by proton conducting solid oxide electrolysis cells with a novel heterogeneous design. *Energy Conversion and Management*, *218*, 113044. (2020).

25. Wrubel, J. A., Gifford, J., Ma, Z., Ding, H., Ding, D., & Zhu, T. Modeling the performance and faradaic efficiency of solid oxide electrolysis cells using doped barium zirconate perovskite electrolytes. *International Journal of Hydrogen Energy*, *46*(21), 11511-11522 (2021).
26. Vøllestad, E., Strandbakke, R., Tarach, M., Catalán-Martínez, D., Fontaine, M. L., Beeaff, D., & Norby, T. Mixed proton and electron conducting double perovskite anodes for stable and efficient tubular proton ceramic electrolysers. *Nature Materials*, *18*(7), 752-759 (2019).

Chapter 3

Efficient anode based on high-valence-state manganate(V) $Ba_3Mn_2O_8$

3.1. Objective of chapter 3

The decrease of the anodic overpotentials is important for improving of Faradaic efficiency, as mentioned in chapter 1. Protonic solid oxide electrolysis cell (H-SOEC) causes the significant anode overpotential because the effective reaction area of oxygen evolution reaction (OER) is limited to TPB due to a mismatch of major ion carriers between the anode and the electrolyte. To increase the effective reaction area, the properties required for the electrode are high reactivity to O atoms in water molecules and a diffusion path for protons generated by OER.

High-valence state transition metal cations incorporated into metal oxides are known to act as a catalytic active site for OER and oxygen reduction reaction (ORR) in neutral or alkaline solutions owing to their unique electronic structures [1-7]. The energy levels between the occupied metal *d* orbital and the O 2*p* orbital tend to get closer with increasing metal valence states, causing strong hybridization, and thus ligand-to-metal charge transfer states, such as $d^{n+1}L^1$ and $d^{n+2}L^2$, are intermixed with the typical ionic configuration d^nL^0 in high-valence-state metal oxides [8]. Here, *L* represents the ligand hole (the oxygen hole) and the superscript number indicates the electron or hole numbers on the metal *d* and oxygen 2*p* orbitals, respectively. In fact, the SOFC cathodes including high valence state Co^{3+} or Ni^{3+} cations involve intermixing of ligand hole states even at elevated temperatures, and such states are recognized to play a crucial role in the performance of the ORR cathode [9,10]. Hence, it is highly motivated to explore OER anode materials based on high-valence-state transition metal oxides for H-SOECs. Unfortunately, many such transition metal oxides are in metastable phases under an ambient atmosphere, as highlighted by their high redox potentials, which cause difficulty in using them directly in H-SOECs without reductive decomposition at elevated temperatures. $Ba_3Mn_2O_8$

($Ba_3(MnO_4)_2$) is a high-valence-state Mn(V) oxide that is known to be thermodynamically stable up to 1000°C in air, regardless of its unusual highly oxidized state [11].

In the crystal structure of $Ba_3(MnO_4)_2$, tetrahedral MnO_4^{3-} oxoanions coordinate to Ba^{2+} cations by bidentate or corner-sharing ways, and this structural feature is similar to that of the scheelite-type $LnTaO_4$ (Ln = La, Nd, Gd, Er) proton conductors [12]. Hence $Ba_3(MnO_4)_2$ is also expected to show partial proton conductivity and thus enlarge reaction area at the anode, as mentioned in chapter 1.

In this chapter, high-valent transition metal oxide $Ba_3(MnO_4)_2$ was demonstrated to be an anode effective for H-SOEC. H-SOECs using a $Ba_3(MnO_4)_2$ base anode could achieve lower anode polarization resistance compared to a cell with the well-known $Sm_{0.5}Sr_{0.5}CoO_3$ anode at 700°C. $Ba_3(MnO_4)_2$ has very large negative hydration enthalpy and thus facilitates the chemisorption of water molecules onto the surface. Therefore, $Ba_3(MnO_4)_2$ anode can lower the anode reaction resistances even at 700°C, because it makes the oxygen evolution reaction occur directly over the electrode surface, instead of being limited within the gas–anode–electrolyte triple phase boundary.

3.2. Experimental

3.2.1. Preparation and characterization

Barium manganate(V), $Ba_3(MnO_4)_2$, was prepared by a conventional solid-state reaction. The powders of $BaCO_3$ and $MnCO_3$ were mixed in an appropriate molar ratio and ground in a mortar for 1 h. The mixtures were then pelletized into a disc with a cold isostatic press (CIP) and calcined at 800°C for 6 h under an ambient atmosphere. After pulverizing in the mortar, the powders were pelletized again by the CIP and finally annealed at 950°C for 48 h in dry air (Ar/O_2 = 4/1). The resulting discs (9.3 mm ϕ, 1 mm *d*) were surface-scrubbed with alumina paste. The phase purity was confirmed by X-ray diffraction (Rigaku Ultima-IV) with Cu Kα radiation, and the chemical composition was examined by inductively coupled plasma optical emission analysis (ICP: PerkinElmer ICP-OES222) with the sample being dissolved in 0.1 M H_2SO_4 solution. Lattice constants *a* and *c* were calculated by using the following Equation (3-1).

$$1/4d_{hkl}^2 = (h^2 + k^2 + hk)/3a^2 + l^2/4c^2 \quad (3\text{-}1)$$

Here, d_{hkl} is the d-spacing of each Miller plane. The values of d_{hkl} were determined by the XRD patterns calibrated with the internal Si standard.

The BET surface area was determined by acquiring nitrogen adsorption isotherms at 77 K (Microtrackbel BELSORP Mini-II). The electrical conductivity was measured using sintered $Ba_3(MnO_4)_2$ pellets by 4-probe DC measurements. The cylindrical pellets (5 mm ϕ × 15 mm L) were prepared by the same sintering process as mentioned above, and four Pt wires (0.05 mm ϕ) were wound on the rim of the pellets.

Thermogravimetric (TG) analysis was performed using a STA2500 thermogravimetric analyzer (Netzsch). For the measurements, specimens were once kept at 900°C in dry air for 6h and then cooled from 900°C to 200°C at a rate of 4°C min^{-1} under a flow of dry and wet air at 50 cm^3 min^{-1}. Dry air was prepared by mixing pure Ar and O_2 in Ar/O_2 = 4/1 (v/v). Wet air was prepared by bubbling them through a water bath at 20°C at a flow rate of 50 cm^3 min^{-1}; the resultant gases had a water partial pressure (p_{H2O}) of 0.023p_0 (p_0 = 101.3 kPa).

3.2.2. EXAFS

Operando XAFS for Mn *K*-edge was obtained on the BL01B1 station of SPring-8, Japan Synchrotron Radiation Research Institute (JASRI). The sample placed in the temperature-controllable cell was heated and/or cooled between room temperature and 700°C at a heating rate of 10°C min^{-1} in air (flow rate: 50 cm^3 min^{-1}). A Si(111) double-crystal monochromator was used. The incident and transmitted X-rays were monitored in ionization chambers filled with N_2 and 85% N_2 + 15% Ar. Quick EXAFS in the continuous scanning mode was recorded from 5674 to 7506 eV (5 min $scan^{-1}$). $BaMnO_4$ (Aldrich) and MnO_2 (Kanto) were used as reference samples. The specimens were mixed with boron nitride powder to achieve appropriate absorbance at the edge energy. The XAFS data were processed using the IFEFFIT software package (Athena and Artemis).

3.2.3. Steam electrolysis

Densely sintered pellets of $BaZr_{0.4}Ce_{0.4}Y_{0.2}O_{3-\delta}$ (BZCY442) were fabricated by a solid-state reactive sintering method assisted by zinc nitrate sintering additives. The precursor powder of BZCY442 was prepared by mixing stoichiometric amounts of starting materials: $BaCO_3$ (High Purity Chemicals; 99.95%), CeO_2 (High Purity Chemicals; 99.99%), ZrO_2 (High Purity Chemicals; 98%), and Y_2O_3 (High Purity Chemicals; 99.99%) along with $Zn(NO_3)_2\ 6H_2O$ additives (Wako Chemicals; 99.9%) as a sintering aid. The amount of the added additives was adjusted for a Zn/Ba molar ratio of 0.02. The powders were dispersed in isopropanol, ball-milled for 24 h, and vacuum-dried. The obtained precursor powders were uniaxially pressed into green pellets at 20 MPa and subsequently pressed under a hydrostatic pressure of 100 MPa in an isostatic press. The pellets were sintered at 1400°C for several hours in air, to obtain sintered discs with a typical diameter of *ca.* 9–9.2 mm and a thickness of 1.8–2.0 mm. Both sides of the sintered discs were polished with 1000 SiC abrasive sandpaper. The phase purity and crystallinity were verified by X-ray diffraction measurements with a Rigaku diffractometer (Rigaku Rint2000). Scanning electron microscopy (SEM) was carried out using a JEOL JSM-7100F microscope. The chemical compositions of the BCY thin films were examined by energy-dispersive X-ray analysis (EDX) using a JEOL JXA-8530F. The relative density of the sintered discs was measured using a pycnometer.

The current–voltage (*I–V*) relationship and faradaic efficiencies were evaluated in a two-electrode cell: 5%-H_2/Ar, Pt |BZCY442| oxide anode, 20%-H_2O/air. The oxide anode and the Pt cathode were screen-printed on the top and bottom surfaces of the BZCY sintered discs (1.5 mm thickness), respectively, using commercial or prepared pastes of cathode and anode catalysts, and these were subsequently co-fired at 800°C. Pt was purchased from Tanaka Co. Here, three oxide materials were examined as an anode catalyst for steam electrolysis: $Sm_{0.5}Sr_{0.5}CoO_{3-\delta}$ (SSC), $Sn_{0.95}Sb_{0.05}O_{2-\delta}$ (ATO), and $Ba_3(MnO_4)_2$-ATO mixtures. SSC pastes were purchased from NexTech Materials Co., Ltd. ATO pastes were prepared by dispersing ATO powders (Mistubishi Materials Co.) in α-terpineol (Aldrich) with 5 wt% polymer dispersant (SolSphere 05). Pastes of $Ba_3(MnO_4)_2$-ATO were prepared by

dispersing the $Ba_3(MnO_4)_2$/ATO mixture (6/4 weight ratio) in α-terpineol with 5 wt% polymer dispersant. The *I–V* characteristics were measured using a Solartron 1260/1287 system. The electrochemical impedance spectra of the H-SOEC were acquired using a Solartron 1260/1287 system in the frequency range of 10^6 to 0.1 Hz with an AC amplitude of 30 mV. To determine the faradaic efficiency of the electrolysis reaction, electrolysis was carried out under galvanostatic conditions and the hydrogen concentrations in the anode out-gases were monitored by gas chromatography (Micro GC; Variant 2000).

Typically, humidified hydrogen gas ($H_2O/H_2/Ar$ = 3/5/92) was fed to the Pt cathode side at a flow rate of 50 cm^3 min^{-1}, and a 20%-H_2O/air mixed gas ($H_2O/O_2/Ar$ = 20/16/64) was fed to the anode side at a rate of 50 cm^3 min^{-1}. The 20%-H_2O/air mixed gas was prepared by passing air through a water bath maintained at ~60°C and then supplied to the anode chamber through stainless-steel tubes heated to 150°C with a ribbon heater to prevent condensation. Hence, the basic configuration of the H-SOEC is as follows: humidified air ($H_2O/O_2/Ar$ = 20/16/64), SSC |BZCY| Pt, wet hydrogen ($H_2O/H_2/Ar$ = 3/5/92).

3.3. Results

3.3.1. Electrical conductivity of $Ba_3(MnO_4)_2$

$Ba_3(MnO_4)_2$ has the $Ba_3(VO_4)_2$-type structure (hexagonal, $R\bar{3}m$), in which Ba cations have ten- or twelve-fold coordinated environments and Mn cations are in a slightly distorted tetrahedral environment, existing as MnO_4^{3-}. The XRD pattern (Figure 3-1a) and the resultant lattice constants (a = 0.571 nm and c = 2.14 nm) are in agreement with those reported previously [11], confirming that a single phase $Ba_3(MnO_4)_2$ was formed.

Figure 3-1b shows the normalized X-ray absorption near edge structure (XANES) spectrum for Mn *K*-edge of $Ba_3(MnO_4)_2$ together with those of two references ($BaMn^{VI}O_4$ and $BaMn^{IV}O_3$), confirming that $Ba_3(MnO_4)_2$ has a well-adopted pentavalent manganese. $BaMn^{IV}O_3$, $Ba_3(Mn^{V}O_4)_2$ and $BaMn^{VI}O_4$ exhibit main absorption peaks at 6556.1, 6557.7, and 6557.3 eV, respectively, attributed to

the purely dipole-allowed $1s \rightarrow 4p$ transition. Before the main edge peak, $Ba_3(Mn^{V}O_4)_2$ gives rise to a sharp pre-edge singlet at 6539.4 eV, due to the quadrupolar $1s \rightarrow 3d$ transition arising from the hybridization of the 3*d* levels of Mn in the presence of the surrounding oxygen ligands [13,14]. This strong pre-edge feature is a characteristic of the tetrahedrally coordinated Mn atoms [15], and thus, the tetrahedrally coordinated $BaMnO_4$ shows a strong peak at 6540.2 eV. The absorption edges defined as the middle point of the edge peaks are determined to be 6552.7, 6554.1 and 6554.8 eV for $BaMn^{IV}O_3$, $Ba_3(Mn^{V}O_4)_2$, and $BaMn^{VI}O_4$, respectively. Thus, the edge peak for $Ba_3(MnO_4)_2$ appears between those of the other two. This is in agreement with the general trends of manganese oxides, for which the absorption edge is linearly correlated with the nominal oxidation state [15].

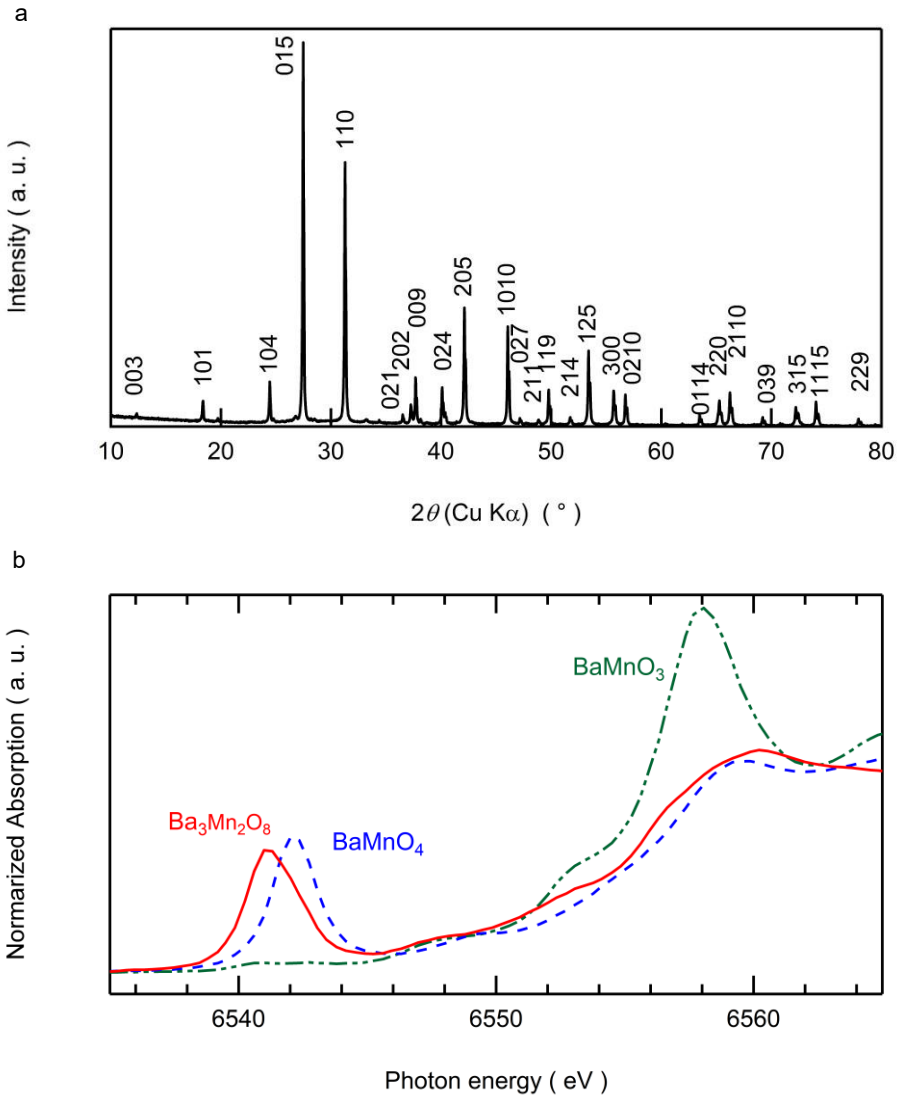

Figure 3-1. (a) XRD patterns of $Ba_3(MnO_4)_2$. (b) Mn *K*-edge XANES of $Ba_3(MnO_4)_2$ and references of $BaMnO_4$ and $BaMnO_3$.

$Ba_3(MnO_4)_2$ exhibits poor semiconductor behavior: its electrical conductivity (σ) at room temperature is very small, at 4.1×10^{-6} S cm^{-1} (300°C) and does not increase above 3.7×10^{-3} S cm^{-1} even at 700°C (Figure 3-2a). σ shows an Arrhenius-type linear dependence on temperature (T) in the range below 520°C; however, the plots clearly deviate upward for T higher than 550°C and the plots become again Arrhenius-type for T above 650°C, which indicates the existence of second or higher order electronic transition in the temperature range of 550 to 650°C. The slopes clarify that the activation energy (E_a) of σ changes in the regions below 500°C and above 670°C, with the values being 72 and 48 kJ mol^{-1}, respectively. To verify the contribution of ionic conductivity, electromotive force (EMF) measurements were conducted by constructing oxygen concentration cells (2%-O_2/Ar, Pt |$Ba_3(MnO_4)_2$| Pt, 100%-O_2) and water concentration cells (0.5%-H_2O/air, Pt |$Ba_3(MnO_4)_2$| Pt, 20%-H_2O/air) at 600 and 700°C. Both cells do not yield significant EMF at either temperature, proving that the electron charge carriers (or hole) are dominant and the proton and oxide ion transfer numbers are negligible over all temperature ranges, and thus, the jump in σ at ~650°C can be attributed to the change in the electron conduction mechanism.

High-temperature XRD reveals that the structural deformation takes place together with the conductivity jump at ~650°C. $Ba_3(MnO_4)_2$ retains the original crystalline phase even at 800°C. The (300) XRD peak essentially shifts to the lower 2θ side with increasing temperature (Figure 3-2b), and thus the lattice constants increase continuously with heating (Figure 3-2c), which is attributed to the thermal expansion of unit cells along the a-axis. On the other hand, the (205) peak shifts to a lower 2θ side with temperature at $T < 690$°C but it is fixed at $T > 700$°C (Figure 3-2b), resulting in the shrinking of the unit cell along the c-axis with temperature at $T > 700$°C (Figure 3-2c). Similarly, the unit cell volume (V) increases with temperature at $T < 690$°C but tends to decrease at $T > 700$°C (Figure 3-2c), confirming that the conductivity jump takes place with thermal shrinkage of V.

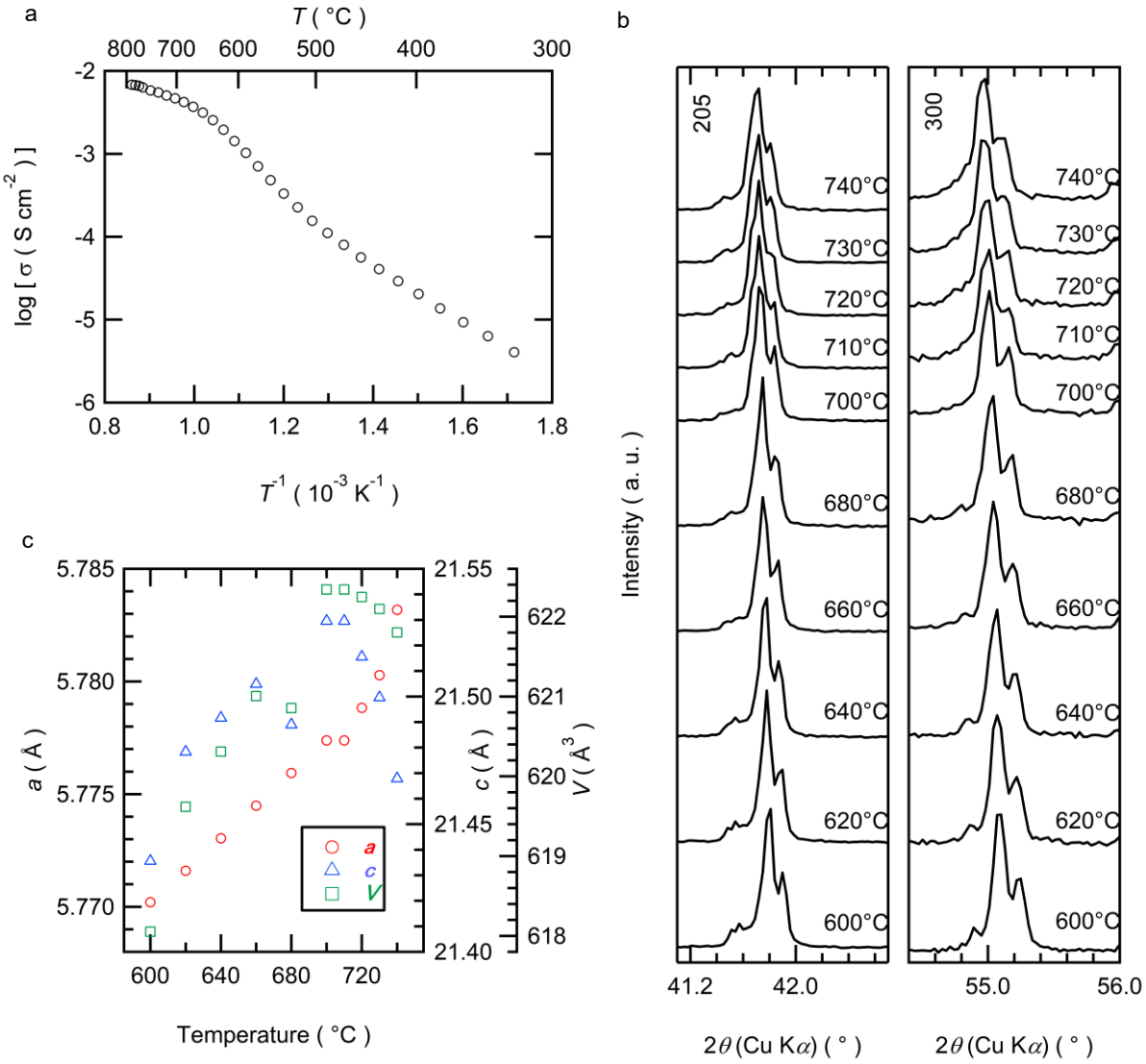

Figure 3-2. (a) Electrical conductivity of $Ba_3(MnO_4)_2$ in air. (b) High-temperature XRD of $Ba_3(MnO_4)_2$, showing shifts of (202) and (300) peaks with temperature. (c) Variation of lattice constants *a* and *c* and unit cell volumes *V*.

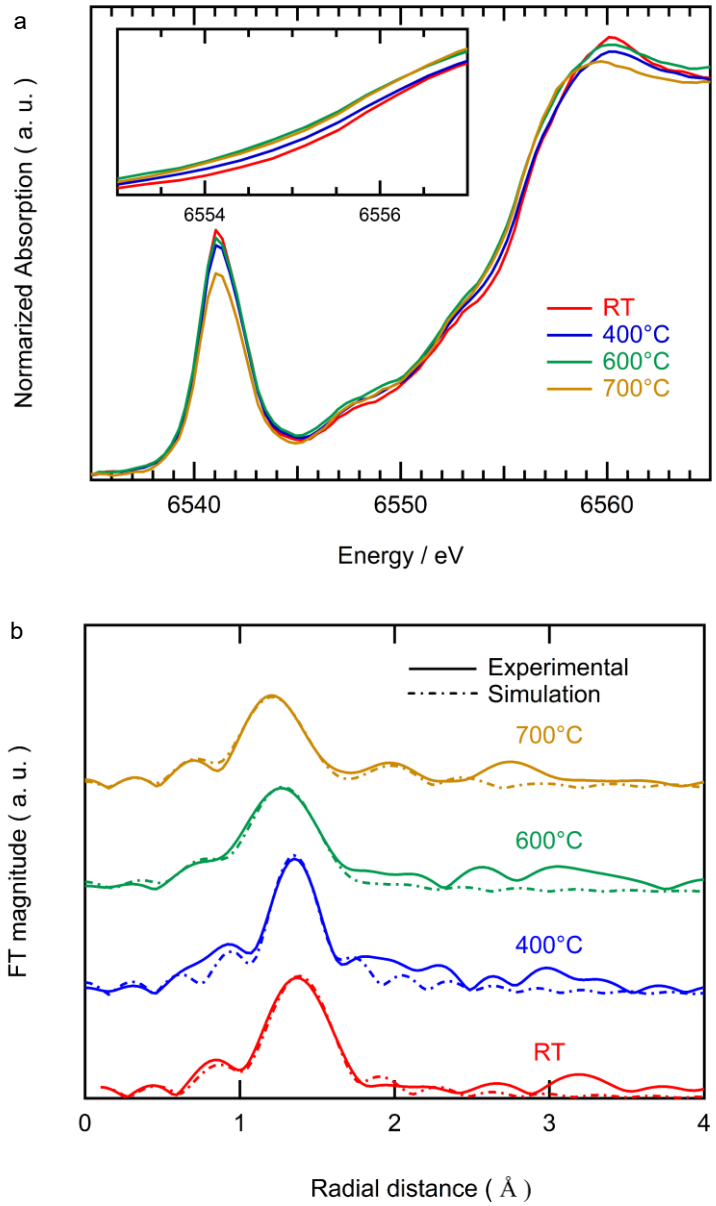

Figure 3-3. Mn *K*-edge EXAFS of $Ba_3(MnO_4)_2$ at various temperatures. (a) XANES region and (b) the corresponding Fourier-transformed radial distribution functions. The inset in (a) shows an expansion of the absorption edge.

3.3.2. XAFS analysis

In order to elucidate the rearrangement of the local structure around Mn atoms at elevated temperatures, *operando* Mn *K*-edge XAFS was conducted for $Ba_3(MnO_4)_2$ under an ambient atmosphere. Figure 3-3a shows the normalized XANES spectrum of $Ba_3(MnO_4)_2$. The spectrum remained unchanged with heating at temperatures below 600°C, while the intensity of the pre-edge and main absorption peaks abruptly decreased with heating between 600 and 700°C, implying the modification of the local coordination environment around Mn atoms due to structural deformation at $T > 600$°C.

Fourier-transform EXAFS analysis was performed to investigate the deformation of the $Mn^{v}O_4^{3-}$ tetrahedron with heating (Table 3-1 and Figure 3-3b). Since these data are shown without phase-shift corrections, the observed peaks might yield shorter atomic distance values than the true atomic distances. Nevertheless, for $Ba_3(MnO_4)_2$, the first coordination shell corresponding to an intense peak at ~1.45 Å can be attributed to the bonding of Mn with four corner O atoms for the $Mn^{v}O_4^{3-}$ tetrahedral oxoanions. In $Ba_3(MnO_4)_2$, the MnO_4 tetrahedra exhibit the C_{3v} symmetry with one short Mn–O2 bond (1.671 Å) and three long Mn–O1 bonds (1.705 Å) [11]. The curve-fitting analysis of the first coordination shell of $Ba_3(MnO_4)_2$ at 25°C leads to a tetrahedral coordination environment with three oxygen atoms at a distance of 1.70 Å and one oxygen at a distance of 1.66 Å (Table 3-1), which are consistent with the aforementioned features of $Mn^{v}O_4^{3-}$ oxoanions [11]. The profiles at 400 and 600°C could be fitted very well by a similar C_{3v} symmetric coordination model, confirming that the local coordination environment around Mn atoms remains unchanged at $T < 600$°C (Table 3-1 and Figure 3-3b).

In contrast, the EXAFS at 700°C does not account for the C_{3v} symmetric tetrahedral coordination environment. The peak position of the first coordination shell clearly shifts to the shorter side with heating between 600 and 700°C (Figure 3-3b), indicating a decrease in the average Mn–O bond length of the $Mn^{v}O_4^{3-}$ tetrahedron. The best fitting for the first Mn–O shell is obtained by a T_d symmetric

tetrahedral coordination environment with four oxygen atoms at an equidistance of 1.69 Å, and this value lies between the lengths of the short Mn–O2 and long Mn–O1 at room temperature (Table 3-1 and Figure 3-3b). Combined EXAFS and XRD studies provide a clear physical model for the structural deformation with an abrupt change in conductivity at ~650°C (see Figure 3-4). In $Ba_3(MnO_4)_2$, an O^{2-} anion tightly bonded to a Mn^{5+} cation (O2) is also coordinated by a Ba^{2+} cation, and thus, the Mn, O, and Ba atoms are aligned along the *c*-axis. In this part, the O atoms bind more tightly to Mn than to Ba neighbors at room temperature, owing to the shorter Mn–O2 bond, which leads to the maintenance of the distance between Ba and O neighbors in the phase before the conductivity jump. However, the Ba cations tend to attract the O neighbors more tightly in the phase at $T > 650$°C than in the phase at $T < 600$°C, and therefore, the lattice constant *c* contracts at ~650°C.

Table 3-1. EXAFS fitting parameters for the first coordination shell

T /°C	r / Å	C.N.	δ / Å
r.t.	1.702 (Mn–O1 × 3)	2.99	−0.003
	1.664 (Mn–O2 × 1)	0.97	−0.007
400	1.700 (Mn–O1 × 3)	2.84	−0.005
	1.681 (Mn–O2 × 1)	0.99	0.010
600	1.699 (Mn–O1 × 3)	3.07	−0.006
	1.682 (Mn–O2 × 1)	1.06	0.010
700	1.690 (Mn–O × 4)	3.77	−0.015

Since $Ba_3(MnO_4)_2$ is a spin-dimer antiferromagnet with a high-spin configuration of $S = 1$ [16], the conductivity gap is close to the sum of the band gap (E_g) and exchange energy for antiferromagnetic

ordering (*J*). The antiferromagnetic/paramagnetic transition above the Néel temperature is typical of the second order phase transition [17], which is in agreement with the feature of the conductivity jump of $Ba_3(MnO_4)_2$. The conductivity gap of the paramagnetic phase tends to be smaller than that of the antiferromagnetic phase due to the decline of the exchange term, and thus, the conductivity jump is attributable to the antiferromagnetic/ferromagnetic transition. The shape change of MnO_4 units must be correlated to the phase transition.

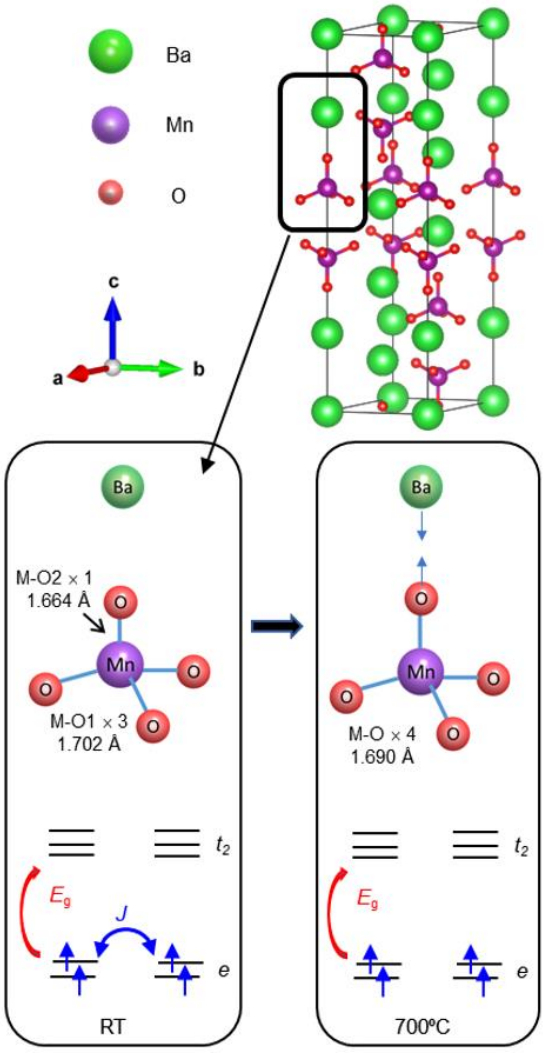

Figure 3-4. Structural deformation and decreasing conductivity gap by the antiferromagnetic/paramagnetic transitions.

3.3.3. Proton uptake of $Ba_3(MnO_4)_2$

Figure 3-5a show the thermogravimetric (TG) curves of the $Ba_3(MnO_4)_2$ powder, measured by cooling in dry and wet air after heating at 900°C in dry air. The wight changes are very small in dry air, whereas $Ba_3(MnO_4)_2$ exhibits a significant weight gain of ~0.3% at $T < 700$°C in wet air. The results confirm that $Ba_3(MnO_4)_2$ undergo hydration via association of water and oxygen vacancy, as described by Equation (3-2):

$$H_2O + V_O^{\bullet\bullet} + O_O^{\times} \rightarrow 2\ OH_O^{\bullet} \qquad (3\text{-}2)$$

Here $V_O^{\bullet\bullet}$ is the oxygen vacancy, $O_O^{\times}$ represents the lattice oxygen, and $OH_O^{\bullet}$ is the proton defect. Assuming that this weight increase is caused only by hydration (Equation 3-2), the proton uptake per

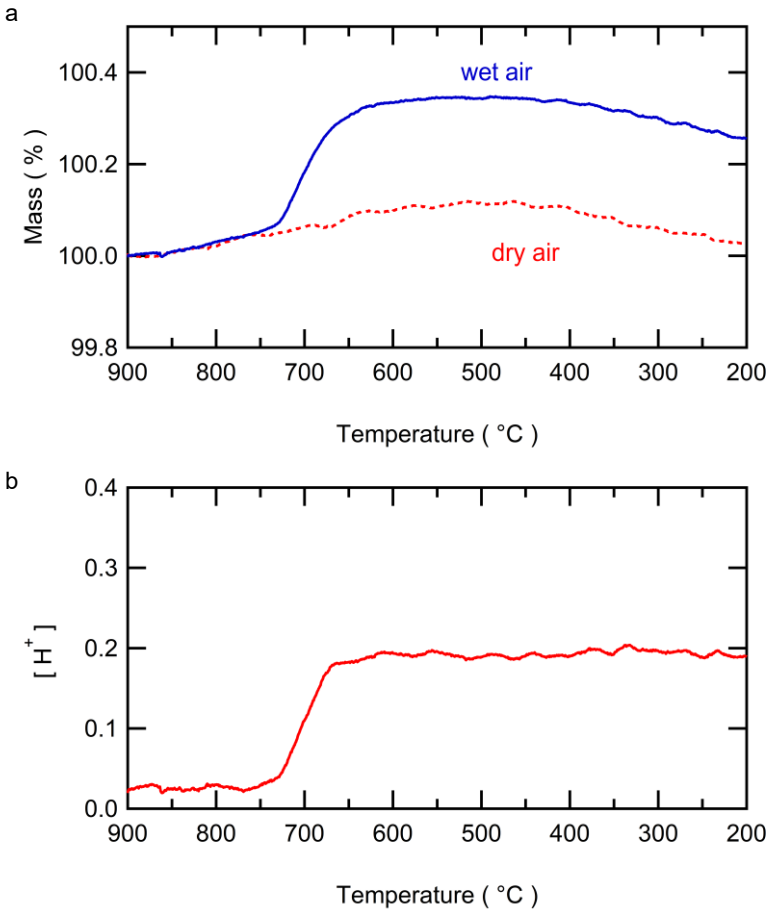

Figure 3-5. (a) TG curves of $Ba_3(MnO_4)_2$ tested from 900 to 200°C in dry and wet air ($p_{H2O} = 0.023\ p_0$) and (b) proton concentration [H^+] of $Ba_3(MnO_4)_2$ calculated from TG in 200-900°C

$Ba_3(MnO_4)_2$ unit cell is calculated shown in Figure 3-5b. $Ba_3(MnO_4)_2$ gains protons of about 0.2 in molar fraction in the temperature below 670°C.

The reaction free energy $\Delta G^0(T)$ is negative due to Equation (3-3) if the dehydration occurs spontaneously at a certain temperature.

$$\Delta G^0(T) = \Delta H^0 - T\Delta S^0 \leq 0 \quad (3\text{-}3)$$

Here ΔS^0 and ΔH^0 are the hydration entropy and enthalpy at the standard pressure. $\Delta G(T, p_{H2O})$ at p_{H2O} can be translated by Equation (3-4) because the equilibrium of reaction is related to the p_{H2O}.

$$\Delta G(T, p_{H2O}) = \Delta G^0(T) - RT \ln(p_{H2O}/p_0) \quad (3\text{-}4)$$

Under equilibrium state ($\Delta G(T, p_{H2O}) = 0$), Equations (3-3), (3-4) can be rewritten as Equation (3-5).

$$p_{H2O}/p_0 = exp(\Delta H^0/RT)\ exp(-\Delta S^0/R) \quad (3\text{-}5)$$

This provides the equilibrium p_{H2O} at a given temperature. Under a fixed p_{H2O}, Equation (3-5) indicates that the dehydration of metal oxides readily occurs by heating in the region above the threshold temperature (T_{de}), which satisfies the following equation:

$$\Delta H^0/RT_{de} = \ln(p_{H2O}/p_0) + (\Delta S^0/R) \quad (3\text{-}6)$$

T_{de} corresponds to the onset temperature of the dehydration as observed in the TG curves (Figure3-5a), which is equal to 943K at p_{H2O} = 0.023 atm for $Ba_3(MnO_4)_2$. Here, ΔS^0 is the mixing entropy for the association between oxygen vacancies and water gas and, thus, can be approximated by the partial mole entropy of water (S^m_{H2O}) and that is assumed to be 120 J K^{-1} reported for the hydration equilibria of $La_{0.99}Ca_{0.01}TaO_4$ reported by the group of T. Norby [18]. ΔH^0 is roughly estimated to be −140 kJ mol^{-1} at hydrated temperature. $Ba_3(MnO_4)_2$ exhibits negative larger ΔH^0 than those of $PrBa_{0.5}Sr_{0.5}Co_{1.5}Fe_{0.5}O_{5+\delta}$ (PBSCF), $BaGd_{0.8}La_{0.2}Co_2O_{6-\delta}$ (BGLC), $BaCo_{0.4}Fe_{0.4}Zr_{0.1}Y_{0.1}O_{3-\delta}$ (BCFZY) and $Ba_{0.95}La_{0.05}Fe_{0.8}Zn_{0.2}O_{3-\delta}$ (BLFZ), known as $H^+/O^{2-}/e^-$ triple conductors [19-22], thereby $Ba_3(MnO_4)_2$ retains much more proton defects than other triple conductors even at 670°C (Table 3-2). $[OH_O^{\bullet}]$ of $Ba_3(MnO_4)_2$ at 670°C is about 0.2, which is 10 times larger than that of the well-known

triple conductor PBSCF at 600°C. ΔH^0 of $Ba_3(MnO_4)_2$ is equivalent as the high proton conductor $BaCe_{0.9}Y_{0.1}O_{3-\delta}$ [23] (Table 3-2). These results suggests that $Ba_3(MnO_4)_2$ is a promising anode material for H-SOFC with significantly high proton conductivity.

Table 3-2. Hydration properties of $Ba_3(MnO_4)_2$, other triple Conductors and $BaCe_{0.9}Y_{0.1}O_{3-\delta}$

Material		$[OH_O^{\bullet}]$	p_{H2O} / p_0	ΔH^0 (kJ mol^{-1})	ref
$Ba_3(MnO_4)_2$	B3M2	0.2 (670°C)	0.023	-140	This work
$PrBa_{0.5}Sr_{0.5}Co_{1.5}Fe_{0.5}O_{5+\delta}$	PBSCF	0.036 (200°C)	0.02	-10 (200°C)	[19]
$PrBa_{0.5}Sr_{0.5}Co_{1.5}Fe_{0.5}O_{5+\delta}$	PBSCF	0.018 (600°C)	0.02	-70 (600°C)	[19]
$BaGd_{0.8}La_{0.2}Co_2O_{5+\delta}$	BGLC	0.03 (400°C)	0.02	-50	[20]
$BaCo_{0.4}Fe_{0.4}Zr_{0.1}Y_{0.1}O_{3-\delta}$	BCFZY	0.005 (500°C)	0.016	-33	[21]
$Ba_{0.95}La_{0.05}Fe_{0.8}Zn_{0.2}O_{3-\delta}$	BLFZ2	0.1 (250°C)	0.016	-86	[22]
$Ba_{0.95}La_{0.05}Fe_{0.9}Zn_{0.1}O_{3-\delta}$	BLFZ1	0.079 (250°C)	0.016	-53	[22]
$BaCe_{0.9}Y_{0.1}O_{3-\delta}$	BCY	0.05 (400°C)	0.0063	-138	[23]

3.3.4. Steam electrolysis measurements

Steam electrolysis was conducted with a cell of oxide-anode | BZCY442 (1.5 mm) | Pt-cathode fed with humidified air (20% H_2O) at the anode side and humidified 1%-H_2/Ar gas (3% H_2O) at the cathode side. Figure 3-6 shows surface SEM images of the SSC, $Ba_3(MnO_4)_2$, and $Ba_3(MnO_4)_2$-ATO mixture anode layers formed on BZCY sintered discs, confirming that all are porous and comprise agglomerates of sub-micrometer- or micrometer-sized particles. The sizes of SSC and ATO particles are ~200 nm and less than 50 nm, respectively, and thus have relatively large BET surface areas of 39 and 115 $m^2\ g^{-1}$, respectively. In contrast, $Ba_3(MnO_4)_2$ powders are made of coarse grains with 0.5–3 μm diameters and thus have a relatively small BET surface area of 9.5 $m^2\ g^{-1}$, which indicates that $Ba_3(MnO_4)_2$-ATO anodes are made of agglomerates of large $Ba_3(MnO_4)_2$ grains deposited with small ATO particles.

The *I–V* characteristics of the H-SOEC with SSC and $Ba_3(MnO_4)_2$-ATO anodes at 700 and 600°C are shown in Figure 3-7a. Both cells have OCVs of ~0.95 and 1.02 V at 700 and 600°C, respectively, which are in agreement with the values reported for the $BaZr_xCe_{0.8-x}Y_{0.2}O_{3-\delta}$ cells fed with diluted hydrogen and steam [24-28]. In contrast, ATO showed deteriorated performance, with an OCV of less than 0.6 V and much lower current than those of the other two at any temperature (Figure 3-7a). These results indicate that ATO is not electrocatalytically active, and it therefore acts only as an electroconductive filler. The electrolysis current of $Ba_3(MnO_4)_2$-ATO is remarkably larger than that of SSC at 700°C, with the currents at 2.0 V bias for $Ba_3(MnO_4)_2$-ATO and SSC cells being 125 and 80 mA cm^{-2}, respectively. However, the current of the former falls to a similar level to that of the latter with a decrease in the temperature to 600°C, with the currents at 2.0 V bias for SSC and $Ba_3(MnO_4)_2$-ATO cells equaling 40 mA cm^{-2}.

The faradaic efficiency of $Ba_3(MnO_4)_2$-ATO was examined by monitoring the amount of the hydrogen gas evolved on the cathode side under galvanostatic conditions, confirming that the $Ba_3(MnO_4)_2$ cell facilitates steam electrolysis as highly efficiently as the SSC cell [29]. At 700°C, the efficiency is more than 80% in the current range of less than 50 mA cm^{-2}, whereas it drops to 70% under high current conditions (Figure 3-7b). Such a characteristic has been attributed to the increase in the partial hole conductivity of the $BaZr_xCe_{0.8-x}Y_{0.2}O_{3-\delta}$ electrolyte at elevated temperatures [30-32]. Hence, the cell yields a higher faradaic efficiency with decreasing temperature, due to a decrease in the hole transfer numbers, thus achieving ~75% efficiency at 600°C (Figure 3-7b). The SSC cell exhibits similar efficiency to that of the $Ba_3(MnO_4)_2$ cell [29].

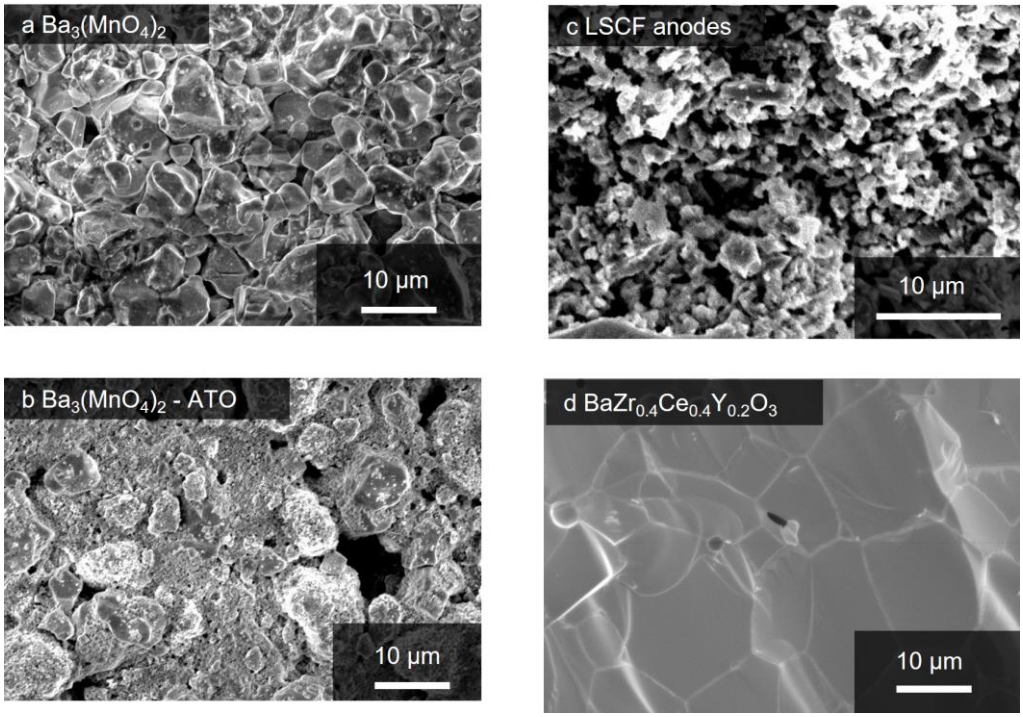

Figure 3-6. Surface SEM images of (a) $Ba_3(MnO_4)_2$, (b) $Ba_3(MnO_4)_2$-ATO and (c) LSCF anodes and (d) $BaZr_{0.4}Ce_{0.4}Y_{0.2}O_3$ electrolyte.

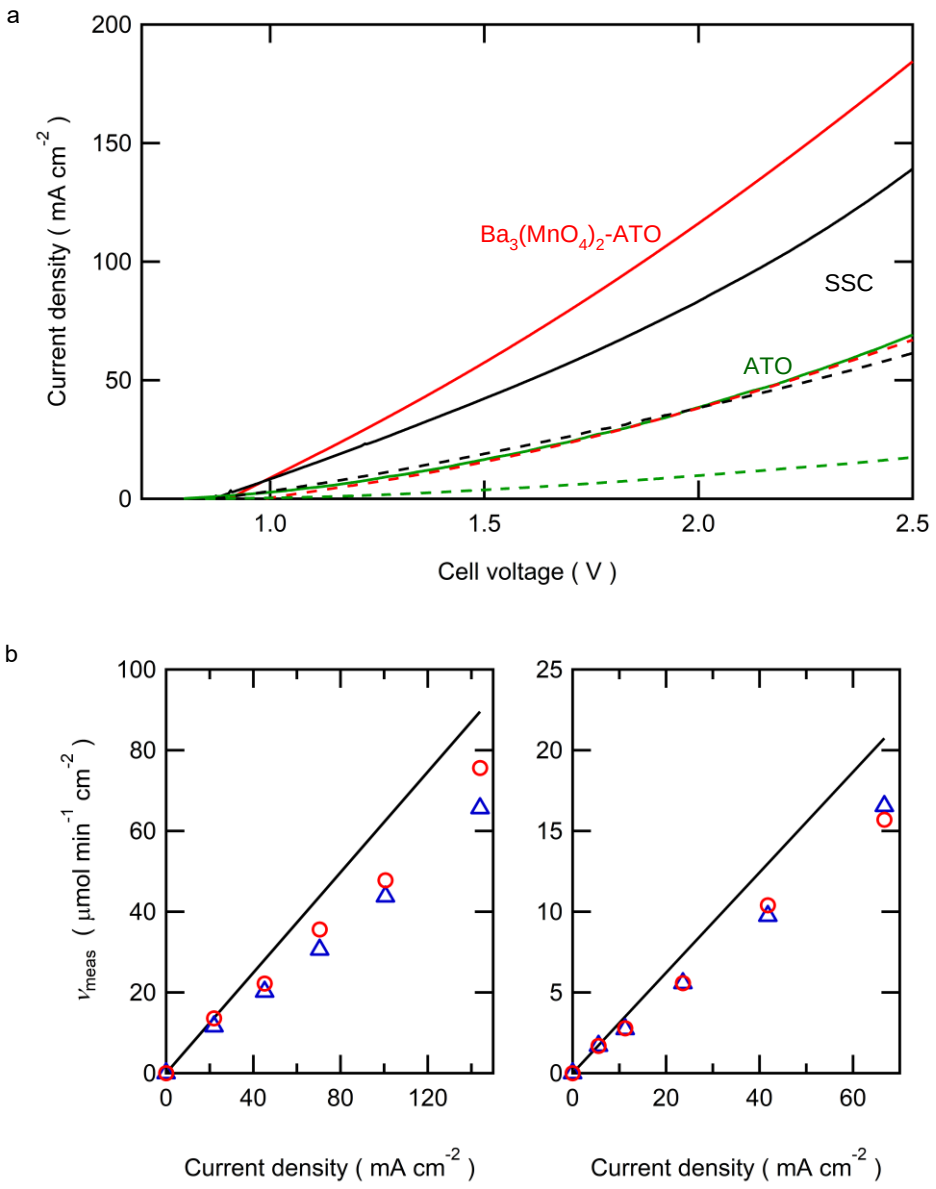

Figure 3-7. (a) IV-characteristics of SOEC with $Ba_3(MnO_4)_2$-ATO, ATO, and SSC anodes. Solid and dashed lines indicate the currents at 700 and 600°C. (b) The hydrogen evolution rate (v_{meas}) of H-SOEC with Ba3$(MnO_4)_2$-ATO (○) and SSC (△) anodes at 700 and 600°C, respectively.

To deconvolute the anodic polarization resistances, the impedance responses were recorded at 700°C under various DC conditions (Figure 3-8). In general, in the impedance spectra of the solid electrochemical cells, the high-frequency x-intercept represents Ohmic loss, i.e., the electrolyte resistances and the following arcs are associated with the interfacial polarization. The SSC cells yield two distinct arcs at 700°C: a large S_h arc in the high-frequency region at approximately 10^5–10^2 Hz, and a small S_l arc in the low-frequency region at approximately 10^2–10^{-1} Hz. These spectral features of the SSC cells at 700°C have been replicated well by employing the equivalent circuit shown in the inset of Figure 3-9a [29], wherein R_b corresponds to the electrolyte resistance and the parallelly connected elements (R_hQ_h) and (R_lQ_l) represent S_h and S_l impedance arcs, respectively. Here, R_i is the resistance element and Q_i is the constant phase element representing the time-dependent capacitance [33], and the parallelly connected R_i and Q_i are related to the capacitance C_i according to Equation (3-7) [33].

$$C_i = (R_i \cdot Q_i)^{1/ni} R_i^{-1} \tag{3-7}$$

The spectra obtained at various potentials can be fitted with the equivalent circuit $R_b(Q_hR_h)(Q_lR_l)$, and R_i, Q_i, and n_i can be determined with errors within a few tens of percentage points.

The $Ba_3(MnO_4)_2$-ATO cells also provide two impedance arcs at 700°C, which appear in the same frequency regions as S_h (10^4–10^2 Hz) and S_l (10^2–10^{-1} Hz). The diameters of both the arcs systematically decrease with increasing DC current (Figure 3-8a), revealing that these are related to the anode reaction kinetics and not to the diffusion-limited concentration overpotentials. The diameters of the mixed S_h and S_l arcs of the $Ba_3(MnO_4)_2$-ATO anode are nearly half of those of the SSC anode, confirming that the polarization resistances of the former are much lower than those of the latter. The spectra of $Ba_3(MnO_4)_2$-ATO can also be fitted very well with the same equivalent circuit as that used for the SSC cell (Figure 3-9a). The R_b is approximately 7–8 Ω cm^2 at all potentials, which is much larger than the polarization resistances R_h and R_l, indicating that the electrolyte resistance dominates over all voltage losses, even at 700°C, owing to the significant thickness (1.2 mm) of the bulk

electrolytes. The resultant R_h and R_l for SSC and $Ba_3(MnO_4)_2$-ATO cells are plotted as a function of cell voltage in Figure 3-9b. Although both have similar R_l values, R_h is significantly reduced upon using the $Ba_3(MnO_4)_2$-ATO anode.

The cells exhibited elongated polarization arcs at 600°C (Figure 3-8b) because additional polarization arcs appeared in the mid-frequency region at $\sim 10^2$ Hz with decreasing temperature. Unfortunately, it is difficult to conduct equivalent circuit fitting to such an elongated spectrum on the basis of a simple parallelly connected (Q_iR_i) component. The diameters of the mixed impedance arcs of $Ba_3(MnO_4)_2$-ATO and SSC are similar, implying that the polarization resistances of the former are similar to those of the latter at 600°C. This is consistent with the results of *I–V* characteristics (Figure 3-7a), proving that the electrocatalytic activity of $Ba_3(MnO_4)_2$ is enhanced by the conductivity jump. Hereafter, the properties at 700°C are mainly considered.

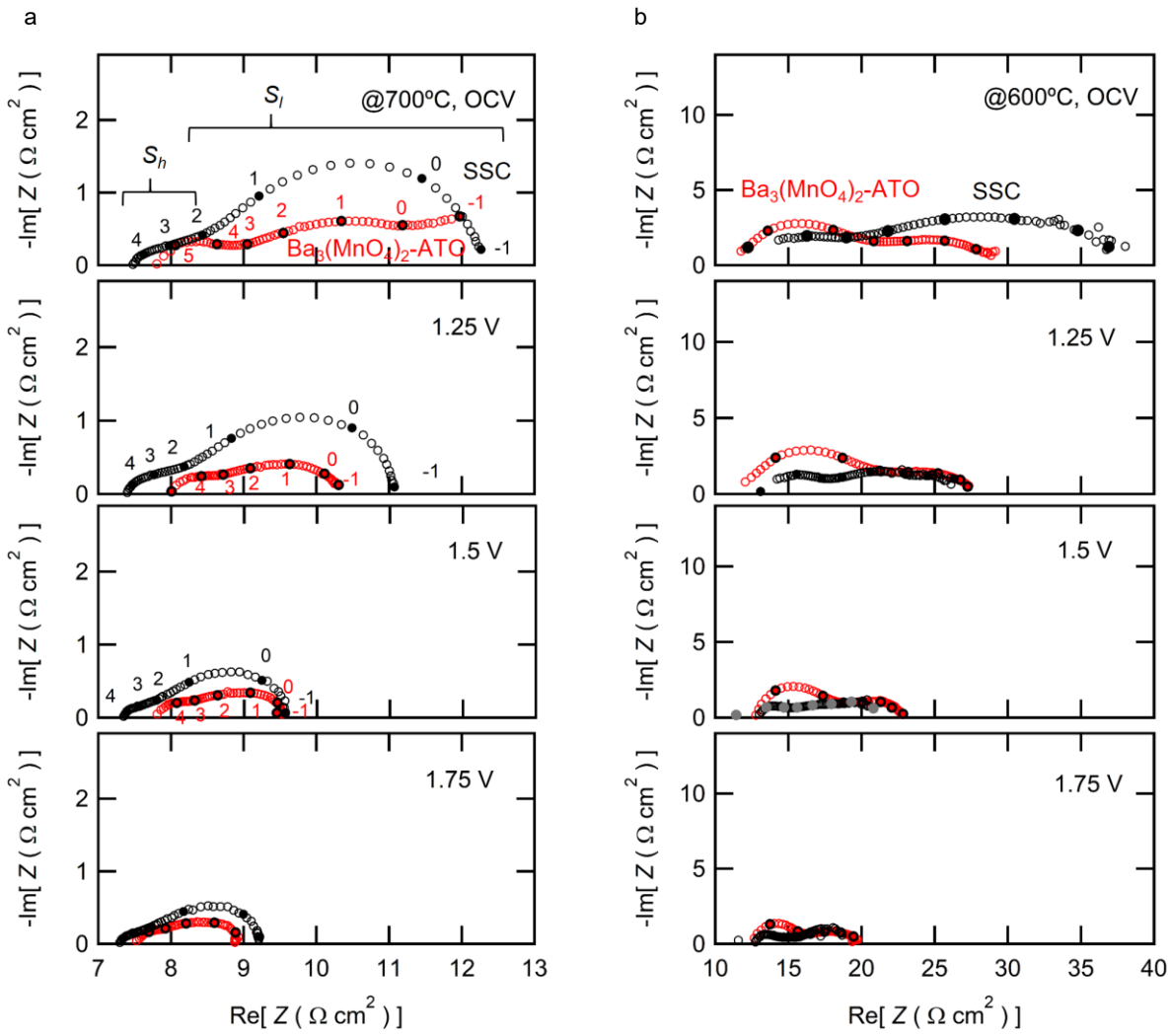

Figure 3-8. Impedance responses of SOEC with SSC or $Ba_3(MnO_4)_2$-ATO anodes at (a) 700°C and (b) 600°C under various biases. 20%-H_2O/air was fed to the anode and 3%-H_2O/5%-H_2/Ar was fed to the cathode. In (a), S_h and S_l indicate the impedance arcs in high and low frequency ranges, respectively.

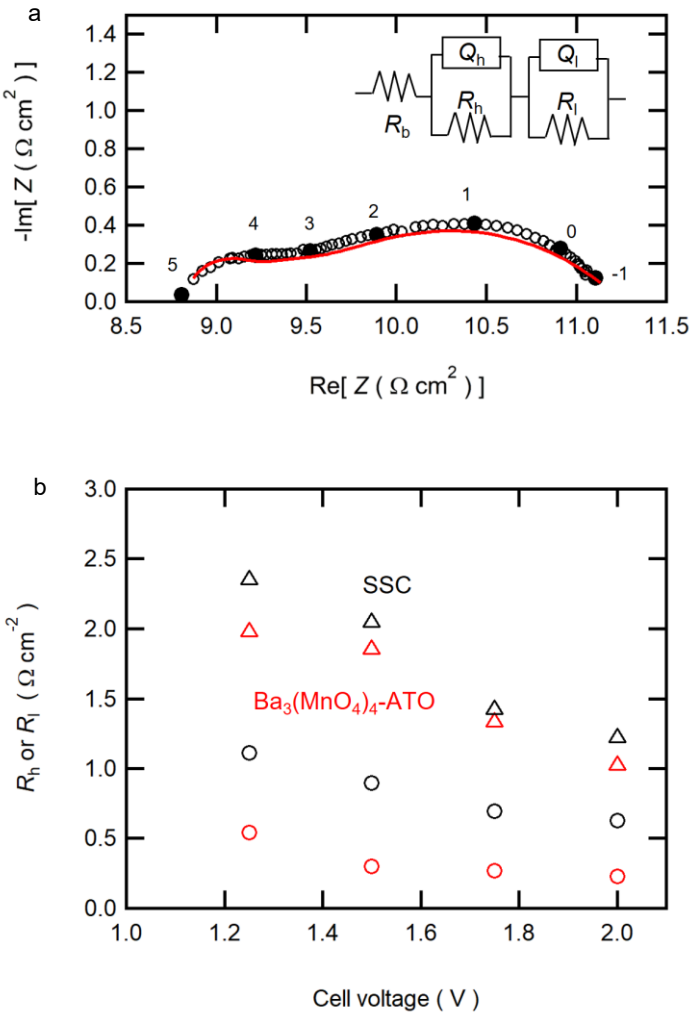

Figure 3-9. (a) Equivalent circuit fitting to the impedance spectra of SOEC with $Ba_3(MnO_4)_2$-ATO anodes at 700°C under 1.2 V cell voltage. Circles represent the measured data and the solid line represents the fit with the model depicted in the inset. (b) R_h (circles) and R_l (triangles) of the impedance spectra of SOEC with SSC (black) or $Ba_3(MnO_4)_2$-ATO (red) anodes under various DC conditions at 700°C, which were determined by equivalent circuit analysis of the spectra displayed in Figure 3-6a.

3.4. Discussion

I demonstrated that $Ba_3(MnO_4)_2$ has a pronounced electrocatalytic performance for anode reactions of H-SOEC at *T* above 600°C with a conductivity jump. Polarization resistances of the $Ba_3(MnO_4)_2$-base anode aided by a conductive filler are sufficiently lower than those of the well-established SSC anode at 700°C, although the values of the former fall at the same level as those of the latter at 600°C before electronic conduction jump.

Recently, two kinds of reaction schemes have been proposed for the OER of H-SOEC [29]: one is triggered by water adsorption on the anode surface (Model-A; Figure 3-10a) [27], while the other is triggered by water adsorption at the gas–anode–electrolyte triple phase boundary (TPB) (Model-B; Figure 3-10b) [34]. In Model-A, the OER process is completed *via* dissociative adsorption of water on the electrode surface (steps 1a, 2a and 3a), multiple charge transfers (steps 4a and 5a), and associative adsorption of oxygen on the electrode surface (steps 6a and 7a), together with the interfacial proton transfer across the TPB (steps 8a and 9a), as shown in Figure 3-10a and Table 3-3 [29]. Here "ad", "TPB", and "elec" indicate species in the electrode surface, the TPB, and the BZCY electrolyte, respectively. In Model-B, the OER process comprises dissociative adsorption of water at the TPB (steps 1b, 2b and 3b), multiple charge transfers with the shift of oxygen species (steps 5b, 6b and 7b), and associative adsorption of oxygen on the electrode surface (step 8b), together with the interfacial proton transfer (step 4b), as shown in Figure 3-10b and Table 3-3 [29].

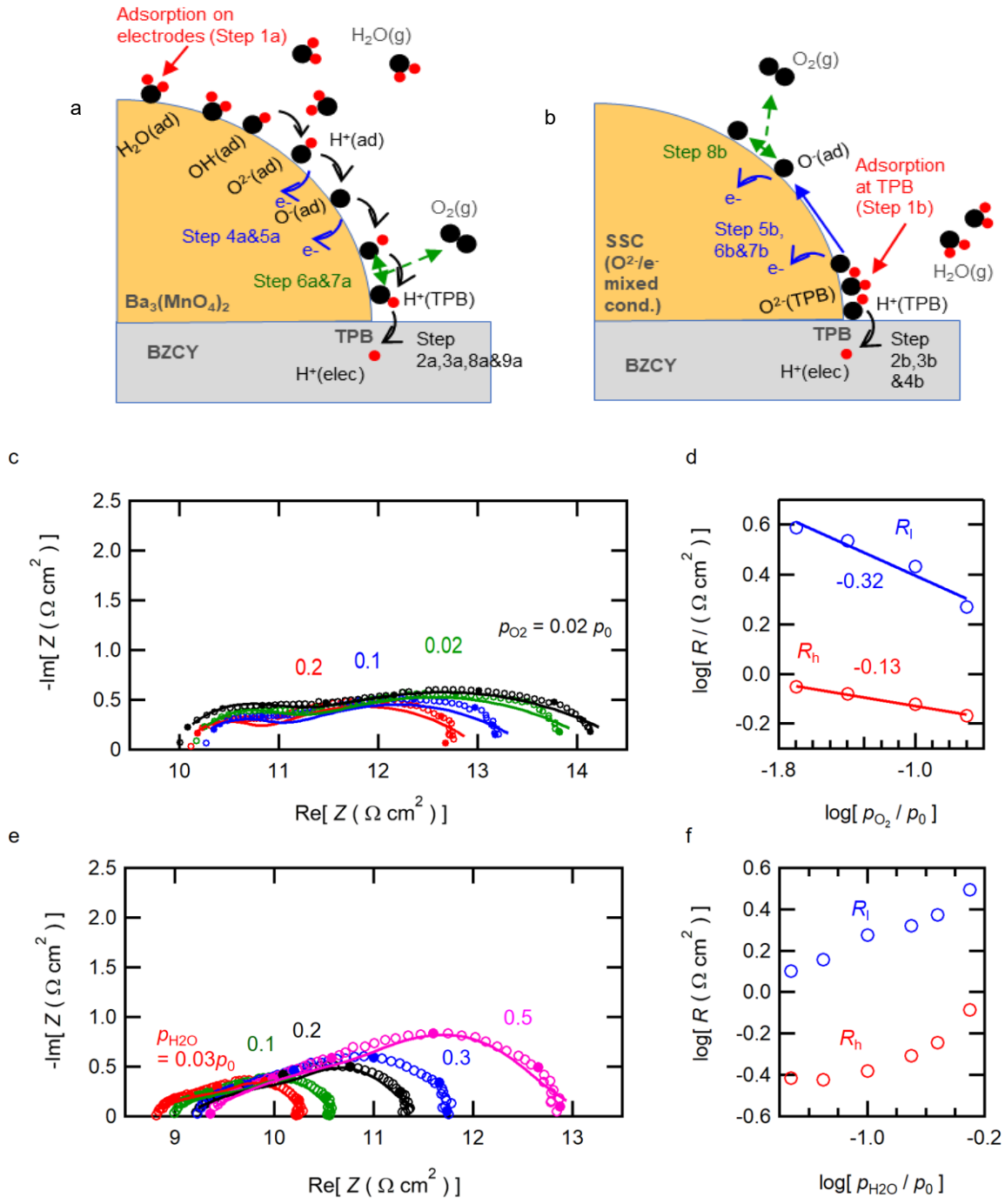

Figure 3-10. Schemes for the anode reactions of H^+-SOEC with the reaction sites existing (a) over the electrode surface and (b) at the gas–anode–electrolyte triple phase boundary. Impedance responses of SOEC with $Ba_3(MnO_4)_2$-ATO anodes, obtained by changing (c) p_{O_2} and (e) p_{H_2O} in the anode side at 700°C. Circles are the observed values and solid lines are the fits obtained by equivalent circuit analysis with the model depicted in Figure 3-9a. Resultant R_h and R_l determined by equivalent circuit analysis of (d) p_{O_2} and (f) p_{H_2O}-variable impedance spectra.

Table 3-3. Elementary anode reaction steps for Models-A and -B (see Figure 3-10a and b) and the related reaction orders in terms of oxygen partial pressures (*m*) and water vapor partial pressures (*n*)

Steps	Reactions	*m*	*n*
Model-A			
Step (1a)	$H_2O(g) \rightarrow H_2O(ad)$	0	1
Step (2a)	$H_2O(ad) \rightarrow OH^-(ad) + H^+(ad)$	0	1
Step (3a)	$OH^-(ad) \rightarrow O_2^-(ad) + H^+(ad)$	0	1/2
Step (4a)	$O^{2-}(ad) + h^+ \rightarrow O^-(ad)$	1/8	0
Step (5a)	$O^-(ad) + h^+ \rightarrow O(ad)$	3/8	0
Step (6a)	$2O(ad) \rightarrow O_2(ad)$	1	0
Step (7a)	$O_2(ad) \rightarrow O_2(g)$	1	0
Step (8a)	$H^+(ad) \rightarrow H^+(TPB)$	0	1/2
Step (9a)	$H^+(TPB) \rightarrow H^+(elec)$	0	1/2
Model-B			
Step (1b)	$H_2O(g) \rightarrow H_2O(TPB)$	0	1
Step (2b)	$H_2O(TPB) \rightarrow OH^-(TPB) + H^+(TPB)$	0	1
Step (3b)	$OH^-(TPB) \rightarrow O^{2-}(TPB) + H^+(TPB)$	0	1/2
Step (4b)	$H^+(TPB) \rightarrow H^+(elec)$	0	1/2
Step (5b)	$O2^-(TPB) + h^+ \rightarrow O^-(TPB)$	0	0
Step (6b)	$O^-(TPB) \rightarrow O^-(ad)$	1/4	0
Step (7b)	$O^-(ad) + h^+ \rightarrow O(ad)$	3/8	0
Step (8b)	$2O(ad) \rightarrow O_2(g)$	1	0

According to the simple kinetic treatment, the rate equations for the elementary steps were converted to a function of p_{O2}^{m} and p_{H2O}^{n} with reaction orders of m and n, as listed in Table 3-3 [29]. If step i with reaction orders of m_i and n_i is the rate-controlling anode reaction of H-SOEC, ideally, the corresponding polarization resistances (R_i) should be proportional to p_{O2}^{-mi} and p_{H2O}^{-ni}. Based on this assumption, the impedance analysis with varying p_{O2} and p_{H2O} at anode sides have been carried out for the SSC cell to determine the reaction orders of R_h and R_l [29]. The anode reactions at the SSC/BZCY interfaces were found to proceed *via* the pathway of Model-B [29]. Moreover, S_h of the SSC cells could be assigned to the first electron transfer at TPB (step 5b) and S_l to the shift of the oxygen chemisorbed from TPB to the anode surface (step 6b) because the measurements provided $R_h \propto p_{O2}^{0}$ and p_{H2O}^{0} and $R_l \propto p_{O2}^{-1/4}$ and p_{H2O}^{0}, which are in agreement with the ideal reaction orders of each step in Model-B (Table 3-3) [29].

To gain insight into the reaction scheme and rate-limiting steps for the $Ba_3(MnO_4)_2$ base anode, impedance responses were acquired in terms of p_{O2} and p_{H2O} in anode gases (Figure 3-10c–f). As for the p_{O2} dependence, S_l arcs are remarkably enlarged with decreasing p_{O2}, with R_l being proportional to $p_{O2}^{-0.32}$ (Figure 3-10c and d) in the p_{O2} range of 0.02 to 1.0p_0 (p_0 = 101.3 kPa) at a fixed temperature. S_h arcs are weakly dependent on p_{O2}, leading to $R_h \propto p_{O2}^{-0.13}$. For p_{H2O} dependence, however, $Ba_3(MnO_4)_2$ yields a negative value of n for both S_h and S_l arcs (Figure 3-10e and f). R_h and R_l significantly increase with p_{H2O} in the range of 0.01 to 0.5p_0, indicating the deterioration of the electrocatalytic performance of $Ba_3(MnO_4)_2$ due to moisture. XRD measurements confirm that the structure of $Ba_3(MnO_4)_2$ and ATO remain unchanged even after steam electrolysis at 2.0 V for 1 h. Furthermore, the impedance arcs of $Ba_3(MnO_4)_2$-ATO can recover their original values with the return of p_{H2O} to 0.1p_0 after exposure to 50%-H_2O/air for 3 h (Figure 3-10b), confirming that $Ba_3(MnO_4)_2$ does not decompose under high p_{H2O} conditions. These features imply that $Ba_3(MnO_4)_2$ suffers H_2O-poisoning under relatively high p_{H2O} conditions because it is favorably

hydrated even at 700°C due to the high hydration enthalpy. Hence the surface coverage by adsorbed H_2O increases and the number of reaction sites is decreased with increasing p_{H2O}.

Nevertheless, the p_{H2O} dependence provides clear evidence for the occurrence of the OER on $Ba_3(MnO_4)_2$ via a different reaction scheme than that of SSC, i.e., via Model-A. m of R_h is ~0.13, which is in agreement with the ideal values (1/8) of step 4a (1st electron (hole) transfer step) in Model-A, while it does not conform to any steps of Model-B (Table 3-3). Similarly, m of R_l results in 0.32, which is consistent with the value (3/8) of the second electron transfer step, i.e., step 5a, but is not close to the values of Model-B. These results prove that the anode reaction processes on the $Ba_3(MnO_4)_2$ base anode mainly occur according to Model-A, although those of the SSC cells are driven by Model-B. Moreover, the results of the reaction order analysis suggest that the electron charge transfer steps would limit the overall reaction rate of the $Ba_3(MnO_4)_2$ anode (Figure 3-10a), probably owing to its poor electrical conductivity. Since σ of $Ba_3(MnO_4)_2$ is several orders of magnitude lower than that of SSC (~500 S cm^{-1} at 700°C) [35] even after the conductivity jump, large overpotentials may take place for driving electron migration in $Ba_3(MnO_4)_2$. In fact, $Ba_3(MnO_4)_2$ cannot achieve pronounced electrocatalytic performance before the conductivity jump at ~600°C.

The aforementioned results unambiguously demonstrate that $Ba_3(MnO_4)_2$ is greatly advantageous for use in H-SOEC in relation to the reaction areas extended by the excellent hydration capability. Since $Ba_3(MnO_4)_2$ allows water absorption by Equation (3-2) and thus may show partial proton conductivity, the effective reaction sites are extended over the entire electrode surface without being confined near the TPB. However, the reaction sites of the SSC anode are limited, since the water adsorption is triggered only at the TPB, owing to the relatively high positive hydration enthalpy [35]. Hence, the $Ba_3(MnO_4)_2$ anode exhibits lower anode polarization resistances than the SSC anode although the former has a smaller TPB area than the latter owing to the relatively large grain size.

As mentioned in the beginning of this chapter, the crystal structure of $Ba_3(MnO_4)_2$ is similar to that of the scheelite-type proton conductor. In scheelite-type $LaNbO_4$, hydration occurs via the association

oxygen-defect NbO_4^{3-} tetrahedra, i.e., $NbO_3(V_O)^-$ and water molecules (Figure 3-11) [36]. The large negative hydration enthalpy of $Ba_3(MnO_4)_2$ could attribute to the large basicity of oxygen-defect MnO_4^{3-} tetrahedra, i.e., $MnO_3(V_O)^-$ oxoanions because Mn that has many unoccupied 3*d* states to accept the additional electrons from water molecules. In conclusion, $Ba_3(MnO_4)_2$ is a promising anode electrocatalyst for H-SOEC, and this finding offers an opportunity to explore other active anode materials based on high-valence-state transition metal oxides.

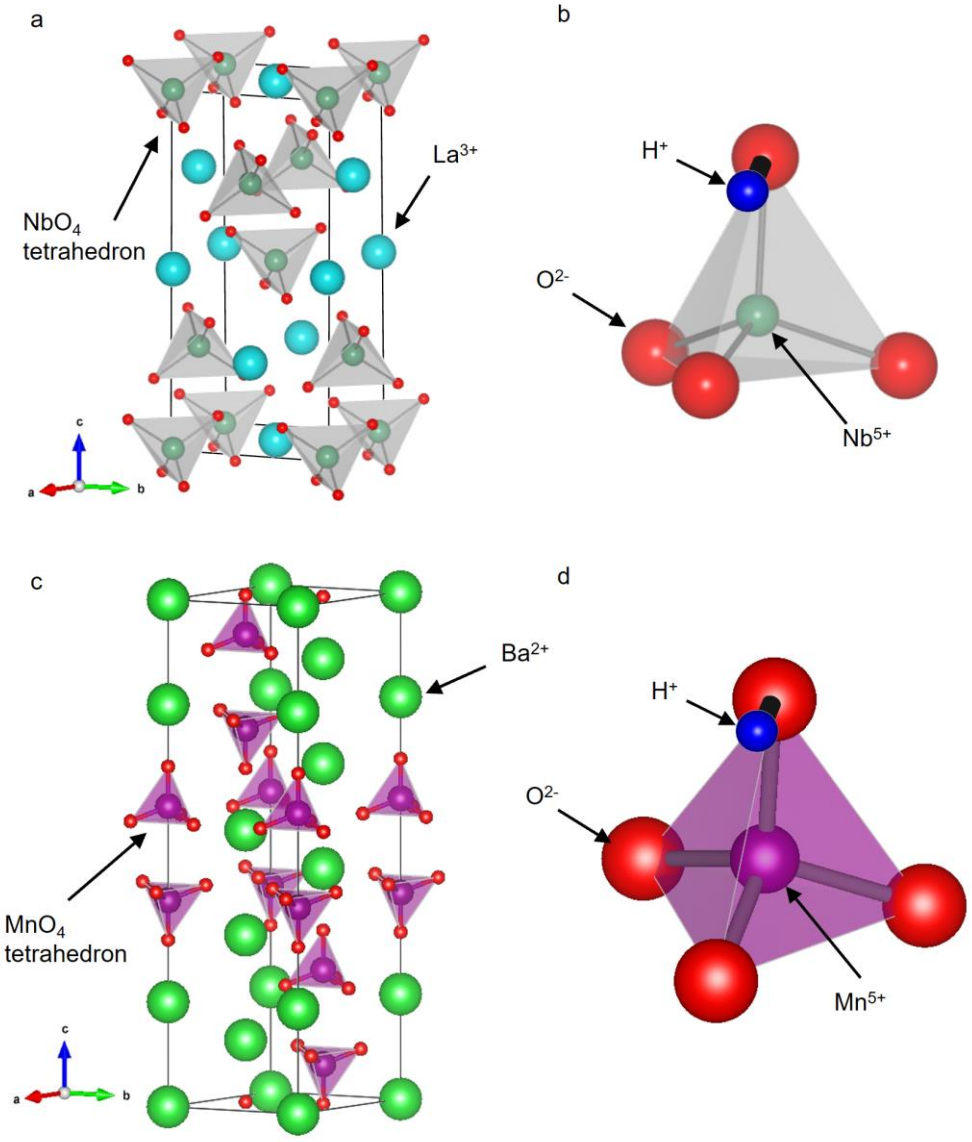

Figure 3-11. (a) Crystal structure of scheelite-type $LaNbO_4$ showing NbO_4 tetrahedra [36] and (b) proton site (blue) relative to an NbO_4^{3-} tetrahedron [36]. (c) Crystal structure of $Ba_3(MnO_4)_2$ showing MnO_4 tetrahedra and (d) predicted proton site (blue) relative to an MnO_4^{3-} tetrahedron

3.5. Conclusions

Herein, high-valence-state Mn(V) oxide $Ba_3(MnO_4)_2$ is demonstrated to be a promising anode electrocatalyst of H-SOECs. $Ba_3(MnO_4)_2$ exhibited poor semiconductor behavior while the conductivity increased by one order of magnitude at ~600°C, owing to the antiferromagnetic/paramagnetic phase transition, accompanied by a shape change of tetrahedral MnO_4^{3-} anions. Anode reactions with the SSC anode, which is a well-known electrode material for H-SOEC, is driven by the adsorption of water at the TPB and subsequent surface diffusion of oxygen species since the hydration of cobaltite is not thermodynamically favored. However, the $Ba_3(MnO_4)_2$ is favorably hydrated at temperatures below 700°C in wet air due to the large negative hydration enthalpy (–140 kJ mol^{-1}), and thus may exhibit significant proton conductivity. The $Ba_3(MnO_4)_2$ base anode, therefor, facilitates the OER directly with the surface-adsorbed water, and exhibits a lower polarization resistance than the SSC anode, because of the extension of the reaction area over the entire surface. The current results offer an opportunity to explore more active anode materials based on high-valence-state transition metal oxides.

3.6. References

1. Grimaud, A., Diaz-Morales, O., Han, B., Hong, W. T., Lee, Y. L., Giordano, L., *et al.* Activating lattice oxygen redox reactions in metal oxides to catalyse oxygen evolution. *Nature Chemistry*, *9*(5), 457-465 (2017).
2. Suntivich, J., May, K. J., Gasteiger, H. A., Goodenough, J. B., & Shao-Horn, Y. A perovskite oxide optimized for oxygen evolution catalysis from molecular orbital principles. *Science*, *334*(6061), 1383-1385 (2011).
3. Grimaud, A., May, K. J., Carlton, C. E., Lee, Y. L., Risch, M., Hong, W. T., *et al.* Double perovskites as a family of highly active catalysts for oxygen evolution in alkaline solution. *Nature Communications*, *4*, 2439 (2013).
4. Calle-Vallejo, F., Díaz-Morales, O. A., Kolb, M. J., & Koper, M. T. Why is bulk thermochemistry a good descriptor for the electrocatalytic activity of transition metal oxides?. *ACS Catalysis*, *5*(2), 869-873 (2015).
5. Rong, X., Parolin, J., & Kolpak, A. M. A fundamental relationship between reaction mechanism and stability in metal oxide catalysts for oxygen evolution. *ACS Catalysis*, *6*(2), 1153-1158 (2016).
6. Yagi, S., Yamada, I., Tsukasaki, H., Seno, A., Murakami, M., Fujii, H., *et al.* Covalency-reinforced oxygen evolution reaction catalyst. *Nature Communications*, *6*, 8249 (2015).
7. Yamada, I., Takamatsu, A., Asai, K., Shirakawa, T., Ohzuku, H., Seno, A., *et al.* Systematic study of descriptors for oxygen evolution reaction catalysis in perovskite oxides. *The Journal of Physical Chemistry C*, *122*(49), 27885-27892 (2018).
8. Lu, Z., Wang, H., Kong, D., Yan, K., Hsu, P. C., Zheng, G., *et al.* Electrochemical tuning of layered lithium transition metal oxides for improvement of oxygen evolution reaction. *Nature Communications*, *5*, 4345 (2014).
9. Mueller, D. N., Machala, M. L., Bluhm, H., & Chueh, W. C. Redox activity of surface oxygen anions in oxygen-deficient perovskite oxides during electrochemical reactions. *Nature Communications*, *6*, 6097 (2015).
10. Nakamura, T., Oike, R., Kimura, Y., Tamenori, Y., Kawada, T., & Amezawa, K. Operando Soft X-ray Absorption Spectroscopic Study on a Solid Oxide Fuel Cell Cathode during Electrochemical Oxygen Reduction. *ChemSusChem*, *10*(9), 2008-2014 (2017).
11. Weller, M. T., & Skinner, S. J. $Ba_3Mn_2O_8$ determined from neutron powder diffraction. *Acta Crystallographica Section C: Crystal Structure Communications*, *55*(2), 154-156 (1999).
12. Haugsrud, R., & Norby, T. High-Temperature Proton Conductivity in Acceptor-Substituted Rare-Earth Ortho-Tantalates, $LnTaO_4$. *Journal of the American Ceramic Society*, *90*(4), 1116-1121 (2007).

13. Yamamoto, T. Assignment of pre-edge peaks in K-edge x-ray absorption spectra of 3*d* transition metal compounds: Electric dipole or quadrupole?. *X-Ray Spectrometry: An International Journal*, *37*(6), 572-584 (2008).
14. Petersburg, C. F., Li, Z., Chernova, N. A., Whittingham, M. S., & Alamgir, F. M. Oxygen and transition metal involvement in the charge compensation mechanism of LiNi 1/3 Mn 1/3 Co 1/3 O 2 cathodes. *Journal of Materials Chemistry*, *22*(37), 19993-20000 (2012).
15. Farges, F. Ab initio and experimental pre-edge investigations of the Mn *K*-edge XANES in oxide-type materials. *Physical Review B*, *71*(15), 155109 (2005).
16. Uchida, M., Tanaka, H., Mitamura, H., Ishikawa, F., & Goto, T. High-field magnetization process in the S= 1 quantum spin system $Ba_3Mn_2O_8$. *Physical Review B*, *66*(5), 054429 (2002).
17. Rao, C. N. R. Transition metal oxides. *Annual Review of Physical Chemistry*, *40*, 291-326 (1989).
18. Haugsrud, R., & Norby, T. High-Temperature Proton Conductivity in Acceptor-Substituted Rare-Earth Ortho-Tantalates, $LnTaO_4$. *J. Am. Ceram. Soc.*, *90*(4), 1116-1121 (2007).
19. Choi, S., Kucharczyk, C. J., Liang, Y., Zhang, X., Takeuchi, I., Ji, H. I., & Haile, S. M. Exceptional power density and stability at intermediate temperatures in protonic ceramic fuel cells. *Nature Energy*, *3*(3), 202-210 (2018).
20. Strandbakke, R., Cherepanov, V. A., Zuev, A. Y., Tsvetkov, D. S., Argirusis, C., Sourkouni, G., *et al.* Gd-and Pr-based double perovskite cobaltites as oxygen electrodes for proton ceramic fuel cells and electrolyser cells. *Solid State Ionics*, *278*, 120-132 (2015).
21. Zohourian, R., Merkle, R., & Maier, J. Proton uptake into the protonic cathode material $BaCo_{0.4}Fe_{0.4}Zr_{0.2}O_{3-\delta}$ and comparison to protonic electrolyte materials. *Solid State Ionics*, *299*, 64-69 (2017).
22. Zohourian, R., Merkle, R., Raimondi, G., & Maier, J. Mixed-conducting perovskites as cathode materials for protonic ceramic fuel cells: understanding the trends in proton uptake. *Advanced Functional Materials*, *28*(35), 1801241 (2018).
23. Lim, D. K., Im, H. N., Song, S. J., & Yoo, H. I. Hydration of Proton-conducting $BaCe_{0.9}Y_{0.1}O_{3-\delta}$ by Decoupled Mass Transport. *Scientific Reports*, *7*(1), 1-9 (2017).
24. Bi, L., Shafi, S. P., & Traversa, E. Y-doped $BaZrO_3$ as a chemically stable electrolyte for proton-conducting solid oxide electrolysis cells (SOECs). *Journal of Materials Chemistry A*, *3*(11), 5815-5819 (2015).
25. Gan, Y., Zhang, J., Li, Y., Li, S., Xie, K., & Irvine, J. T. Composite oxygen electrode based on LSCM for steam electrolysis in a proton conducting solid oxide electrolyzer. *Journal of The Electrochemical Society*, *159*(11), F763 (2012).

26. Stuart, P. A., Unno, T., Kilner, J. A., & Skinner, S. J. Solid oxide proton conducting steam electrolysers. *Solid State Ionics*, *179*(21-26), 1120-1124 (2008).
27. He, F., Song, D., Peng, R., Meng, G., & Yang, S. Electrode performance and analysis of reversible solid oxide fuel cells with proton conducting electrolyte of $BaCe_{0.5}Zr_{0.3}Y_{0.2}O_{3-\delta}$. *Journal of Power Sources*, *195*(11), 3359-3364 (2010).
28. Li, S., & Xie, K. Composite oxygen electrode based on LSCF and BSCF for steam electrolysis in a proton-conducting solid oxide electrolyzer. *Journal of The Electrochemical Society*, *160*(2), F224 (2013).
29. Kobayashi, T., Kuroda, K., Jeong, S., Kwon, H., Zhu, C., Habazaki, H., & Aoki, Y. Analysis of the anode reaction of solid oxide electrolyzer cells with $BaZr_{0.4}Ce_{0.4}Y_{0.2}O_{3-\delta}$ electrolytes and $Sm_{0.5}Sr_{0.5}CoO_{3-\delta}$ anodes. *Journal of The Electrochemical Society*, *165*(5), F342 (2018).
30. Zhu, H., Ricote, S., Duan, C., O'Hayre, R. P., Tsvetkov, D. S., & Kee, R. J. Defect incorporation and transport within dense $BaZr_{0.8}Y_{0.2}O_{3-\delta}$ (BZY20) proton-conducting membranes. *Journal of The Electrochemical Society*, *165*(9), F581 (2018).
31. Oishi, M., Akoshima, S., Yashiro, K., Sato, K., Mizusaki, J., & Kawada, T. Defect structure analysis of B-site doped perovskite-type proton conducting oxide BaCeO3: Part 2: The electrical conductivity and diffusion coefficient of $BaCe_{0.9}Y_{0.1}O_{3-\delta}$. *Solid State Ionics*, *179*(39), 2240-2247 (2008).
32. Dippon, M., Babiniec, S. M., Ding, H., Ricote, S., & Sullivan, N. P. Exploring electronic conduction through $BaCe_xZr_{0.9-x}Y_{0.1}O_{3-d}$ proton-conducting ceramics. *Solid State Ionics*, *286*, 117-121 (2016).
33. Bieberle-Hütter, A., Søgaard, M., & Tuller, H. L. Electrical and electrochemical characterization of microstructured thin film $La_{1-x}Sr_xCoO_3$ electrodes. *Solid State Ionics*, *177*(19-25), 1969-1975 (2006).
34. He, F., Wu, T., Peng, R., & Xia, C. Cathode reaction models and performance analysis of $Sm_{0.5}Sr_{0.5}CoO_{3-\delta}$–$BaCe_{0.8}Sm_{0.2}O_{3-\delta}$ composite cathode for solid oxide fuel cells with proton conducting electrolyte. *Journal of Power Sources*, *194*(1), 263-268 (2009).
35. Yang, S., He, T., & He, Q. $Sm_{0.5}Sr_{0.5}CoO_3$ cathode material from glycine-nitrate process: Formation, characterization, and application in $LaGaO_3$-based solid oxide fuel cells. *Journal of Alloys and Compounds*, *450*(1-2), 400-404 (2008).
36. Mather, G. C., Fisher, C. A., & Islam, M. S. Defects, dopants, and protons in LaNbO4. *Chemistry of Materials*, *22*(21), 5912-5917 (2010).

Chapter 4

Hydrogen permeable cathode of barium indate zirconate perovskite oxyhydride with enhanced hydride ion conductivity

4.1. Objective of chapter 4

The Faradaic efficiency of H-SOEC is expected to improve by applying dry gas to the cathode atmosphere, as mentioned in chapter 1. For this, it is desirable to design hydrogen permeable membrane cathode type structure. This motivates me to develop the alternative cathode materials that shows the hydrogen solubility and permeability without relying on the proton uptake by hydration. Oxyhydride with the hydride (H^-) ion conductivity is potential candidate for such cathodes, because such a material can generate H^- ion defects by the 'hydrogenation' i.e., the association of oxygen vacancies and hydrogen molecules in dry atmosphere.

Fluorite-type $LnH_{3-2x}O_x$ [1,2] and Ruddlesden–Popper-type $La_{2-x-y}Sr_{x+y}LiH_{1-x+y}O_{3-y}$ [3] Ba_2ScHO_3 [4], and Ba_2YHO_3 [5] have been reported to show H^- ion conductivity, and some of these achieve 0.01 S cm^{-1} at 400°C [1]. Despite the excellent conductivity, these oxyhydrides tend to decompose at several hundreds' °C [1-8] and their synthesis requires strong reducing conditions with the presence of hydrogenation reagents, such as metal hydrides of the constituent cations, $LiAlH_4$ or CaH_2 [1-8], attributed to the lability of H^- anion. The harsh preparation conditions and pyrolytic nature, however, are obstacle to their applications because limit processing for material design into porous substances, composites, dense membrane and so on. Thus, a strong motivation exists to explore highly durable oxyhydride ceramics with bulk H^- ion conductivity.

Some pioneer works [9-11] have predicted the possibility for the formation of H^- ion defects in perovskites, such as $SrTi_{1-x}Fe_xO_{3-x/2}$ at very low oxygen partial pressure. $SrTi_{0.5}Fe_{0.5}O_{2.75}$ was deduced to show the negatively-charged hydrogen ion conduction, based on the electromotive forces of the

concentration cells, and the conductivity was estimated to reach 10^{-2} S cm^{-1} at 800°C [11]. In a recent year, cubic perovskite $BaTiO_{1-x}H_x$ ($x \leq 0.6$) have been synthesized by the chemical reaction between parent oxides ($BaTiO_3$) and hydrogen sources (CaH_2) via O^{2-}/H^- anion substitution. The oxyhydrides were air stable and persistent without decomposition by boiling in a hot water [12]. Unfortunately, the bulk diffusivity of H^- ions was relatively low because the relatively low concentration of anion vacancy retards the long-range hopping along the nearest neighbor anion sites [13,14]. Nevertheless, these findings implies that the perovskite oxyhydride systems having significantly large anion deficiency are potential candidate of H^- ion conductors combing relatively high conductivity and durability [15].

In this chapter, I discovered highly durable oxyhydride perovskite $BaZr_{0.5}In(II)_{0.5}O_{2.25}H_{0.5}$ with enhanced H^- ion electron mixed conductivity. $BaZr_{0.5}In(III)_{0.5}O_{2.75}$, as the parent phase, was reductively hydrogenated to $BaZr_{0.5}In(II)_{0.5}O_{2.25}H_{0.5}$ via simple H_2 gas annealing at 800°C under ambient pressure with the incorporation of H^- ions with simultaneous oxygen vacancy formation. Membrane devices comprising dense $BaZr_{0.5}In_{0.5}O_{2.25}H_{0.5}$ films on porous Ni-cermet supports were fabricated by conventional sintering and post-reduction, because low lattice contraction (–0.07%) following hydrogenation allowed for the bulk hydrogenation of $BaZr_{0.5}In_{0.5}O_{2.75}$ sinters without structural collapse. The resultant devices exhibited higher hydrogen permeability than protonic Ni-$(Ba,Sr)Zr_xCe_{1-x-y}M_yO_{3-\delta}$ ((BS)ZCM; M = Y, Eu, etc.) composite membranes [16-19] at 500°C because $BaZr_{0.5}In(II)_{0.5}O_{2.25}H_{0.5}$ allows H^- ion hopping between the nearest neighbor anion sites due to the significantly high oxygen deficiency (25% of O sites are defected), giving rise to H^- ion conductivity of 10^{-3} S cm^{-1}. Given their superior H^- ion conductivity and ease of manufacturing, the synthesized materials have great potential for applications in mixed conducting electrodes and hydrogen permeable membrane supports of ceramic electrochemical cells.

4.2 Experimental

4.2.1. Samples

$BaZr_{0.5}In_{0.5}O_{3-\delta}$ (BZI) powders were synthesized via a solid-state reaction. Stoichiometric amounts of the starting materials, including $BaCO_3$ (High Purity Chemicals; 99.95%), ZrO_2 (High Purity Chemicals; 98%), and In_2O_3 (High Purity Chemicals; 99.99%), were ball-milled for 2 h, pressed into pellets, and calcined at 900°C for 12 h, at 1300°C for 12 h, and then at 1500°C for 8 h with intermittent ball milling for 2 h and re-pressing. The sinters were pulverized, and the obtained powders were applied as pristine BZI.

Wet-BZI powders were prepared by heating pristine BZI in 3%-D_2O/Ar gas at 275°C for 144 h according to a previously reported method.[22] The humidified gas was prepared by bubbling Ar gas through a D_2O bath at 25°C at a flow rate of 50 cm^3 min^{-1}. H-BZI and D-BZI powders were prepared by heating BZI at 800°C for 24 h in dry H_2 and D_2, respectively, and then cooling to room temperature in the same atmosphere. deD-BZI powders were prepared by heating BZI at 800°C for 24 h in D_2, heating at 700°C for 3 h in 0.1%-D_2/Ar, and then cooling to room temperature in the same atmosphere. All dry gases used in this study were purified by passing through molecular sieves and had a dew point of < −70°C, as monitored via the exhaust gases with a YSZ-O_2 sensor.

4.2.2 Characterization

The phase purity of the samples was evaluated by X-ray diffraction (XRD) analysis in the 2θ range of 20°–80° at a scan rate of 5° min^{-1} using an Ultima IV instrument (Rigaku) with CuKα radiation.

Thermogravimetric analysis (TGA) was performed using an STA2500 thermogravimetric analyzer (Netzsch) under a flow of dry H_2 or Ar at 50 cm^3 min^{-1}. Magic-angle-spinning nuclear magnetic resonance (NMR) spectroscopy was performed using a JNM-ECAII spectrometer (JEOL Ltd.). The measurements were recorded on a spectrometer operated at a resonance frequency of 598.97 MHz and equipped with a magic-angle-spinning probe with a diameter of 3.2 mm. Electron spin resonance (ESR) spectroscopy was conducted using an ESR04 spectrometer (Keycom) at 9.6 G Hz. 2,2-

Diphenyl-1-picrylhydrazyl (DPPH) was used as an internal standard. Pressure–composition–temperature (PCT) measurements of the H-BZI powders were carried out using a PCT-2SDWIN apparatus (Suzuki Shokan Co., Ltd.) to monitor the H_2 sorption/desorption capacity of the sample. The sample was evacuated once at an elevated temperature under a pressure of 10^{-4} Pa and then exposed to H_2 gas.

Neutron powder diffraction (NPD) measurements of the BZI samples were carried out using the SPICA time-of-flight (TOF) neutron powder diffractometer installed at Japan Proton Accelerator Research Complex (J-PARC). The sample was placed in a cylindrical V cell (radius, 6 mm; height, 55 mm), and the diffraction data were collected at room temperature. The Z-Rietveld program was used to refine the lattice and structural parameters [20,21]. The X-ray absorption fine structures (XAFS) of the In and Zr K-edges were obtained on BL07 at the SAGA Light Source. The XAFS for In and Zr K-edges was recorded in transparent mode from 27613 to 28918 eV and from 17670 to 19233 eV (30 min $scan^{-1}$), respectively. All samples were mixed with BN powder to achieve the suitable absorbance at the appropriate edge energy.

4.2.3. Electrical conductivity and hydrogen permeability

Sintered discs (ϕ12 mm × 0.8 mm) and bars (ϕ3.5 mm × 10 mm) of H-BZI were prepared as follows. BZI powders were ball-milled with $Zn(NO_3)_2{\cdot}6H_2O$ (Wako Chemicals; Zn/BZI molar ratio, 0.01) as a sintering aid for 3 h. The resulting powders were uniaxially pressed into pellets (ϕ 15 mm × 1.5 mm or ϕ 5 mm × 15 mm) under 20 MPa and subsequently pressed under a hydrostatic pressure of 100 MPa in an isostatic press. The samples were then sintered at 1500°C for 8 h. After polishing the edges, the BZI sinters were hydrogenated by heating at 800°C for 3 days in dry H_2 to obtain the H-BZI sinters.

DC conductivity measurements were performed by the four-probe technique using a SP-300 galvano/potentiostat (Biologic) equipped with a frequency response analyzer. Impedance spectra were measured by the two-probe method with the same apparatus used for the DC measurements at an AC

amplitude of 30 mV. Au wires (ϕ0.1 mm) were attached to the samples with Au paste to achieve electrical contact.

Hydrogen concentration cells of {30%-H_2/Ar, Pd(1) | H-BZI | Pd(2), H_2} were constructed with the H-BZI sintered discs to evaluate their hydrogen pumping ability. Pd thin-film electrodes (Pd(1) and Pd(2); thickness, 200 nm) were deposited on the two surfaces of an H-BZI sinter disc by RF magnetron sputtering. The sputtering was conducted using Ulvac ACS-3000 vacuum system at a cathode power of 150 W in Ar pressure of 1 Pa. An alumina tube (ϕ10 mm) was attached to both surfaces of the H-BZI discs with a molten glass seal. Dry 30%-H_2/Ar mixed gas was fed to the Pd(1) side at a rate of 20 cm^3 min^{-1}, and pure H_2 gas was fed to the Pd(2) side at a rate of 50 cm^3 min^{-1}. A DC bias was applied between the Pd(1) working electrode and the Pd(2) counter electrode by the SP-300 apparatus, and the exhaust gases at the Pd(1) side were analyzed by a GC400 micro gas chromatograph (Agilent).

H_2 permeation tests were conducted on a membrane device comprising a dense H-BZI thin film on a porous Ni-(H-BZI) cermet support. BZI, NiO, and ethyl cellulose (as a pore former) were mixed at a mass ratio of 50:50:5.5 in ethanol with ball-milling and then pressed in the same way as described above to obtain green pellets that were used as cermet supports. The NiO-BZI buffer and BZI layers were spin-coated on the green pellets using a 1H-D7 spin-coater (MISAKA). The NiO-BZI (mass ratio, 50:50) and BZI slurries were prepared by dispersing each powder in a solution containing a dispersant and binder and then spin-coated on the surfaces of the green pellets. After spin-coating, the BZI device precursors were cofired first at 350°C for 2 h and then at 1400°C for 8 h. Finally, the device precursors were heated at 800°C for 6 h in dry H_2 to reduce NiO to Ni and hydrogenate BZI to H-BZI. Half-cells of {10%-H_2/Ar | H-BZI | Ni-(H-BZI) cermet,100 or 80%-H_2/N_2} were constructed by feeding dry 10%-H_2/Ar mixed gas to the film surface at a rate of 20 cm^3 min^{-1} and 100 or 80%-H_2/N_2 gas to the cermet side at a rate of 50 cm^3 min^{-1}. Exhaust gases in the low-concentration side were analyzed using the GC400 micro gas chromatograph (Agilent).

4.3. Results

4.3.1. Chemical transformation of $BaZr_{0.5}In_{0.5}O_{3-\delta}$ perovskite into an oxyhydride

The cubic perovskite $BaZr_{0.5}In_{0.5}O_{3-\delta}$ (BZI) has been intensively studied over the last few decades [22-27] because it shows H^+ conductivity via the hydration reaction in a wet atmosphere, as indicated in Equation (4-1):

$$H_2O + V_O^{\bullet\bullet} + O_O^{\times} \rightleftharpoons 2OH_O^{\bullet} \quad (4\text{-}1)$$

Hereafter, the defects and related reactions are represented in Kröger–Vink notation. $V_O^{\bullet\bullet}$, $O_O^{\times}$ and $OH_O^{\bullet}$ are a oxygen vacancy, lattice oxygen and proton defect, respectively. BZI appeared to undergo a new type of thermochemical transformation. In this transformation, the parent oxide is reductively hydrogenated with H_2 gas at elevated temperatures and then transformed into an isomorphous oxyhydroxide phase (Figure 4-1). Thermogravimetric analysis (TGA) confirms that BZI experiences a significant mass loss (Δm) of ~1.2 wt% at approximately 500°C in dry H_2 due to loss of oxygen; this Δm is much larger than the loss observed (~0.3 wt%) at approximately 300°C in dry Ar due to dehydration (Figure 4-1a) [28]. A thermogravimetric plateau, which indicates the formation of a new phase, appears in the temperature range of approximately 700–900°C. This finding can be confirmed by the results of isothermal TGA at 800°C with atmospheric switching from dry Ar to dry H_2 (Figure 4-1a, inset). The weight of BZI abruptly decreases upon exposure to H_2 by loss of oxygen and stabilizes within 1 h, ultimately leading to a Δm of –2.7 wt%. X-ray diffractometry (XRD) confirms that the cubic perovskite structure of the BZI specimens is preserved after heating at 800°C in dry H_2 for 12 h, although the color of the material changes from milky white to black (Figure 4-1b). Combined XRD and TGA confirms that BZI is reduced to highly oxygen-deficient perovskite phase by H_2 annealing at 800°C. From inset of Figure 4-1a, the composition of the reduced phase is calculated to $BaZr_{0.5}In_{0.5}O_{2.27}$ with Δm at t = 300 min under the assumption that the mass change observed is due to oxygen loss only and BZI at t = 0 is completely dehydrated, thereby, assumed to $BaZr_{0.5}In_{0.5}O_{2.75}$. Here, t is the time of H_2 exposure. The mean valence of In in the reduced phase is calculated to 1.08+.

Lattice constant (*a*) decreases from 4.2020 Å to 4.1990 Å after H_2 heating, indicating lattice contraction is minimal (0.07%) despite the large oxygen defects formed. This feature implies the O^{2-}/H^- substitution because H^- anion has the similar ionic radii as O^{2-} anion [29]. ^1H nuclear magnetic resonance (^1H-NMR) spectroscopy confirms the incorporation of hydride anions into the perovskite lattice (Figure 4-1c). The NMR spectrum of pristine BZI shows a broad peak in the range of 0–10 ppm, which could be assigned to hydroxyl (OH^-) groups on the surface and the bulk of the oxide [30,31]. The ^1H-NMR spectrum of post-H_2 annealed BZI exhibits a sharp peak at approximately 5 ppm, which is consistent with the signal of the H^- ion in the perovskite lattice [12,32,33].

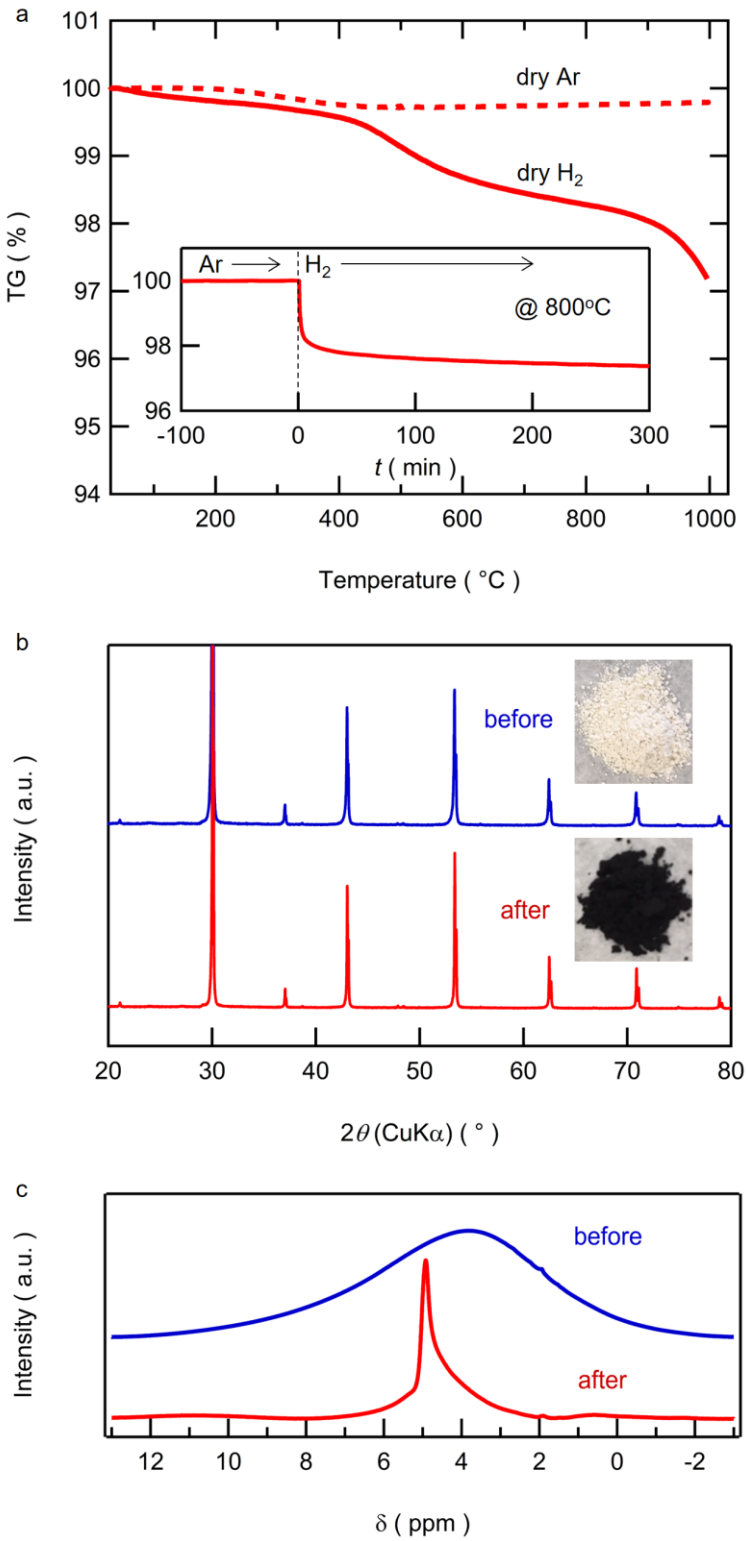

Figure 4-1. Hydrogenation of BZI. (a) Thermogravimetric (TG) curves measured in dry Ar (dotted line) and H_2 (solid line). Inset: Isothermal TG curve obtained with atmosphere switching from Ar to H_2 at 800 °C. (b) X-ray diffractions patterns and (c) ^1H nuclear magnetic resonance spectra of BZI before (blue) and after (red) heating in dry H_2 at 800 °C for 8 h.

Neutron diffraction (ND) Rietveld structure refinement was conducted on BZI based on a cubic perovskite (space group, $Pm\bar{3}m$) structure with various H dopant sites to clarify the anion configuration and H species of the sample (Figure 4-2). Cubic perovskites may contain three types of H sites [12,22,34] (Figures 4-2a–c): (1) a proton on an interstitial 24k site ($OH_O^\bullet$ defect), which is a typical proton defect site of perovskite proton conductors [22], (2) a H^- ion in O vacancies in 3d sites ($H_O^\bullet$ defect), and (3) a H^- ion on an interstitial 3c sites at the [100] face center (H_i' defect). $H_O^\bullet$ defect-type H^- ions are known to form in various perovskite oxihydrides [12], while H_i' defect-type H^- ions have only been predicted theoretically [34]. In this work, we examined the H sites of four specimens, namely, pristine BZI, BZI hydrated at 275°C for 6 days in 3%-D_2O/Ar (i.e., wet-BZI), BZI hydrogenated at 800°C for 1 days in H_2 or D_2 (i.e., H-BZI and D-BZI, respectively), and BZI hydrogenated once at 800°C for 1 days in D_2 and then dehydrogenated at 700°C for 1 h in 0.1%-D_2/Ar (i.e., deD-BZI).

ND patterns of pristine BZI is refined well by the structure model without any H dopants, which confirms the water contents of pristine BZI is quite small, in agreement with the previous reports for the structure refinement of $BaZr_{0.5}In_{0.5}O_{3-\delta}$ (Figure 4-3a and Table 4-1) [23]. The structure of wet-BZI is refined very well by ND Rietveld analysis with the $OD_O^\bullet$ proton defects (Figure 4-2a and d and Table 4-1). The nuclear density map of wet-BZI reconstructed using the maximum entropy method (MEM) reveals a clear nuclear spot on 24k sites, thereby confirming the incorporation of $OD_O^\bullet$ defects (Figure 4-2f). Thus, the composition of wet-BZI is $BaZr_{0.5}In_{0.5}O_{2.53}(OD_O)_{0.44}$ (Table 4-1), which is in agreement with previous results reported for hydrated $BaZr_{0.5}In_{0.5}O_{3-\delta}$ [23].

D-BZI could not be refined with the protonic $OD_O^\bullet$ defects because the corresponding fitting shows very low 24k site occupancy (~0.0008(1)) with an R_{wp} of over 7%. Infrared spectroscopy indicates the absence of OH^- groups in H-BZI because the OH^- stretching band of H-BZI was much smaller than that of wet-BZI (Figure 4-4). Refinement with the hydridic $D_O^\bullet$ defect gives a better fit, with an R_{wp} of 6.07% and R_p of 4.05%. The MEM nuclear density map of D-BZI shows a positive nuclear density at the [100] face center (3c site; Figure 4-2c and g), which confirms the existence of hydridic H_i' defects. Hence, the coexistence of $OD_O^\bullet$ and D_i' defect type D^- ions was considered during fitting, and

remarkably improved refinement results, with R_{wp} = 5.37% and R_p = 3.75%, were obtained (Figure 4-2e and Table 4-1). The composition of D-BZI was subsequently determined to $BaZr_{0.5}In_{0.5}O_{2.28}(D_O)_{0.29}(D_i)_{0.19}$, as listed in Table 4-1. The oxygen content in this composition is in agreement with the corresponding values determined by TGA ($BaZr_{0.5}In_{0.5}O_{2.27}$). The chemical composition by ND suggests mean valence of In equaling +2.08 as calculated by fixing the formal valences of Ba^{2+}, Zr^{4+}, O^{2-}, and H^- ions (Table 4-1). ESR and XANES measurements also confirms H-BZI mainly takes In(II) valence state, as mentioned below. Combined these experimental results unambiguously demonstrate that $BaZr_{0.5}In(III)_{0.5}O_{2.75}$ perovskite transforms into an isomorphous oxyhydroxide with a nominal composition of $BaZr_{0.5}In(II)_{0.5}O_{2.25}H_{0.5}$ in an ambient H_2 atmosphere. This transformation could be rewritten by the hypothetical consecutive reactions of In reduction and oxidative hydrogenation as follows.

In reduction: $BaZr_{0.5}In(III)_{0.5}O_{2.75} + H_2 \rightarrow BaZr_{0.5}In(I)_{0.5}O_{2.25} + 0.5\ H_2O$ (4-2)

Oxidative hydrogenation: $BaZr_{0.5}In(I)_{0.5}O_{2.25} + 0.25\ H_2 \rightarrow BaZr_{0.5}In(II)_{0.5}O_{2.25}H_{0.5}$ (4-3)

Reaction (4-2) and (4-3) might proceed simultaneously during H_2 annealing. The resultant oxyhydride $BaZr_{0.5}In(II)_{0.5}O_{2.25}H_{0.5}$ must be in equilibria with H_2 gases by following defect reactions.

$O_O^{\times} + H_2 + 2h^{\bullet} \rightarrow H_2O + V_O^{\bullet\bullet}$ (4-4)

$1/2\ H_2 + V_O^{\bullet\bullet} \rightarrow H_O^{\bullet} + h^{\bullet}$ (4-5)

$1/2\ H_2 \rightarrow H_i' + h^{\bullet}$ (4-6)

Here $h^{\bullet}$ indicates an electron hole.

Table 4-1. Structural parameters refined by neutron diffraction Rietveld analysis.

	R_{wp} (%)	R_p (%)	a /Å	$g(O_o)$	$g(H_{OH})$	$g(H_O)$	$g(H_i)$	composition	In valence
BZI	13.8	7.58	4.202001(2)	0.9119(6)	-	-	-	$BaZr_{0.5}In_{0.5}O_{2.74}$	+2.96
Wet-BZI	5.85	4.78	4.239737(5)	0.9913(4)	0.0184(2)	-	-	$BaZr_{0.5}In_{0.5}O_{2.53}(OD_O)_{0.44}$	+3.00
D-BZI	5.37	3.75	4.198989(3)	0.7610(2)	-	0.0971(2)	0.0639(4)	$BaZr_{0.5}In_{0.5}O_{2.28}(Do)_{0.29}(D_i)_{0.19}$	+2.08
deD-BZI	4.43	3.77	4.198248(3)	0.7576(4)	-	0.0758(3)	0.0617(8)	$BaZr_{0.5}In_{0.5}O_{2.27}(Do)_{0.23}(D_i)_{0.19}$	+1.92

A. BZI

Atom	site	g	x	y	z	U_{11} /Å^2	U_{22} /Å^2	U_{33} /Å^2	U /Å^2
Ba	1b	1	0.5	0.5	0.5	0.366(4)	$=U_{11}$	$=U_{11}$	0.366(4)
Zr/In	1a	0.5	0	0	0	0.157(4)	$=U_{11}$	$=U_{11}$	0.157(4)
O	3d	0.9119(6)	0.5	0	0	0.062(7)	1.721(6)	$=U_{22}$	1.168(4)

Composition: $BaZr_{0.5}In_{0.5}O_{2.74}$, Unit cell: $Pm\bar{3}m$, a = 4.202001(2) Å
R_{wp} = 13.78%, R_p = 7.58%, R_e = 1.66%, S = 8.29%, R_B = 7.95%, R_F = 5.48%

B. W-BZI

Atom	site	g	x	y	z	U_{11} /Å^2	U_{22} /Å^2	U_{33} /Å^2	U /Å^2
Ba	1b	1	0.5	0.5	0.5	1.154(8)	$=U_{11}$	$=U_{11}$	1.154(8)
Zr/In	1a	0.5	0	0	0	0.425(7)	$=U_{11}$	$=U_{11}$	0.425(7)
O	3d	0.9913 (4)	0.5	0	0	0.119(10)	1.777(8)	$=U_{22}$	1.224(5)
D_{OD}	24k	0.0184(2)	0.55	0.23	0	$=U_{11}$(O)	$=U_{22}$(O)	$=U_{33}$(O)	$=U$(O)

Composition:$BaZr_{0.5}In_{0.5}O_{2.53}(OD_O)_{0.44}$, Unit cell: $Pm\bar{3}m$, a = 4.239737(5) Å
R_{wp} = 5.85%, R_p = 4.78%, R_e = 2.50%, S = 2.34%, R_B = 9.92%, R_F = 14.27%

C. D-BZI

Atom	site	g	x	y	z	U_{11} /Å^2	U_{22} /Å^2	U_{33} /Å^2	U /Å^2
Ba	1b	1	0.5	0.5	0.5	0.535(5)	$=U_{11}$	$=U_{11}$	0.535(5)
Zr/In	1a	0.5	0	0	0	0.180(4)	$=U_{11}$	$=U_{11}$	0.1804)
O	3d	0.7610(2)	0.5	0	0	0.130(8)	1.613(8)	$=U_{22}$	1.119(6)
D_O	3d	0.0971(2)	0.5	0	0	$=U_{11}$(O)	$=U_{22}$(O)	$=U_{33}$(O)	$=U$(O)
D_i	3c	0.0639(4)	0.5	0.5	0	2	2	2	2

Composition: $BaZr_{0.5}In_{0.5}O_{2.28}$ $(Do)_{0.29}(D_i)_{0.19}$, Unit cell: $Pm\bar{3}m$, a = 4.198989(3) Å
R_{wp} = 5.37%, R_p = 3.75%, R_e = 1.79%, S = 2.99%, R_B = 4.35, R_F = 4.86%

D. DeD-BZI

Atom	site	g	x	y	z	U_{11} /Å^2	U_{22} /Å^2	U_{33} /Å^2	U / A2
Ba	1b	1	0.5	0.5	0.5	0.719(5)	$=U_{11}$	$=U_{11}$	0.719(5)
Zr/In	1a	0.5	0	0	0	0.331(5)	$=U_{11}$	$=U_{11}$	0.331(5)
O	3d	0.7576(4)	0.5	0	0	0.156(8)	1.705(7)	$=U_{22}$	1.189(4)
D_O	3d	0.0758(3)	0.5	0	0	$=U_{11}$(O)	$=U_{22}$(O)	$=U_{33}$(O)	$=U$(O)
D_i	3c	0.0617(8)	0.5	0.5	0	2	2	2	2

Composition: $BaZr_{0.5}In_{0.5}O_{2.27}(Do)_{0.23}(D_i)_{0.19}$, Unit cell: $Pm\bar{3}m$, a = 4.198248(3) Å
R_{wp} = 4.37%, R_p = 3.73%, R_e = 3.073, S = 1.42%, R_B = 7.12%, R_F = 6.87%

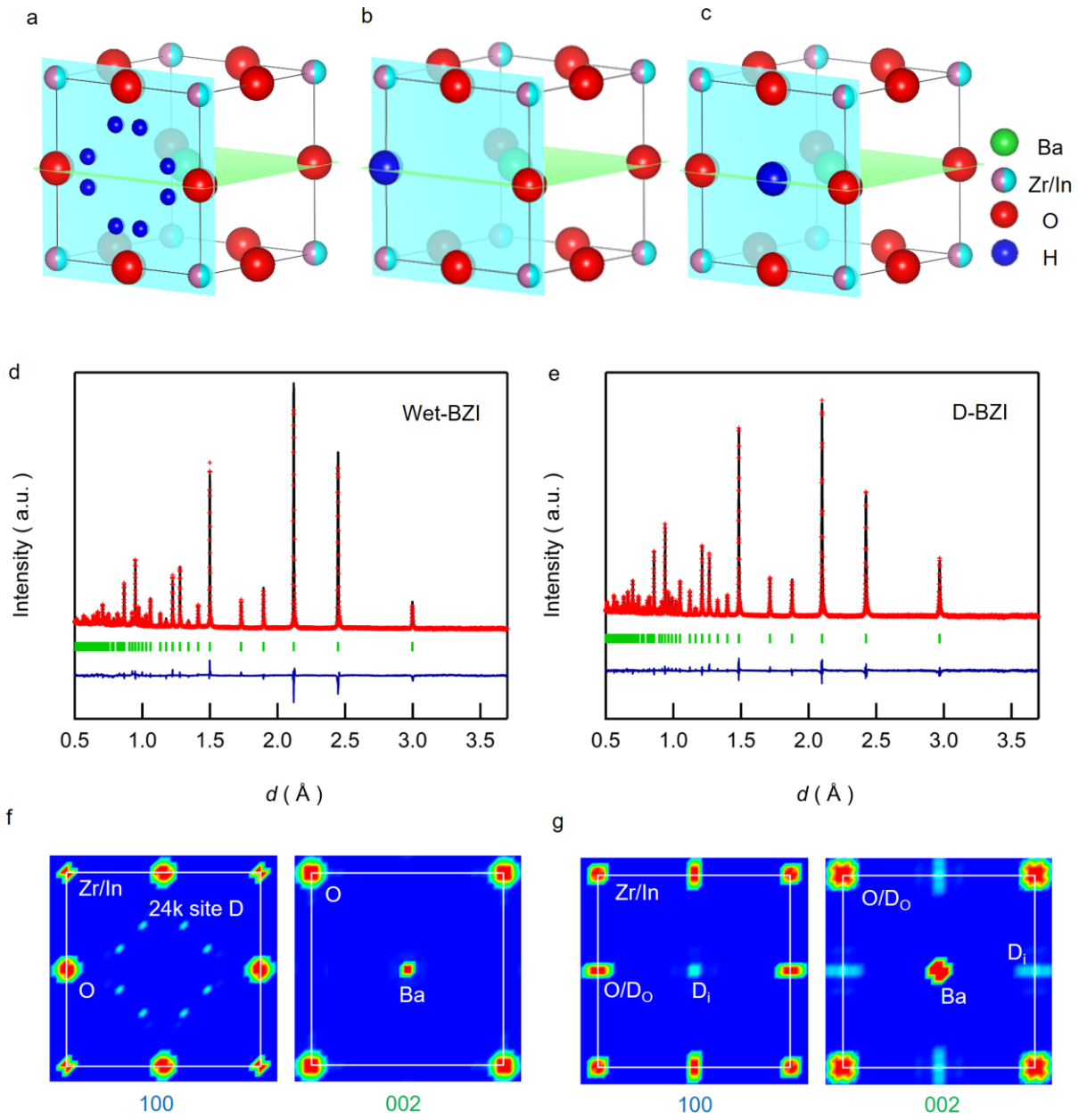

Figure 4-2. Powder neutron diffraction Rietveld structure refinement of BZI. Defect model of hydrogen impurities in cubic perovskites: (a) proton at 24k sites ($OH_O^{\bullet}$), (b) hydride (H^-) ion in O vacancies at 3d sites ($H_O^{\bullet}$), and (c) H^- ion at the [100] face center of 3c sites (H_i'). Light blue and green planes indicate the [100] and [002] planes, respectively, of cubic perovskite. Rietveld profiles of (d) Wet-BZI and (e) D-BZI. Maximum entropy method mapping of (f) wet-BZI and (g) D-BZI on the [100] and [002] planes.

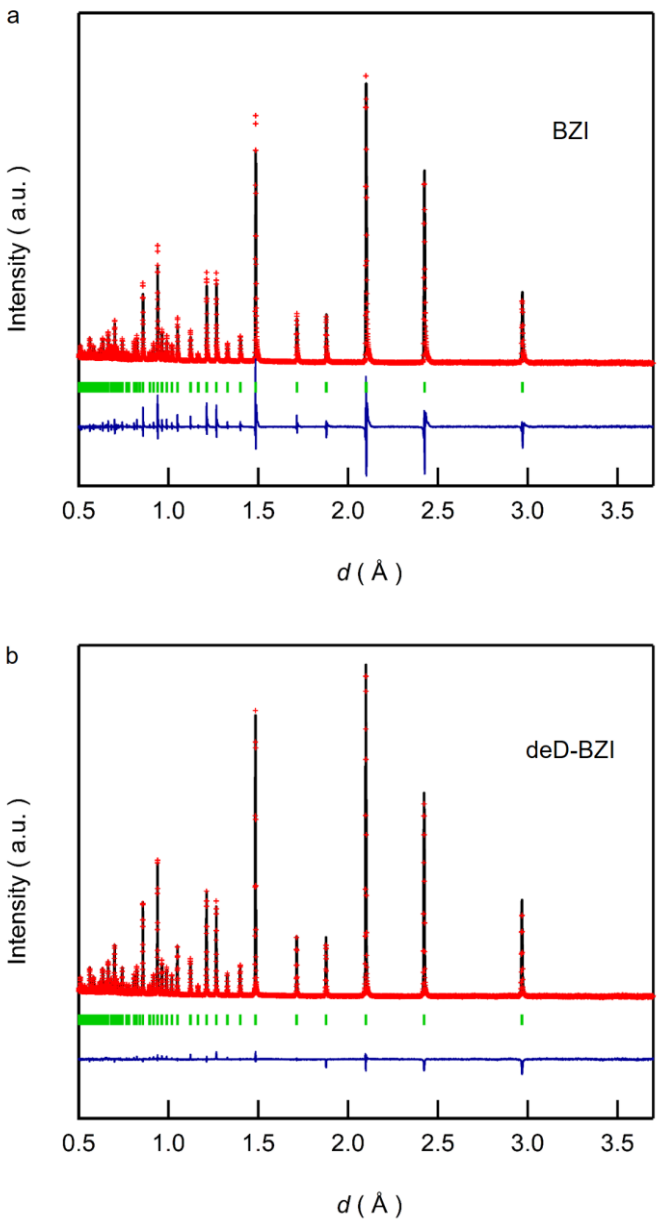

Figure 4-3. Powder neutron diffraction Rietveld profiles of (a) as prepared BZI and (b) deD-BZI.

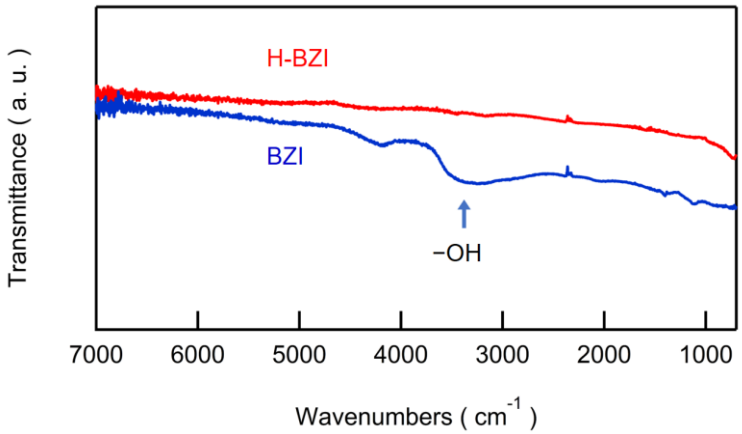

Figure 4-4. Fourier transform infrared (FTIR) spectra

The structural refinement of deD-BZI was smoothly conducted with the $D_O^{\bullet}$–D_i' coexisting model to yield $BaZr_{0.5}In_{0.5}O_{2.27}(D_O)_{0.23}(D_i)_{0.19}$ (Table 4-1). The difference in the composition between D-BZI and deD-BZI reveals that $[H_O^{\bullet}]$ decreases by 0.06 but $[H_i']$ remains unchanged with dehydrogenation treatment by heating in 0.1%-H_2/Ar at 700°C. Here [] indicates the molar fraction of the defects. These indicates $[H_O^{\bullet}]$ is variable in response to hydrogen partial pressure (p_{H2}) according to defect reaction (4-5) but $[H_i']$ is invariable at p_{H2} above 1 kPa because the defect reaction (4-6) largely shifts to the right side in the p_{H2} region.

X-ray absorption fine structure (XAFS) analysis confirmed the reduction of In atoms following the chemical transformation (Figure 4-5a). The In-*K* absorption edges of H-BZI clearly shift toward lower energies in comparison with those of pristine BZI, and the E_0 values of the former and latter are 27945.3 and 27944.2 eV, respectively. Given that the absorption edge of transition-metal oxides is generally proportional to their mean valence state because the core electron binding energy linearly increases with the positive charge on the cation [35,36], the mean valence of In in H-BZI is roughly estimated to be +1.8 from the relative shift in E_0 between In foil and pristine BZI. This value is in close agreement with that (+2.08) calculated from the chemical composition (Table 4-1). Electron spin resonance (ESR)

spectroscopy confirms the inclusion of In(II) states with a $5s^1$ electronic configuration in H-BZI (Figure 4-6). Pristine BZI does not show an ESR signal, whereas H-BZI shows a broad, asymmetric ESR signal at $g = 2.041$. The spin density of H-BZI is roughly estimated by comparison with the 2,2-Diphenyl-1-picrylhydrazyl (DPPH) reference signal to be in the order of 10^{21} cm^{-3}, which is consistent with the population of In atoms (6.7×10^{21} cm^{-3}). The Zr-K edge XANES spectra do not indicate a chemical shift, which confirms that Zr atoms are not reduced by hydrogenation (Figure 4-5b).

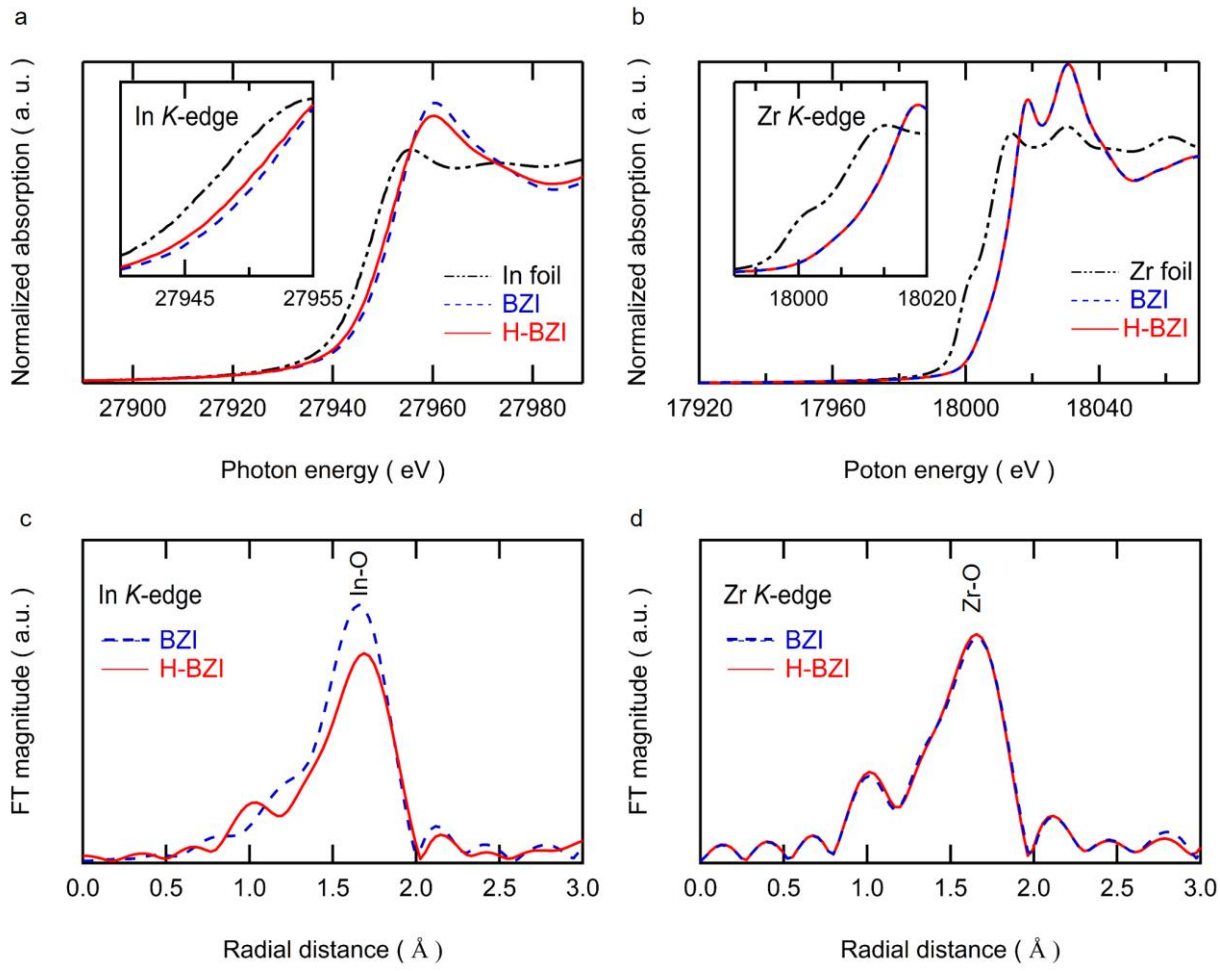

Figure 4-5. Valence state and coordination environment of In and Zr atoms. (a) In *K*-edge XANES and (b) Zr *K*-edge XANES of BZI and H-BZI. The black line in (a, b) shows the In or Zr foil. Radial distribution function (RDF) around the (c) In and (d) Zr atoms of BZI and H-BZI. Blue line: BZI; red line: H-BZI.

4.3.2. Hydrogen sorption/desorption

The structural features refined by ND reflects their hydrogen sorption behavior. The pressure–composition–temperature (PCT) measurements were conducted for H-BZI as depicted in Figure 4-7. Here, H-BZI was once heated to 800°C in vacuum (10^{-4} Pa) and then hydrogen absorption isotherms were measured by controlling p_{H2}, which clarified the hydrogen uptake (δ_H) in relation to the base value in vacuum at each temperature. H-BZI is capable of reversible absorption/desorption of H_2 in response to p_{H2}, in which δ_H is proportional to $p_{H2}^{0.5}$ over a wide p_{H2} range at temperatures above 400°C (Figure 4-7a). This provides clear evidence for the incorporation of hydride ion according to Equation (4-5) and/or (4-6), because both equations give $p_{H2}^{0.5}$ dependence of $[H_O^\bullet]$ and $[H_i']$, respectively, as follows.

$$[H_O^\bullet] = K_5 [h^\bullet]^{-1} [V_O^{\bullet\bullet}] p_{H2}^{0.5} \quad (4\text{-}7)$$

$$[H_i'] = K_6 [h^\bullet]^{-1} p_{H2}^{0.5} \quad (4\text{-}8)$$

K_5 and K_6 are equilibrium constants of reaction (4-5) and (4-6), respectively. δ_H of H-BZI at 800°C in 100 kPa p_{H2} is about 0.045, which is larger than the value (0.003) at 700°C in 100 Pa by about 0.04. This gap is close to the decline of $H_O^\bullet$ defects with dehydrogenation of D-BZI to deD-BZI by heating in 0.1%-H_2/Ar at 700°C (Table 4-1), indicating that the adsorption/desorption is conducted only by uptake/loss of H^- lattice anion ($H_O^\bullet$ defect) with remaining interstitial H^- ion (H_i' defect) unchanged. These features prove that H-BZI conducts reversible H_2 absorption/desorption via association of oxygen vacancy and H_2 molecules (Equation (4-4)), assisted by bulk diffusion of $H_O^\bullet$ defects.

In p_{H2} equaling 100 kPa, δ_H is rather constant in $T \geq 600$°C whereas it remarkably increases with decreasing temperature in $T \leq 500$°C (Figure 4-7b). T is temperature. This feature reveals $[H_O^\bullet]$ is almost constant in $T \geq 600$°C whereas it increases with temperature in $T \leq 500$°C at fixed p_{H2} of 100 kPa.

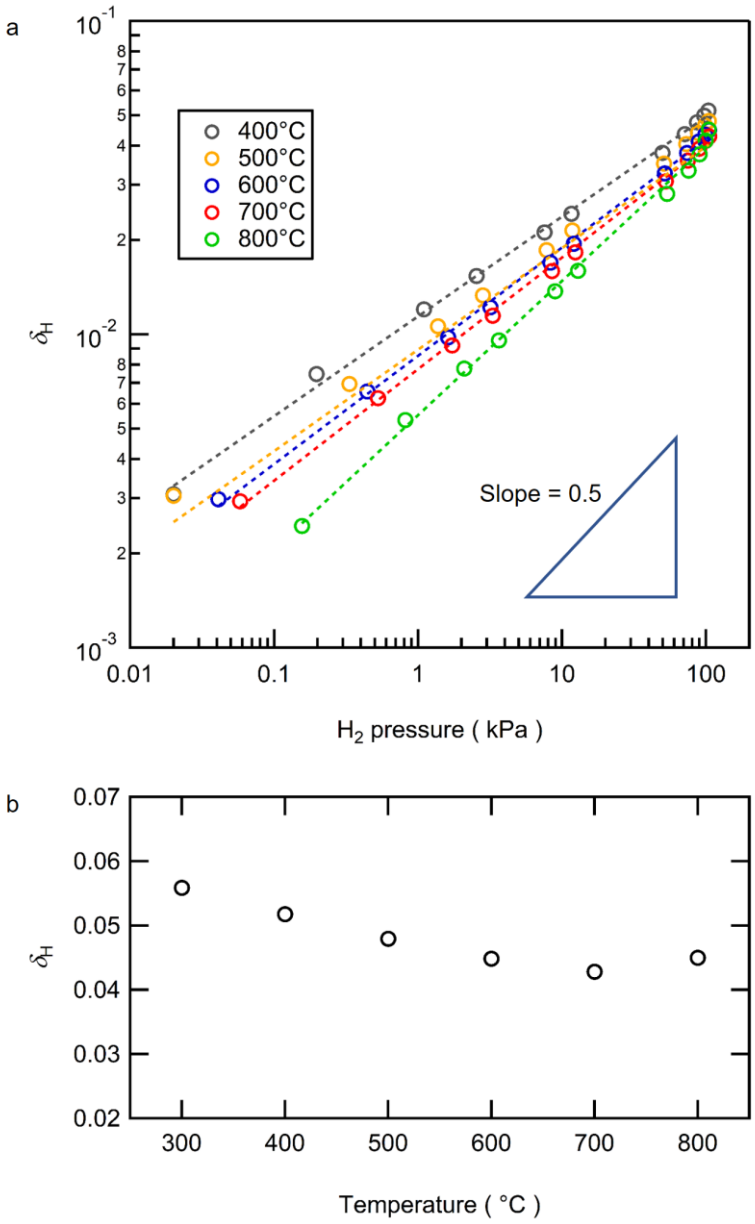

Figure 4-7. The pressure-composition-temperature (PCT) curves. (a) Log-log plots of δ_H vs p_{H2}. (b) δ_H at each temperature in 100kPa.

4.3.3. Hydrogen permeation by hydride-ion transport

The electrical conductivity (σ) of an H-BZI sintered bar (relative density, > 95%; ϕ4 mm × 10 mm) was measured by the four-probe DC method in a dry H_2 atmosphere (dew-point < −70°C). The BZI sintered discs (ϕ10 mm × 1 mm) could be successfully converted into H-BZI discs while maintaining their dense matrices by H_2 hydrogenation at 800°C for 3 days without the use of H^- reagents (Figure 4-8a–d). The interior of the disc is completely blackened, and their average grain sizes remains unchanged at approximately 5 μm (Figure 4-8e and f). ND Rietveld refinement of the pulverized discs also confirms that the hydrogenated sinters have oxygen defects and hydrogen concentrations similar to those of the H-BZI powder. Low lattice contraction (–0.07%) following hydrogenation allowed topotactic bulk transformation.

Pristine BZI is a poor proton conductor with an activation energy of 65 kJ mol^{-1} in wet Ar, in agreement with previous reports [24]. However, H-BZI exhibits highly conductive semiconductor behavior in a dry H_2 atmosphere (Figure 4-8g). In this study, σ shows low temperature dependence at 100°C ≤ T ≤ 400°C and is generally maintained at approximately 10^{-2} S cm^{-1} over this range. σ then increases at T > 400°C. The hydrogen concentration cells described below give a much smaller open circuit voltage than the Nernstian theoretical value at T > 400°C, confirming that H-BZI is a mixed ion electron conductor with a relatively small ion transfer number. $\log\sigma$ is proportional to $T^{-1/4}$, which indicates that variable-range electron-hopping [37] occurs in H-BZI.

The activation energy for electron hopping (E_{eh}) decreases from 0.31 to 0.1 eV with decreasing T to below 400°C, indicating the variation of carrier concentration or mobility at the temperature. When [H_i'] is as assumed to constant as confirmed by PCT and ND measurements, combing Equation (4-4) and (4-5) gives [$h^\bullet$] as follows.

$$[h^\bullet] = [H_O^\bullet]\,[O_O^\times]^{-1}\,p_{H2O}\,p_{H2}^{-3/2}\,K_4^{-1}\,K_5^{-1} \qquad (4\text{-}9)$$

p_{H2O}. K_4^{-1} and K_5^{-1} are a water partial pressure and equilibrium constant of reaction (4-4) and (4-5), respectively. Hence [$h^\bullet$] is in proportion to [$H_O^\bullet$], if p_{H2O}, [$O_O^\times$] and p_{H2} is assumed to constant. This is consistent with the experimental conditions, because p_{H2O} is kept at very low and thus defect reaction

(4-4) is largely shifted to the left side. [h•] is speculated to increase with decreasing T to below 500 °C, based on the PCT and ND results that [H_O•] tends to increase with decreasing T to below 500 °C (Figure 4-7b). Therefore, the relatively low E_{eh} in $T \leq 400$ °C attributes to the increase of [h•]. The aforementioned results reveal that H-BZI exhibits hopping transport of holes, which is consistent with the valence state of In atoms (+2.08) allowing hole hopping between In(II) to In(III).

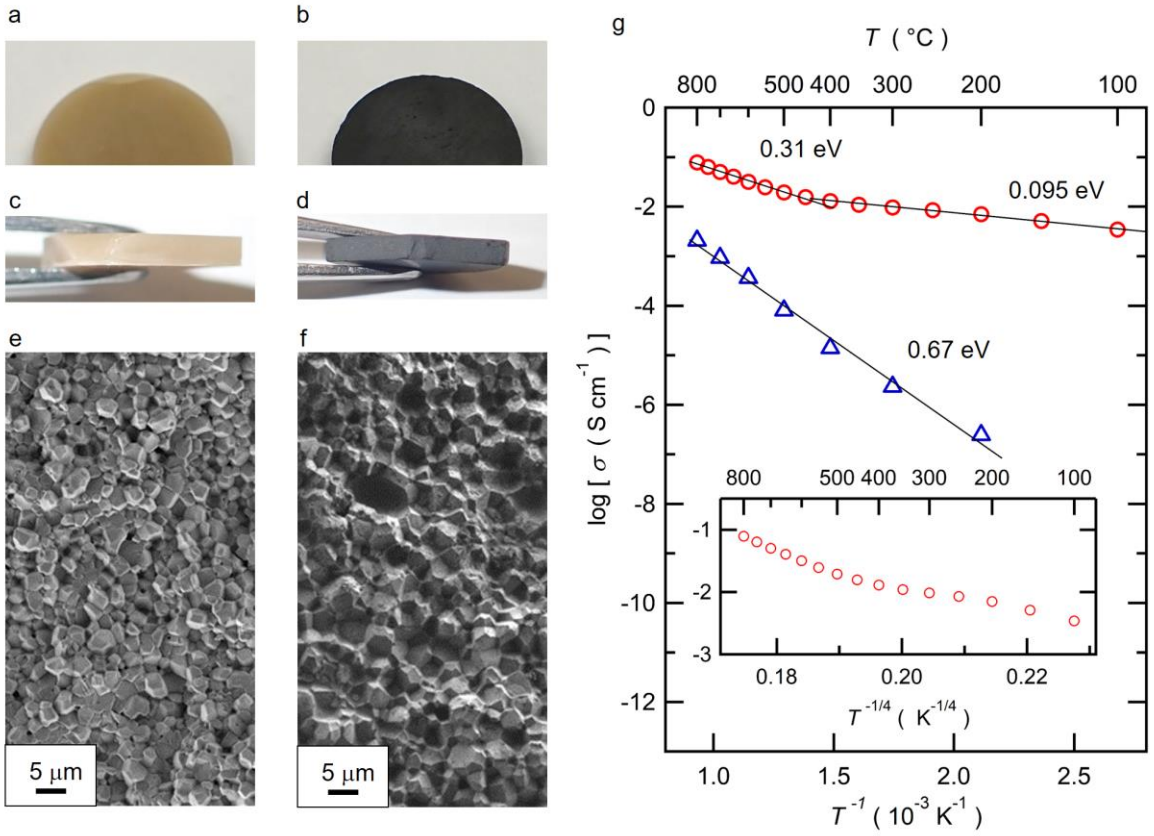

Figure 4-8. Electrical conductivity of H-BZI sinters. (a, b) Surface and (c, d) cross-sectional images of the (a, c) BZI and (b, d) H-BZI sintered discs. The latter was prepared by the hydrogenation of pristine BZI sintered discs at 800 °C for 3 days in H_2. Cross-sectional SEM images of (e) BZI and (f) H-BZI sintered discs. (g) Electrical conductivity (σ) of BZI (blue triangle) and H-BZI (red circle) sintered bars, measured in wet Ar and dry H_2 , respectively by 4 probe DC tex. Inset: Plots of $\log\sigma$ vs. $T^{-1/4}$ for H-BZI.

Electrochemical H_2 pumping measurements prove that the hydrogen permeability of H-BZI is due to H^- ion conduction. Concentration cells of {30%-H_2/Ar, Pd(1) | H-BZI | Pd(2), H_2} were constructed from the dense H-BZI sintered discs (ϕ12 mm × 0.8 mm), and the exhaust gases on the Pd(1) side were analyzed by DC polarization. Relatively high p_{H2} gases were fed to the low H_2 concentration side to prevent the oxidation of H-BZI. H-BZI achieves a constant current of approximately +/−0.5 A cm^{-2}, and the H_2 concentration (C_H) logarithmically increases/decreases but stabilizes within 30 min at 800°C when a bias of +/−5 V is applied to Pd(1) at t = 0 (Figure 4-9a). The positive and negative biases on Pd(1) increase and decrease, respectively, the hydrogen flux in the H-BZI bulk, which proves that H-BZI exhibits hydrogen permeance via the conduction of negatively charged hydrogen species (i.e., H^- ions). The partial H^- ion conductivity (σ_H) at 800°C, which is roughly calculated from the increase in hydrogen flux with an applied bias of +5 V, is 1.2 × 10^{-3} S cm^{-1}, which is similar to the total conductivity of the well-known proton-conducting $BaZr_{0.8}Y_{0.2}O_3$ ceramic [38]. The transfer number of H^- ions is estimated to be 0.12 by comparing the hydrogen flux and DC current. Unfortunately, hydrogen pumping does not occur well at low temperatures because of the small change in C_H in comparison with that of the feed gas (30%). These results verify that the hydrogen permeability of H-BZI is due to its mixed ion electron conductivity.

Membrane devices with 10 μm-thick dense H-BZI films can be fabricated via the conventional processes used for solid oxide fuel cells because the dense matrices of BZI are retained following hydrogenation on account of its low lattice deformation (Figures 6c−6e). A NiO/BZI composite disc (ϕ12 mm) coated with BZI film (10 μm) was fabricated by the ceramic cofiring process [39]. The BZI and NiO components were converted to H-BZI and Ni, respectively, by H_2 heating at 800°C for 8 h, as confirmed by XRD measurements. Hence, the membrane device comprises a dense H-BZI film over a porous Ni-(H-BZI) cermet support, which are typical form of the fuel electrodes in ceramics electrochemical cells and membrane reactors (Figure 4-9c−e). Concentration cells of {10%-H_2/Ar | H-BZI | Ni-(H-BZI) cermet, 100 or 80%-H_2/N_2} yield a large H_2 flux (J_{H2}) without N_2 gas leakage (Figure 4-9b and Figure 4-10), which confirms their hydrogen permeability due to ambipolar diffusion of H^-

ion and electron. The permeance of H-BZI exhibits a complex temperature dependence. J_{H2} decreases with decreasing temperature in the range of 700–600°C, remains unchanged in the range of 600−500°C, and decreases once more at $T < 500$°C. This characteristic is attributed to differences in the temperature dependence of the diffusivity and concentration of H^- ions: specifically, the former increases whereas the latter decreases with increasing temperature (see Figure 4-7b).

The permeance of the H-BZI membrane is higher than those of proton-conducting ceramic membranes with a thickness of a few tens of micrometers [16-19] at $T < 700$°C and equal to 0.18 and 0.20 mL cm^{-2} min^{-1} (67 and 75 μmol cm^{-2} s^{-1}, respectively) at 500°C under H_2 feeds of 80% and 100%, respectively (Figure 4-9b). The corresponding H^- ion conductivity is estimated as 4×10^{-4} S cm^{-1} by using a flux-conductivity relationship [40], notably, this conductivity is one order of magnitude higher than the highest value obtained for protonic $BaCeO_3$ base films [17]. Moreover, this conductivity value satisfies the requirements for the mixed conducting electrodes of ceramic cells ($> 10^{-4}$ S cm^{-1}) [41]. The H-BZI membrane exhibits remarkable permeance corresponding to a H^- ion conductivity of 10^{-4} S cm^{-1} even at 400°C. These results unequivocally demonstrate that mixed H^- ion–electron-conducting BZI possesses better hydrogen permeability than proton-conducting ceramics at relatively low temperatures.

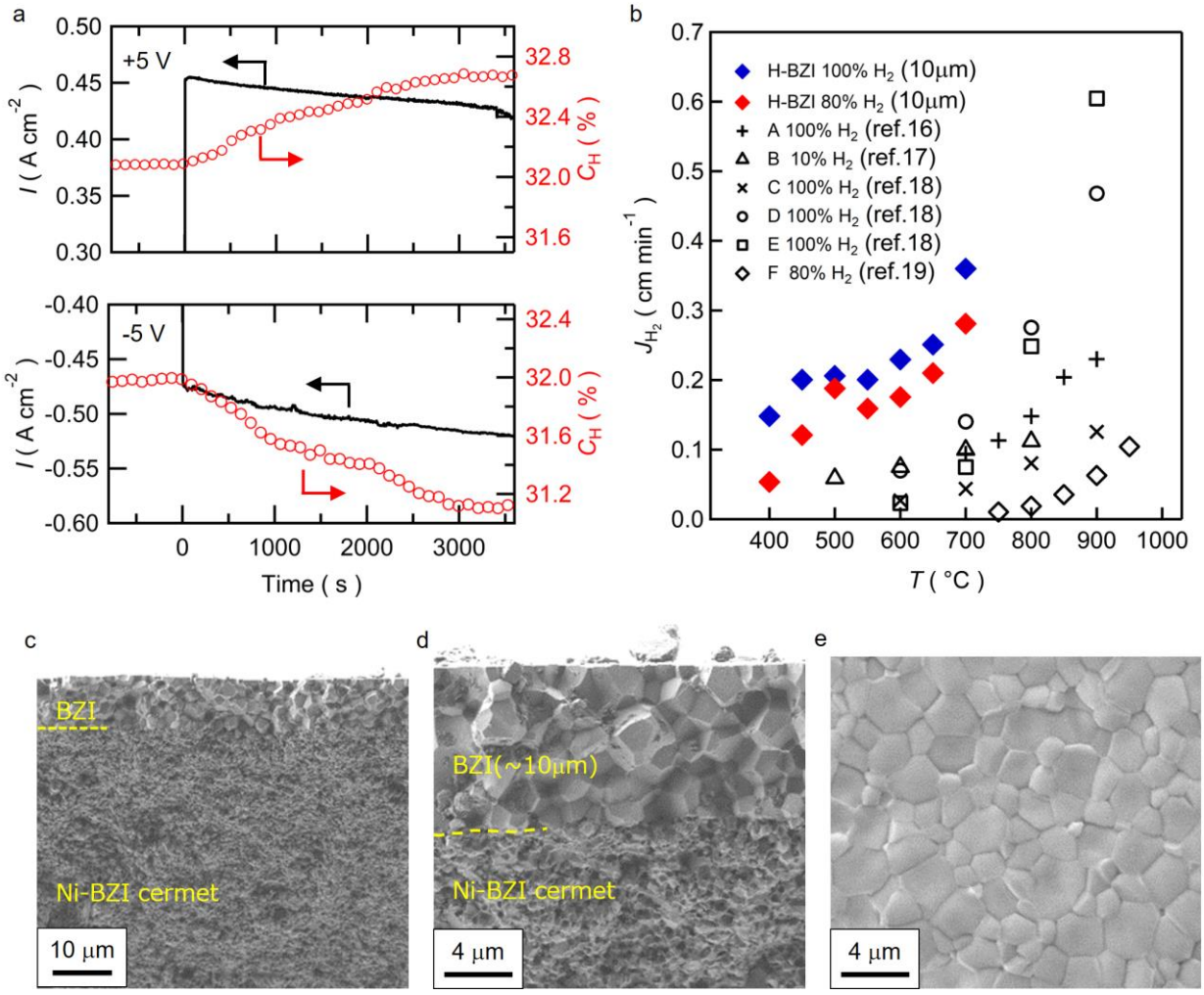

Figure 4-9. Hydrogen permeability due to the mixed conductivity of H^- electrons. (a, b) H_2 pumping of concentration cells of {10%-H_2/ Ar, Pd(1) | H-BZI | Pd(2), H_2} constructed with H-BZI sintered discs at 800 °C. The cell was kept at the open circuit voltage for $t < 0$, and a bias of +/−5 V was applied at $t = 0$. (b) H_2 permeance of thin-film devices bearing {10%-H_2/ Ar | H-BZI (10 μm)/Ni-BZI | y%-H_2/N_2 (y = 80 and 100)}. Blue and red symbols indicate the permeance of H-BZI in y = 100 and 80, respectively. White symbols the permeance of (BS)ZCM base membranes cited from references [16-19]. (c, d) Cross-sectional and (e) surface scanning electron microscopy images of the thin-film device used for permeation measurements. In (b), the reference materials are as follows: A. $SrCe_{0.7}Zr_{0.2}Eu_{0.1}O_{3-\delta}$ _Ni-SCZ82(33 μm) [16], B. $BaCe_{0.9}Y_{0.1}O_{3-\delta}$_porrous$ZrO_2$ (10 μm) [17], C. $SrCe_{0.9}Eu_{0.1}O_{3-\delta}$_Ni-$SrCeO_3$ (30 μm) [18], D. $SrCe_{0.85}Eu_{0.15}O_{3-\delta}$_Ni-$SrCeO_3$ (30 μm) [18], E. $SrCe_{0.8}Eu_{0.2}O_{3-\delta}$_Ni-$SrCeO_3$ (30 μm) [18], F. $SrCe_{0.95}Y_{0.05}O_{3-\delta}$(SCY)_Ni-SCY (50 μm) [19].

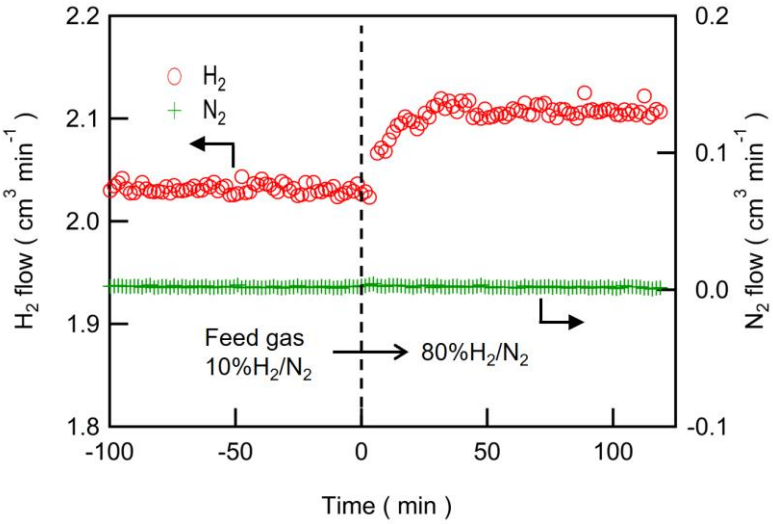

Figure 4-10. Flow rate changes of H_2 and N_2 in permeation test

4.4. Discussion

The preceding results demonstrate that $BaZr_{0.5}In(III)_{0.5}O_{2.75}$ is reductively transformed to $BaZr_{0.5}In(II)_{0.5}O_{2.25}H_{0.5}$ (H-BZI) by H_2 annealing at elevated temperature. H^- ions are introduced to oxygen site ($H_O^\bullet$ defects) and interstitial site near [100] face center (H_i' defects). The resultant H-BZI exhibits remarkable hydrogen permeation due to the ambipolar diffusion of $H_O^\bullet$ defect type H^- ion and electron hole. The membrane permeability is higher than those of H^+-conducting (BS)ZCM-Ni cermet in a wide temperature range, which attributes to the relatively high surface exchange kinetics and bulk diffusivity of H-BZI. H-BZI must have large active surface for the dissociative adsorption of hydrogen than the protonic (BS)ZCM-Ni cermets, because hydrogen incorporation can occur over all surfaces of H-BZI membrane while that occurs only at Ni-(BS)ZCM-gas triple phase boundary in case of cermet

membranes owing to the poor electron conductivity in (BS)ZCM. Hence the former could exhibit relatively high surface exchange kinetics.

Moreover, the structural analysis confirms that the defect structures of H-BZI is suitable for hopping of $H_O^{\bullet}$ defects. Combined ND and PCT results (Table 4-1 and Figure 4-7a) prove that $H_O^{\bullet}$ defects dominantly contribute to H^- ion diffusion for the hydrogen permeation. Given the simple hopping mechanism of $H_O^{\bullet}$ defect type H^- ions via thermally activated jumping from one anion site to the nearest neighboring (NN) vacant sites, the fast diffusion of $H_O^{\bullet}$ defects must require the percolation of oxygen vacancies along the NN sites (Figure 4-11a) [15]. Since each anion in H-BZI has eight NN anion sites, anion sites must be at least 25% occupied (randomly) by H^- ions or vacancies to achieve a 3-dimensional percolation of $V_O^{\bullet\bullet}$ and $H_O^{\bullet}$ defects along NN sites [15]. This requirement gives rise to a sum of $[V_O^{\bullet\bullet}]$ and $[H_O^{\bullet}]$ of ≥ 0.75 [15], which is close to the corresponding value of H-BZI (0.72).

The accounts for the local coordination environments provide more clear verification for the percolation of $V_O^{\bullet\bullet}$ and $H_O^{\bullet}$ defect sites along NN path. The radial distribution function analysis indicates that the length of the In–O scattering path, at ~1.65 Å, remarkably decreases whereas that of the Zr–O scattering path, at ~1.6 Å, remains unchanged by hydrogenation, as shown in Figure 4-5c and d. This result reveals that O atoms shared by two InO_6 octahedra (referred to as In–O–In) are preferably vacant or submitted by H atoms whereas O atoms bridging two ZrO_6 or a pair of InO_6 and ZrO_6 octahedra (referred to as Zr–O–Zr and In–O–Zr, respectively) are retained even after hydrogenation. This finding is in agreement with the theoretical calculation that O vacancies favorably form in In–O–In sites in $BaZr_{0.8}In_{0.2}O_{3-\delta}$ perovskites [42]. Every O atom is coordinated by a pair of the B site cations in ideal cubic perovskite ABO_3. Therefore, 25% of the O sites is assigned to In–O–In sites in $BaZr_{0.5}In_{0.5}O_3$, because the probability for the coordinated by two In atoms is given by 0.5 × 0.5 if Zr and In atoms randomly occupy the B sites. Based on the EXAFS and ND analysis, all In–O–In sites are assigned to anion vacancy or H^- ion defect. Recalling bond percolation in simple cubic sublattice of B-site cations, the population of In–O–In bonds (0.25) is beyond the threshold (0.2488) [43].

The activation energy of hydrogen permeation (E_H) in H-BZI is approximately determined to 0.25 eV from the slope in $T \geq 550$°C. This value is very close to the energies calculated for H^- ion jump along NN sites (0.2 eV) in $SrTiO_{1-x}H_x$ [44]. On the other hand, the E_H value is much smaller than the activation energy for H^- diffusion in $BaTiO_{1-x}H_x$ ($x \leq 0.6$), which was deduced from the kinetics of H/D exchange reactions [15]. Tang et al reported that the H^- diffusion in $BaTiO_{1-x}H_x$ requires hopping along the second nearest neighbor (2NN) sites because the relatively low concentration of anion vacancy does not allow the percolation in NN path (Figure 4-11a and b) [15]. A bottleneck energy of 2NN hopping is about 200 kJ mol^{-1}, so that $BaTiO_{1-x}H_x$ ($x \leq 0.6$) show slow diffusion of H^- ions. Based on these, the current results unambiguously demonstrate that H-BZI involves bulk conduction of H^- ion by the NN hopping of $Ho^{\bullet}$ defects through the percolation network of In–O–In vacancy sites (Figure 4-11c).

The small change of [Hi′] after H_2 desorption confirms the less-pronounced diffusion of Hi′ defects. This is rather consistent with the previous reports, in which Hi′ defects have large bottleneck energy for the jump to NN vacant site as calculated by DFT [44]. (100) plane of ideal perovskite consists of four B site cations locating the corners and four anions bridging two B site cations (Figure 4-11d). Some of (100) face of H–BZI consist of three or four In atoms, so that two or all O^{2-} ions are missing or substituted by H^- ions. H_i' defects must be favorably incorporated to the center sites of such In-rich (100) plane to reduce the coulombic repulsions in cation excess conditions. The probability for the (100) plane including three and four In atoms is 0.25 and 0.0625, respectively, under the random distribution of Zr and In atoms, and this value is close to [H_i'] of H-BZI (0.19). H_i' defects have not been formed in perovskite oxyhydride such as $BaTiO_{2.4}H_{0.6}$ [12] and $SrTiO_{2.55}H_{0.45}$ [45], probably because these have much smaller anion deficiency than H-BZI.

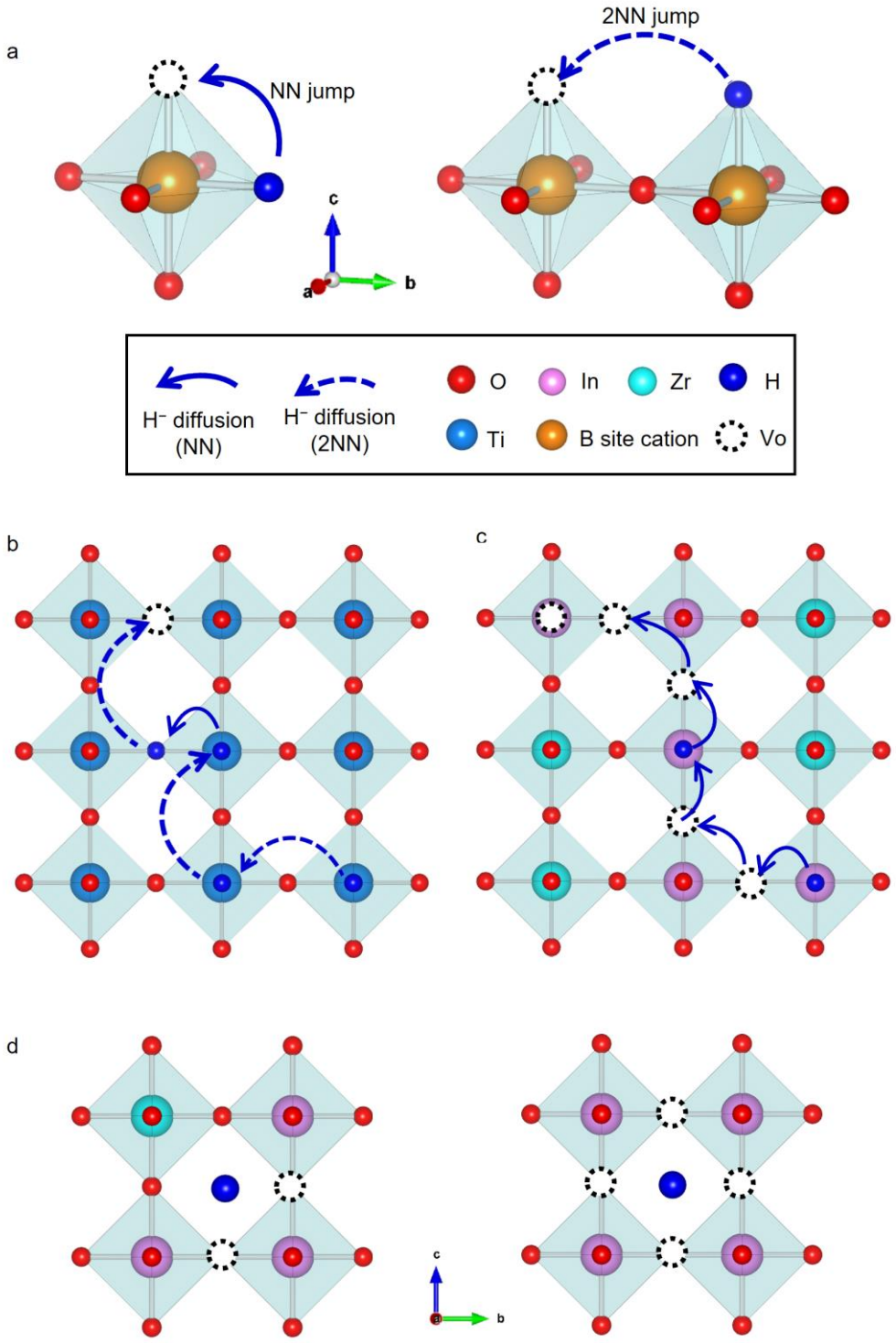

Figure 4-11. (a) Hydride migration along NN (blue, solid line) and 2NN (blue, dotted line) jump in cubic perovskite oxyhydride. (b) Possible hydride diffusion pathway in $BaTiO_{3-x}H_x$ including 2NN hydride hopping. (c) Possible hydride diffusion pathway in H-BZI by NN hydride hopping. (d) H_i' defects incorporated to the center sites of In-rich (100) plane including three (left) and four (right) In atoms.

4.5. Conclusion

The cubic perovskite BZI was demonstrated to undergo topotactic transformation to H-BZI by H_2 annealing at 800°C with the reduction of In(III) to In(II) and the incorporation of H^- ions into oxygen vacancies sites ($H_O^\bullet$ defect) and interstitial sies (H_i' defect) near [100] face centers (3c sites). Because the lattice contraction is only 0.07% regardless of the number of O vacancies and H^- ion defects formed, BZI sintered bodies (relative density, > 95%) can be converted to oxyhydrides while retaining their dense matrix. Hence, membrane devices comprising dense H-BZI films resting on porous Ni-cermet supports can be fabricated by the hydrogenation of an isomorphous BZI device without deformation. The H-BZI film exhibited a hydrogen permeance of 0.20 mL cm^{-2} min^{-1} at 500°C with a H^- ion conductivity of 4×10^{-4} S cm^{-1}, which is one order of magnitude higher than that obtained from protonic ceramic separation films. O vacancies and H^- ion defects favored localization on O sites bridging two In atoms (In–O–In sites), and thus the percolation of these vacancies and defects occurs because of the relatively large oxygen deficiency (0.72). The structural features allowed the bulk diffusion of $H_O^\bullet$ defect type H^- ions via consecutive hopping along NN path. Coupled with the large polarizability of H^- ion in comparison to H^+, thus H-BZI can exhibited fast bulk diffusion of H^- ion, and thus, achieved superior permeability than protonic (BS)ZCM-Ni cermet membranes. Given their superior H^- ion conductivity and ease of manufacturing, the current materials exhibit great potential for application in the mixed conducting electrodes of ceramic electrolysis cells and membrane reactors used to execute processes such as ammonia synthesis, CO_2 hydrogenation, and methane utilization. The current results provide a strong tool for electrochemical and catalytic conversion systems.

4.6. References

1. Fukui, K., Iimura, S., Tada, T., Fujitsu, S., Sasase, M., Tamatsukuri, H., *et al*. Characteristic fast H^- ion conduction in oxygen-substituted lanthanum hydride. *Nature Communications*, *10*, 2578 (2019).
2. Ubukata, H., Broux, T., Takeiri, F., Shitara, K., Yamashita, H., Kuwabara, A., *et al*. Hydride conductivity in an anion-ordered fluorite structure LnHO with an enlarged bottleneck. *Chemistry of Materials*, *31*(18), 7360-7366 (2019).
3. Kobayashi, G., Hinuma, Y., Matsuoka, S., Watanabe, A., Iqbal, M., Hirayama, M., *et al*. Pure H^- Conduction in Oxyhydrides. *Science*, *351*(6279), 1314-1317 (2016).
4. Takeiri, F., Watanabe, A., Kuwabara, A., Nawaz, H., Ayu, N. I. P., Yonemura, M., *et al*. Ba_2ScHO_3: H^- Conductive Layered Oxyhydride with H^- Site Selectivity. *Inorganic chemistry*, *58*(7), 4431-4436 (2019).
5. Nawaz, H., Takeiri, F., Kuwabara, A., Yonemura, M., & Kobayashi, G. Synthesis and H^- conductivity of a new oxyhydride Ba_2YHO_3 with anion-ordered rock-salt layers. *Chemical Communications*, *56*(71), 10373-10376 (2020).
6. Kobayashi, Y., Tang, Y., Kageyama, T., Yamashita, H., Masuda, N., Hosokawa, S., & Kageyama, H. Titanium-based hydrides as heterogeneous catalysts for ammonia synthesis. *Journal of the American Chemical Society*, *139*(50), 18240-18246 (2017).
7. Tang, Y., Kobayashi, Y., Masuda, N., Uchida, Y., Okamoto, H., Kageyama, T., *et al*. Metal-Dependent Support Effects of Oxyhydride-Supported Ru, Fe, Co Catalysts for Ammonia Synthesis. *Advanced Energy Materials*, *8*(36), 1801772 (2018).
8. Tang, Y., Kobayashi, Y., Tassel, C., Yamamoto, T., & Kageyama, H. Hydride-Enhanced CO_2 Methanation: Water-Stable $BaTiO_{2.4}H_{0.6}$ as a New Support. *Advanced Energy Materials*, *8*(23), 1800800 (2018).
9. Steinsvik, S., Larring, Y., & Norby, T. Hydrogen Ion Conduction in Iron-Substituted Strontium Titanate, $SrTi_{1-x}Fe_xO_{3-x/2}$ ($0 \leq x \leq 0.8$). *Solid State Ionics*, *143*(1), 103-116 (2001).
10. Poulsen, F. W. Speculations on the existence of hydride ions in proton conducting oxides. *Solid State Ionics*, *145*(1-4), 387-397 (2001).
11. STEINSVIK, S., BUGGE, R., GjØNnes, J. O. N., TAFTØ, J., & Norby, T. The Defect Structure of $SrTi_{1-x}FexO_{3-y}$ (x = 0–0.8) Investigated by Electrical Conductivity Measurements and Electron Energy Loss Spectroscopy (EELS). *Journal of Physics and Chemistry of Solids*, *58*(6), 969-976 (1997).
12. Kobayashi, Y., Hernandez, O. J., Sakaguchi, T., Yajima, T., Roisnel, T., Tsujimoto, Y., *et al*. An

oxyhydride of $BaTiO_3$ exhibiting hydride exchange and electronic conductivity. *Nature Materials*, *11*(6), 507-511 (2012).

13. Uchimura, T., Takeiri, F., Okamoto, K., Saito, T., Kamiyama, T., & Kobayashi, G. (2021). Direct synthesis of barium titanium oxyhydride for use as a hydrogen permeable electrode. *Journal of Materials Chemistry A*, *9*(36), 20371-20374.
14. Takeiri, F., Watanabe, A., Okamoto, K., Bresser, D., Lyonnard, S., Frick, B., *et al*. Hydride-ion-conducting K2NiF4-type Ba–Li oxyhydride solid electrolyte. *Nature Materials*, *21*(3), 325-330 (2022).
15. Tang, Y., Kobayashi, Y., Shitara, K., Konishi, A., Kuwabara, A., Nakashima, T., *et al*. On hydride diffusion in transition metal perovskite oxyhydrides investigated via deuterium exchange. *Chemistry of Materials*, *29*(19), 8187-8194 (2017).
16. Li, J., Yoon, H., & Wachsman, E. D. Hydrogen permeation through thin supported $SrCe_{0.7}Zr_{0.2}Eu_{0.1}O_{3-\delta}$ membranes; dependence of flux on defect equilibria and operating conditions. *Journal of Membrane Science*, *381*(1-2), 126-131 (2011).
17. Kim, J. H., Kang, Y. M., Kim, B. G., Lee, S. H., & Hwang, K. T. Preparation of dense composite membrane with Ba-cerate conducting oxide and rapidly solidified Zr-based alloy. *International Journal of Hydrogen Energy*, *36*(16), 10129-10135 (2011).
18. Oh, T. K., Yoon, H., & Wachsman, E. D. Effect of Eu dopant concentration in $SrCe_{1-x}Eu_xO_{3-\delta}$ on ambipolar conductivity. *Solid State Ionics*, *180*(23-25), 1233-1239 (2009).
19. Zhan, S., Zhu, X., Ji, B., Wang, W., Zhang, X., Wang, J., *et al*. Preparation and hydrogen permeation of $SrCe_{0.95}Y_{0.05}O_{3-\delta}$ asymmetrical membranes. *Journal of Membrane Science*, *340*(1-2), 241-248 (2009).
20. Oishi, R., Yonemura, M., Nishimaki, Y., Torii, S., Hoshikawa, A., Ishigaki, T., *et al*. Rietveld analysis software for J-PARC. *Nuclear Instruments and Methods in Physics Research Section A: Accelerators, Spectrometers, Detectors and Associated Equipment*, *600*(1), 94-96 (2009).
21. Oishi-Tomiyasu, R., Yonemura, M., Morishima, T., Hoshikawa, A., Torii, S., Ishigaki, T., & Kamiyama, T. Application of matrix decomposition algorithms for singular matrices to the Pawley method in Z-Rietveld. *Journal of Applied Crystallography*, *45*(2), 299-308 (2012).
22. Ahmed, I., Knee, C. S., Karlsson, M., Eriksson, S. G., Henry, P. F., Matic, A., Engberg, D., & Börjesson, L. Location of Deuteron Sites in the Proton Conducting Perovskite $BaZr_{0.50}In_{0.50}O_{3-Y}$. *Journal of Alloys and Compounds*, *450*(1-2), 103-110 (2008).
23. Ahmed, I., Kinyanjui, F. G., Steegstra, P., Shen, Z. J., Eriksson, S. G., & Nygren, M. Improved proton conductivity in spark-plasma sintered dense ceramic $BaZr_{0.5}In_{0.5}O_{3-\delta}$. *Electrochemical and*

Solid-State Letters, *13*(11), B130 (2010).

24. Ahmed, I., Eriksson, S. G., Ahlberg, E., & Knee, C. S. Influence of Microstructure on Electrical Properties in $BaZr_{0.5}In_{0.5}O_{3-\delta}$ Proton Conductor. *Solid State Ionics*, *179*(21-26), 1155-1160 (2008).
25. Ahmed, I., Eriksson, S. G., Ahlberg, E., Knee, C. S., Berastegui, P., Johansson, L. G., Rundlöf, H., Karlsson, M., Matic, A., Börjesson, L. & Engberg, D. Synthesis and Structural Characterization of Perovskite Type Proton Conducting $BaZr_{1-x}In_xO_{3-\delta}$ ($0 \leq x \leq 0.75$). *Solid State Ionics*, *177*(17-18), 1395-1403 (2006).
26. Kinyanjui, F. G., Norberg, S. T., Ahmed, I., Eriksson, S. G., & Hull, S. In-situ conductivity and hydration studies of proton conductors using neutron powder diffraction. *Solid State Ionics*, 225, 312-316 (2012).
27. Mazzei, L., Wolff, M., Pergolesi, D., Dura, J. A., Börjesson, L., Gutfreund, P., Bettinelli, M., Lippert, T., & Karlsson, M. Structure and Conductivity of Epitaxial Thin Films of In-Doped $BaZrO_3$-Based Proton Conductors. *The Journal of Physical Chemistry C*, *120*(50), 28415-28422 (2016).
28. Manthiram, A., Kuo, J. F., & Goodenough, J. B. Characterization of oxygen-deficient perovskites as oxide-ion electrolytes. *Solid State Ionics*, 62(3-4), 225-234 (1993).
29. Lang, P. F., & Smith, B. C. Ionic radii for Group 1 and Group 2 halide, hydride, fluoride, oxide, sulfide, selenide and telluride crystals. *Dalton Transactions*, *39*(33), 7786-7791 (2010).
30. Maekawa, H., Kashii, N., Kawamura, J. I., Hinatsu, Y., & Yamamura, T. High Temperature ^1H NMR Study of Proton Conducting Oxide $SrCe_{0.95}Y_{0.05}H_{0.004}O_{3-\delta}$. *Solid State Ionics*, *122*(1-4), 231-236 (1999).
31. Verbraeken, M. C., Viana, H. A., Wormald, P., & Irvine, J. T. A structural study of the proton conducting B-site ordered perovskite $Ba_3Ca_{1.18}Ta_{1.82}O_{8.73}$. *Journal of Physics: Condensed Matter*, *23*(23), 234111 (2011).
32. Hayashi, K. Heavy Doping of H^- ion in $12CaO{\cdot}7Al_2O_3$. *Journal of Solid State Chemistry*, *184*(6), 1428-1432 (2011).
33. Shima, T., Luo, Y., Stewart, T., Bau, R., McIntyre, G. J., Mason, S. A., & Hou, Z. Molecular heterometallic hydride clusters composed of rare-earth and d-transition metals. *Nature Chemistry*, *3*(10), 814-820 (2011).
34. Björketun, M. E., Sundell, P. G., & Wahnström, G. Structure and thermodynamic stability of hydrogen interstitials in $BaZrO_3$ perovskite oxide from density functional calculations. *Faraday Discussions*, *134*, 247-265 (2007).
35. Henderson, C. M. B., Charnock, J. M., Smith, J. V., & Greaves, G. N. X-ray absorption

spectroscopy of Fe, Mn, Zn, and Ti structural environments in staurolite. *American Mineralogist*, *78*(5-6), 477-485 (1993).

36. Farges, F. *Ab initio* and experimental pre-edge investigations of the Mn *K*-edge XANES in oxide-type materials. *Physical Review B*, *71*(15), 155109 (2005).
37. Mott, N. F. Conduction in non-crystalline materials: III. Localized states in a pseudogap and near extremities of conduction and valence bands. *Philosophical Magazine*, *19*(160), 835-852 (1969).
38. Tong, J., Clark, D., Hoban, M., & O'Hayre, R. Cost-effective solid-state reactive sintering method for high conductivity proton conducting yttrium-doped barium zirconium ceramics. *Solid State Ionics*, *181*(11-12), 496-503 (2010).
39. An, H., Lee, H. W., Kim, B. K., Son, J. W., Yoon, K. J., Kim, H., Shin, D., Ji, H. I., & Lee, J. H. 5 × 5 cm^2 Protonic Ceramic Fuel Cell With a Power Density of 1.3 W cm^{-2} at 600°C. *Nature Energy*, *3*(10), 870-875 (2018).
40. Norby, T., & Larring, Y. Mixed hydrogen ion–electronic conductors for hydrogen permeable membranes. *Solid State Ionics*, *136*, 139-148 (2000).
41. Lei, C., Simpson, M. F., & Virkar, A. V. Investigation of Ion and Electron Conduction in the Mixed Ionic-Electronic Conductor-La-Sr-Co-Fe-Oxide (LSCF) Using Alternating Current (AC) and Direct Current (DC) Techniques. *Journal of The Electrochemical Society*, *169*(1), 014506 (2022).
42. Takahashi, H., Yashima, I., Amezawa, K., Eguchi, K., Matsumoto, H., Takamura, H., & Yamaguchi, S. First-Principles Calculations for the Energetics of the Hydration Reaction of Acceptor-Doped $BaZrO_3$. *Chemistry of Materials*, *29*(4), 1518-1526 (2017).
43. Frisch, H. L., & Hammersley, J. M. Percolation processes and related topics. *Journal of the Society for Industrial and Applied Mathematics*, *11*(4), 894-918 (1963).
44. Liu, X., Bjørheim, T. S., Vines, L., Fjellvåg, Ø. S., Granerød, C., Prytz, Ø., Yamamoto, T., Kageyama, H., Norby, T., & Haugsrud, R. Highly Correlated Hydride Ion Tracer Diffusion in $SrTiO_{3-x}H_x$ Oxyhydrides. *Journal of the American Chemical Society*, *141*(11), 4653-4659 (2019).
45. Bouilly, G., Yajima, T., Terashima, T., Yoshimune, W., Nakano, K., Tassel, C., Kususe, Y., Fujita, K., Tanaka, K., Yamamoto, T., Kobayashi, Y., & Kageyama, H. Electrical properties of epitaxial thin films of oxyhydrides $ATiO_{3-x}H_x$ (A = Ba and Sr). *Chemistry of Materials*, *27*(18), 6354-6359 (2015).

Chapter 5

H-SOEC using $BaZr_{0.5}In_{0.5}O_{2.25}H_{0.5}$ oxyhydride cathodes

5.1. Objective of chapter 5

Cubic perovskite $BaZr_{0.5}In_{0.5}O_{2.25}H_{0.5}$ (H-BZI) oxyhydride exhibited excellent hydrogen permeability according to ambipolar diffusion hydride ion electron mixed conductivity, as described in chapter 4. Therefore, H-BZI is attractive candidate for the hydrogen permeable membrane cathodes of H-SOECs. In this chapter, steam electrolysis was performed using H-BZI cathode. I developed the H-SOECs comprising Ni-BZI or Ni-(H-BZI) cermet cathode, BZI electrolyte film, $Ba_{0.95}La_{0.05}Fe_{0.8}Zn_{0.2}O_{3-\delta}$ (BLFZ) AFL and $PrBa_{0.5}Sr_{0.5}Co_{1.5}Fe_{0.5}O_{5+\delta}$ (PBSCF) anode. The H-SOECs with Ni-BZI cathode (denoted as the cell with H^+-cathode) were evaluated by feeding wet H_2 gases to the cathode side for pre-reduction and steam electrolysis. On the other hand, the H-SOECs with Ni-BZI cathode (denoted as H^--cathode type cell) were evaluated by feeding dry H_2 gases to the cathode side for pre-reduction and steam electrolysis. The electrolysis currents and Faradaic efficiencies were compared between both cathode type cells. The results demonstrated that the currents at 1.3 V increased by 1.6 times and Faradaic efficiency increase from 80 to more than 90% by using H^--cathode.

5.2 Experimental

5.2.1. Sample preparation

$BaZr_{0.5}In_{0.5}O_{3-\delta}$ (BZI) powders were synthesized via a solid-state reaction. Stoichiometric amounts of the starting materials, including $BaCO_3$ (High Purity Chemicals; 99.95%), ZrO_2 (High Purity Chemicals; 98%), and In_2O_3 (High Purity Chemicals; 99.99%), and $Zn(NO_3)_2 \cdot 6H_2O$ (Wako Chemicals; 99.9%, Zn/BZI molar ratio, 0.01) additives as a sintering aid were ball-milled for 2 h, pressed into pellets, and calcined at 900°C for 12 h. After ball-milling, the powders were pressed again

into pellets and calcined at 1300°C for 12 h, and then finally, annealed at 1500°C for 8 h after ball-milling for 10 h and pelletizing.

PBSCF, and BLFZ powders were synthesized by a citrate precursor route, where citric acid (CA; $C_6H_7O_8 \cdot H_2O$, 99.5%, Kanto Chemical Co.) was used as a chelating agent at a molar ratio of CA : (PBSCF, BLFZ) = 2:1. The precursor solution of PBSCF and BLFZ was prepared by dissolving the required stoichiometric amounts of $Pr(NO_3)_3 \cdot nH_2O$ (99.5%, FUJIFILM Wako Pure Chemical Corporation), $Ba(NO_3)_2$ (99%, Kanto Chemical), $Sr(NO_3)_2$, $Co(NO_3)_2 \cdot 6H_2O$, $Fe(NO_3)_3 \cdot 9H_2O$ (99.9%, Wako Pure Chemical Industries), and $Ba(NO_3)_2$ (99%, Kanto Chemical), $La(NO_3)_3 \cdot 6H_2O$, $Fe(NO_3)_3 \cdot 9H_2O$ (99.9%, Wako Pure Chemical Industries), $Zn(NO_3)_2 \cdot 6H_2O$ (99.9%, FUJIFILM Wako Pure Chemical Corporation), respectively, in Milli-Q H_2O with CA. The gelatinous products were obtained by heating and stirring to evaporate H_2O and promote polymerization. The gels were calcined at 500°C for 1 h, following which the ground precursor powders were calcined at 900 and 1000°C in air for 8 h. The BLFZ powders were pelletized into a disk and subsequently sintered at 1200°C for 6 h to obtain the target for pluses laser deposition (PLD).

5.2.2. Fabrication of H-SOEC

H-SOECs with BZI thin film on porous Ni-BZI or Ni-(H-BZI) ceramet supports were fabricated using co-firing proses [1], as shown in Figure 5-1. The porous cathode was prepared by ball-milling NiO (High Purity Chemicals, 99.97%), BZI electrolyte powders, ethyl cellulose and starch with a weight ratio of 60:40:2:10, respectively, for 10 h in 2-propanol. After drying, the mixture powders were uniaxially pressed into pellets (~12 mm diameter, ~1.8 mm thickness) under 20 MPa and subsequently isostatically pressed under a hydrostatic pressure of 100 MPa. The cathode buffer layer was spin-coated on both surfaces of the porous pellets with a slurry, which was prepared by dispersing NiO and BZI (weight ratio of 60:40) into a solution containing a dispersant (20 wt.% polyethyleneimine (M_w 28 000) dissolved in α-terpineol) and a binder (5 wt.% surfactant dissolved in α-terpineol). The electrolyte layer was spin-coated on both surfaces of the cathode buffer layer with a

slurry, which was prepared by dispersing BZI powders into a solution containing a dispersant (20 wt.% polyethyleneimine dissolved in α-terpineol) and a binder (5 wt.% surfactant dissolved in α-terpineol). Subsequently, the pellet was first exposed to 350°C for 2 h and then at 1400°C for 8 h in an air atmosphere to form a half-cell. The backside of the sintered pellet was polished with SiC paper.

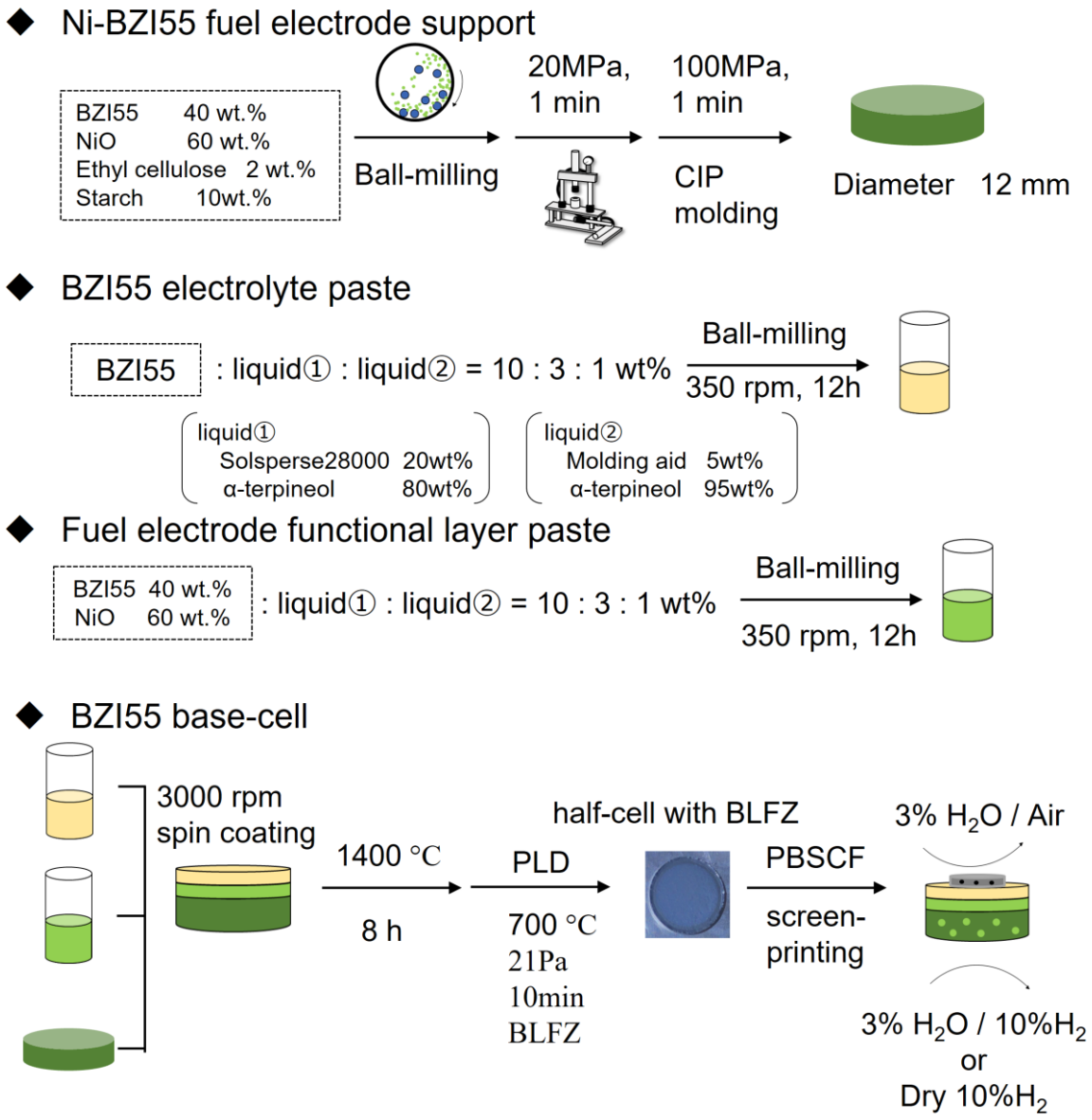

Figure 5-1. The fabrication procedures of the {Ni-BZI or Ni-(H-BZI) │BZI │BLFZ/PBSCF} cell.

$Ba_{0.95}La_{0.05}Fe_{0.8}Zn_{0.2}O_{3-\delta}$ (BLFZ) AFL were deposited for 10 min on BZI electrolyte of the half-cell using the pulsed-laser deposition (PLD) technique with an Ulvac UPS-1000S ultravacuum chamber system. The substrate temperature was set to 700°C. The oxygen partial pressure in the chamber was set to 21 Pa. A 248 nm KrF excimer laser (Coherence COMPEX 109) ablated the targets at a repetition rate of 5 Hz. The laser energy was approximately 105 mJ per a pulse. Finally, a $PrBa_{0.5}Sr_{0.5}Co_{1.5}Fe_{0.5}O_{5+\delta}$ (PBSCF) button electrode was screen-printed on the surfaces of the BLFZ films as a porous anode.

5.2.3. Characterization

The phase purity was checked by X-ray diffraction (XRD) analysis in the 2θ range between 20° and 80° at a scan rate of 5° min^{-1} using a Rigaku Ultima IV (Cu Kα radiation). The microstructures of the fabricated cells were examined using a field emission scanning electron microscope (FESEM; SIGMA500, ZEISS) operated at 5 kV.

5.2.4. Electrochemical Measurements

Steam electrolysis were conducted with a wet or dry cathode gas in order to prepare separately H^+ conducting Ni-BZI cathode cell or H^- conducting Ni-(H-BZI) cathode cell. Hereafter, these are described as H^+-cathode and H^--cathode, respectively. In the case of H-SOECs with H^+-cathode, the pre-reduction was conducted at 600°C for 6 h by supplying wet 10%-H_2/Ar (including 3% H_2O) gas to the cathode side and wet air (including 3% H_2O) to the anode side to form H^+-cathode based on a porous Ni-BZI cermet (Figure 5-3a). For H^--cathode, the pre-reduction was conducted at 800°C for 12 h by supplying dry 10%-H_2/Ar gas to the cathode side and wet air to the anode side, and then the hydrogen concentration in the cathode side was gradually increased to 50% over 30 min and kept for 1 h to obtain a Ni-(H-BZI) cermet cathode. The resultant cells with H^--cathode must consist of bilayer films of BZI electrolyte and hydrogen-permeable H-BZI cathode, as shown in Figure 5-3b, because BZI thin film near the porous Ni-(H-BZI) cermet support is reduced to H-BZI by pre-reduction.

Steam electrolysis performances was evaluated in the range of 500 to 700°C with a wet or dry 10%-H_2/Ar mixed gas to the cathode at a rate of 40 sccm and a 20%-H_2O/air to the anode at a rate of 25 sccm. The 20%-H_2O/air was prepared by passing Ar/O_2 = 8/2 (v/v) mixed gas through a water bath maintained at approximately 60°C and subsequently supplied to the anode chamber through a stainless-steel tube heated at 150°C using a ribbon heater to prevent condensation. For cells with H^+-cathode, wet 10%-H_2/Ar mixed gas (3% H_2O) was prepared by bubbling in pure water maintained at 25°C and fed to the cathode at 30 cm^3 min^{-1}. For cells with H^--cathode, dry 10%-H_2/Ar mixed gas was fed to the cathode at 30 cm^3 min^{-1}. The electrochemical measurements were carried out using a potentio/galvanostat equipped with frequency response analyzer (Biologic SP-300). The hydrogen evolution rates (v) in the cathode were quantified by analyzing the cathode exhaust gas using gas chromatography (490 Micro GC, Agilent Technologies). The Faradaic efficiency, η, was calculated using the observed and theoretical hydrogen evolution rates (v_{meas} and v_{theo}, respectively) using the following equation:

$$\eta = \frac{v_{\mathrm{meas}}}{v_{\mathrm{theo}}} \times 100 = \frac{v_{\mathrm{meas}}}{I \times (z \times F)^{-1}} \times 100\ (\%) \qquad (5\text{-}1)$$

where I is the applied current, z is the electron transport number of steam electrolysis, and F is Faraday's constant (96 485 C mol^{-1}).

5.3. Results and Discussion

5.3.1. Characterization of Prepared H-SOECs

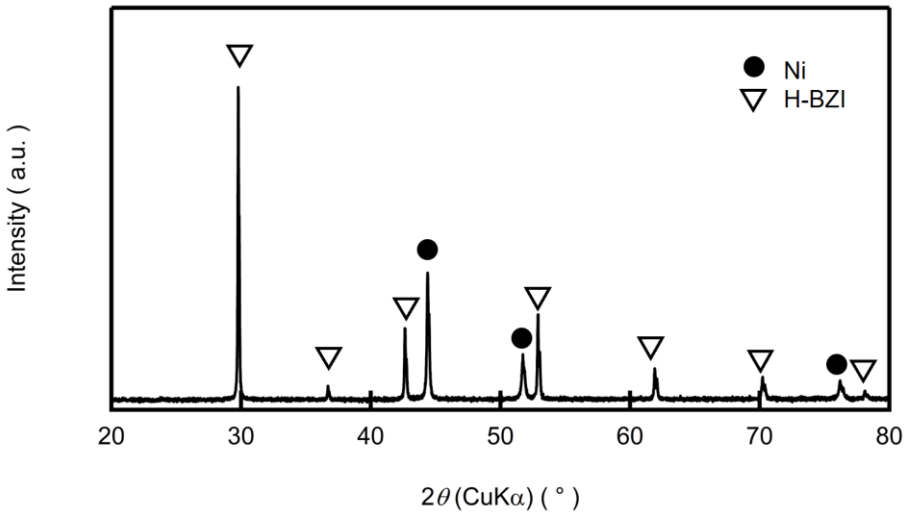

Figure 5-2. XRD pattern of pulverized half cells {Ni-(H-BZI) | H-BZI} after reduction.

Figure 5-2 shows the powder XRD pattern of pulverized half-cell after reduction by dry hydrogen at 800°C (i.e., Ni-(H-BZI)/H-BZI). All peaks were assigned to Ni and H-BZI, which confirms that the reaction between BZI and Ni is less-pronounced at elevated temperature in H_2 atmosphere. Figure 5-3a and 3b show the cross-sectional SEM images of H-SOEC with H^+- and H^--cathode, respectively, after electrolysis measurement. Both cells comprise of highly porous Ni-BZI or Ni-(H-BZI) cermet supports, porous Ni-BZI or Ni-(H-BZI) cathode buffer layer (10 μm), highly dense BZI electrolyte (10 μm), BLFZ-AFL 150 nm), and porous PBSCF anode layer. In both cells, the cermet supports are highly porous with interconnected macropore networks that act as a gas diffusion path. Highly dense BZI electrolyte films are uniformly formed over porous Ni-BZI or Ni-(H-BZI) cathode buffer layers with a thickness of about 10 μm. The BZI electrolyte layer maintains dense matrices without any cracks even after electrolysis. The PBSCF anode is a porous layer composed of ~100 nm diameter particles

with a thickness of ~100 μm. Figure 5-2c and 2d show a cross-sectional and surface SEM image of the BLFZ-AFL on the BZI thin film. The 150-nm-thick BLFZ layer, comprised of the nanoparticles with about 50 nm diameters, fully covers the electrolyte surface. The BZI grains significantly grew up to a few μm sizes in diameter.

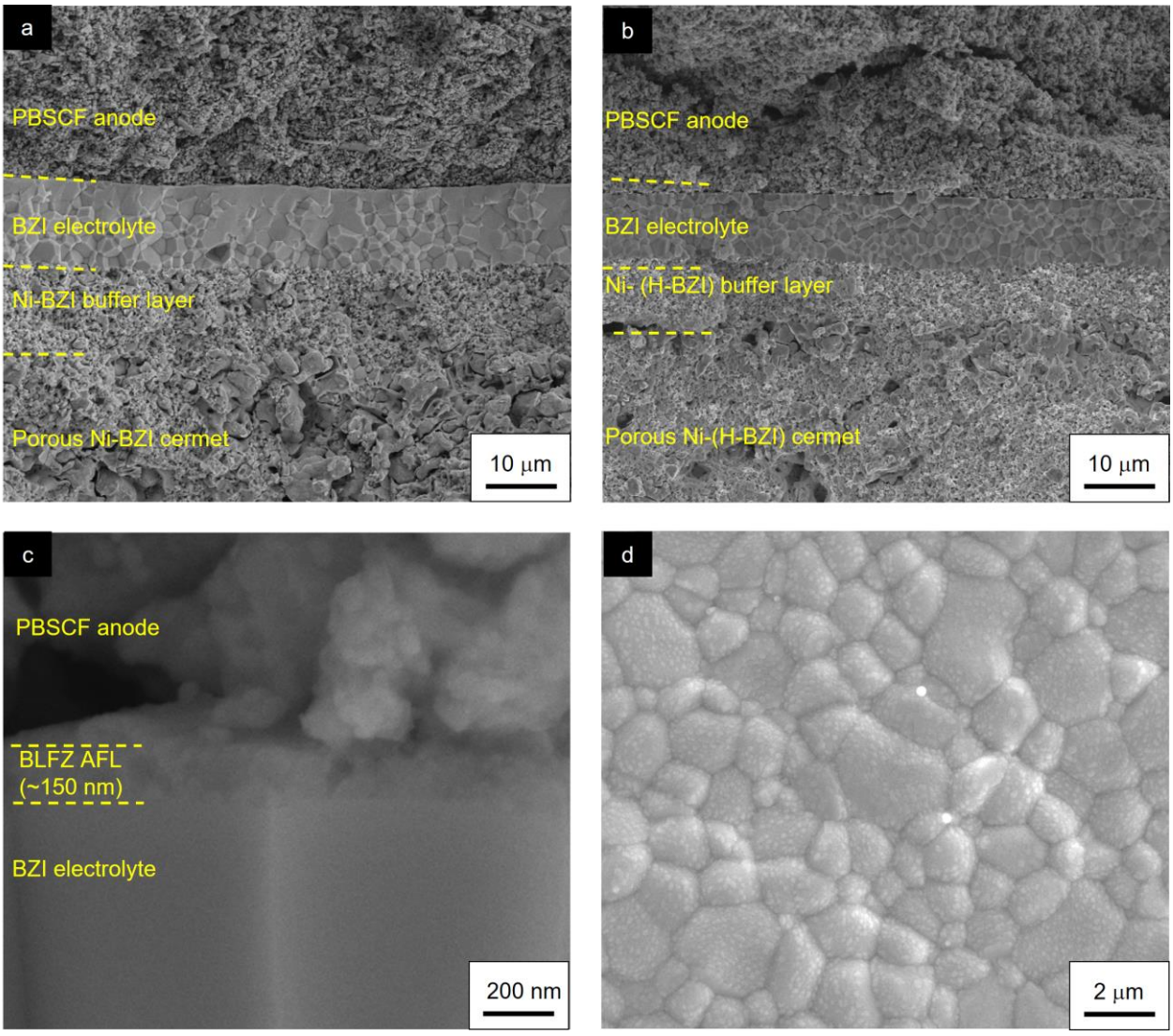

Figure 5-3. Cross-sectional SEM images of H-SOEC with (a) Ni-BZI (H^+-) and (b) Ni-(H-BZI) (H^--) cathodes after electrochemical measurement. (c) Cross-sectional and (d) surface SEM images of BLFZ-AFL deposited on BZI electrolyte.

5.3.2. Electrochemical Measurements

Figure 5-4a shows the current–voltage (*I–V*) curves for the H-SOEC with H^+-cathode, i.e., {20%-H_2O/20%-O_2/Ar, PBSCF | BLFZ/BZI (10 μm) | Ni-BZI, wet 10%-H_2/Ar}, measured in the range of 700-500°C. Open circuit voltage (OCV) at 600 and 500°C are 0.95 and 0.99 V, respectively, which is slightly lower than the ideal value of 0.97 and 1.00 V calculated by the Nernst equation, probably due to the partial hole conductivity of BZI. The H-SOEC with H^+-cathode exhibited electrolysis currents of 1.14 and 0.56 A cm^{-2} by 1.3 V bias at 600 and 500°C, respectively. Figure 5-4b shows the current–voltage (*I–V*) curves for the H-SOEC with H^--cathode, i.e., {20%-H_2O/20%-O_2/Ar, PBSCF | BLFZ/BZI (10 μm) | Ni-(H-BZI), dry 10%-H_2/Ar}, in the range of 700-500°C. OCV at 600 and 500°C are measured to be 0.93 and 0.98 V, respectively, which is comparable to the results of the cells with H^+-cathode. However, the OCV of the H-SOEC was significantly lower than that of the H-SOEC with H^+-cathode at temperature above 650°C. The electrolysis currents of H-SOEC with H^--cathode at 600 and 500°C are 1.68 and 0.84 A cm^{-2} at 1.3 V, respectively, which are higher than the corresponding values of the H-SOEC. The electrolysis current of H-SOEC with H^--cathode at 600°C is much higher than those of the previously reported H-SOEC with Zr-rich side electrolyte [2-12] (Figure 5-5).

Figure 5-4c and 4d show the AC impedance spectra for H-SOEC with H^+ and H^--cathode, respectively, measured under the OCV condition in the temperature range from 500°C to 700°C. The high frequency *x* intercept is normally attributed to the electrolyte's ohmic resistances (R_O), while the succeeding arcs denote the interfacial polarization mainly because of the anode reactions [15]. The polarization resistances (R_p) are approximated using the total diameter of the impedance arcs. The R_O of the cells with H^+- and H^--cathode at 500°C are 0.40 Ω cm^2 and 0.27 Ω cm^2 under OCV conditions, respectively. R_O of the H-SOEC with H^--cathode is apparently lower than that with H^+-cathode. This feature could be attributed to the reduction of nominal thickness of BZI electrolyte, because BZI electrolyte films near the Ni–(H-BZI) cermet layer is converted to H-BZI membrane electrode by the pre-reduction treatment (Figure 5-6).

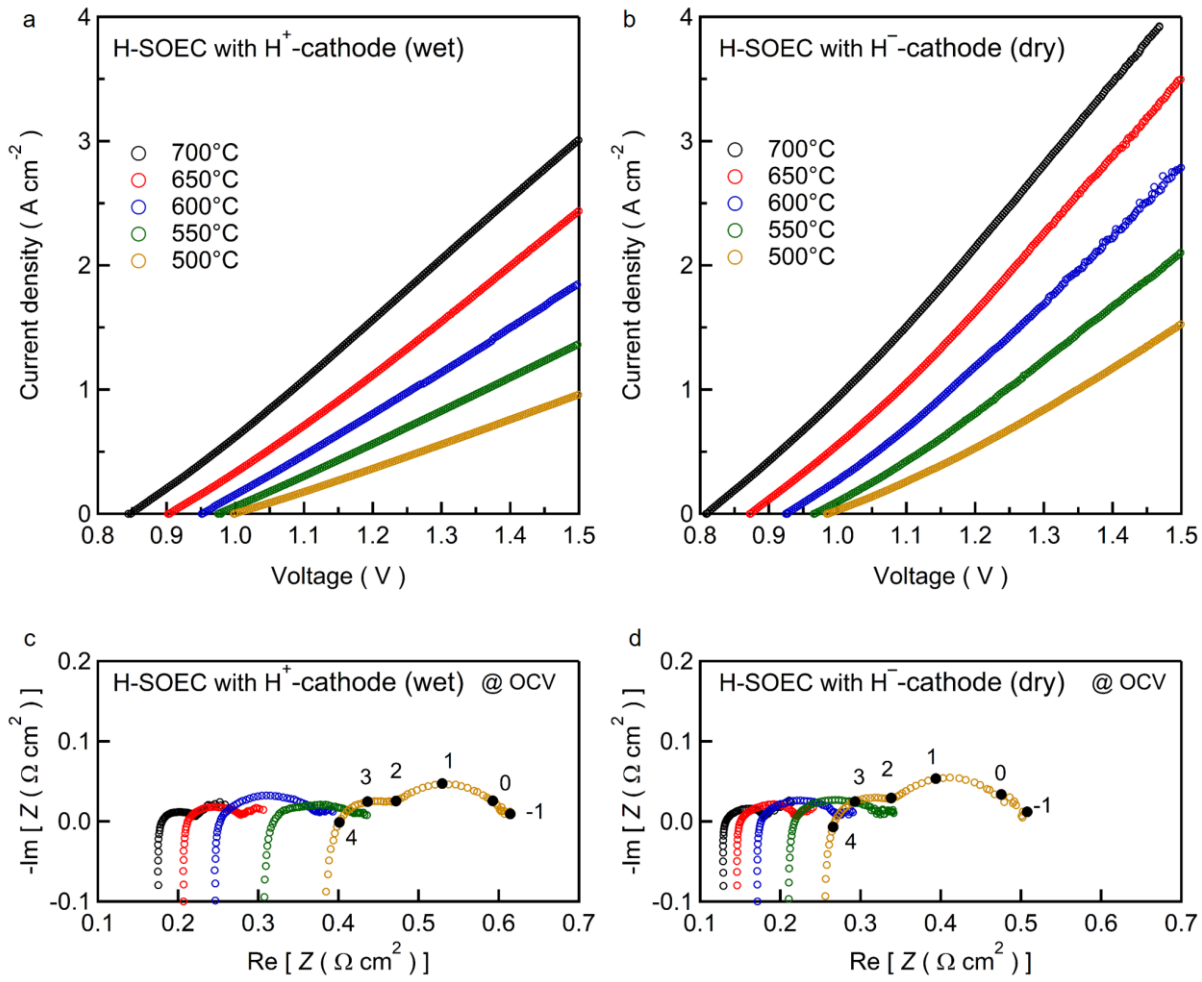

Figure 5-4. The current–voltage (*I–V*) curves for the H-SOEC with (a) H^+- and (b) H^--cathode, i.e., {20%-H_2O/20%-O_2/Ar, PBSCF | BLFZ/BZI (10 μm) | Ni-BZI, wet 10%-H_2/Ar} and {20%-H_2O/20%-O_2/Ar, PBSCF | BLFZ/BZI (10 μm) | Ni-(H-BZI), dry 10%-H_2/Ar}, respectively, measured in the range of 700-500°C. The AC impedance spectra for H-SOEC with (c) H^+- and (d) H^--cathode, respectively, measured under the OCV condition in the temperature range from 500°C to 700°C.

On the other hand, the R_p of the cell with H^--cathode (0.23 Ω cm^2) is very close to that of the cell with H^+-cathode (0.21 Ω cm^2). In the H-SOEC with H^--cathode, the cathode reaction is featured by the conversion to H^- ions with association of H^+ and electrons at the electrolyte/cathode interface, and the subsequent diffusion of H^- ion in H-BZI membrane electrode (Figure 5-7). The impedance arcs of both type H-SOECs are in good agreement with each other, as shown in Figure 5-8, confirming that additional arcs do not appear with a use of H^--cathode. These results reveals that the resistances related to H^- defect formation and diffusion in H-BZI membranes are quite small.

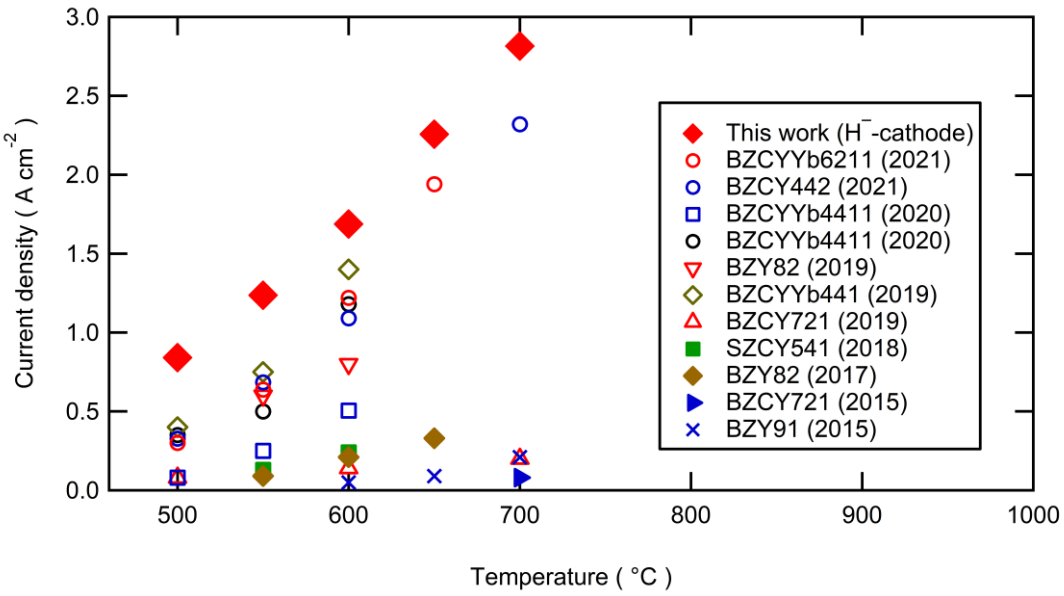

Figure 5-5. Comparison of the electrolysis current density of H-SOECs with Zr-rich side electrolytes at the thermal neutral point [2-12].

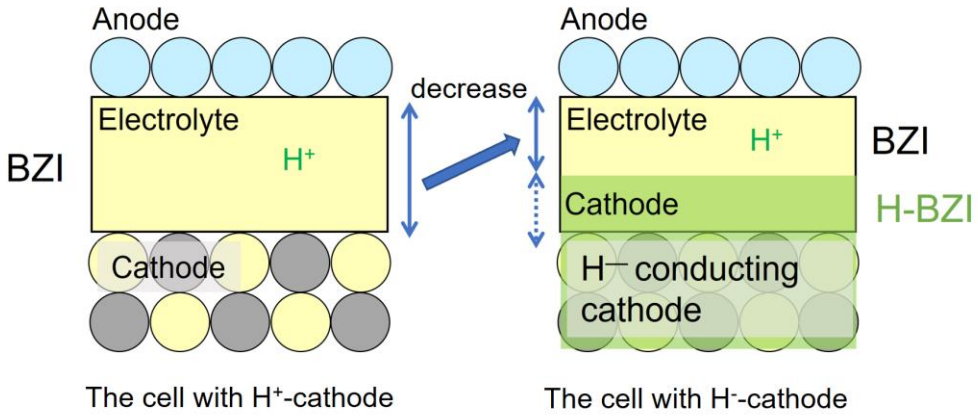

Figure 5-6. Schematic diagram of decrease in electrolyte thickness from the cell with H^+-cathode (left) to H^--cathode (right) by hydrogenation.

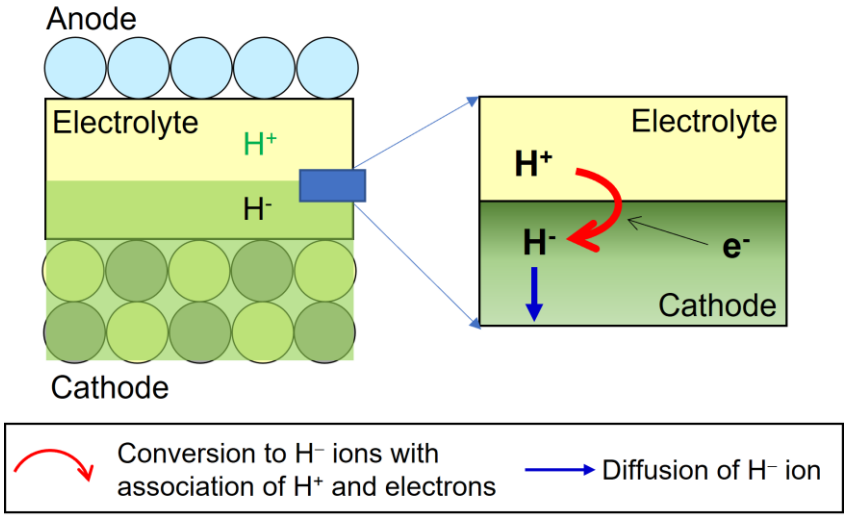

Figure 5-7. Schematic diagram of the reactions associated with hydride ions on the cathode side

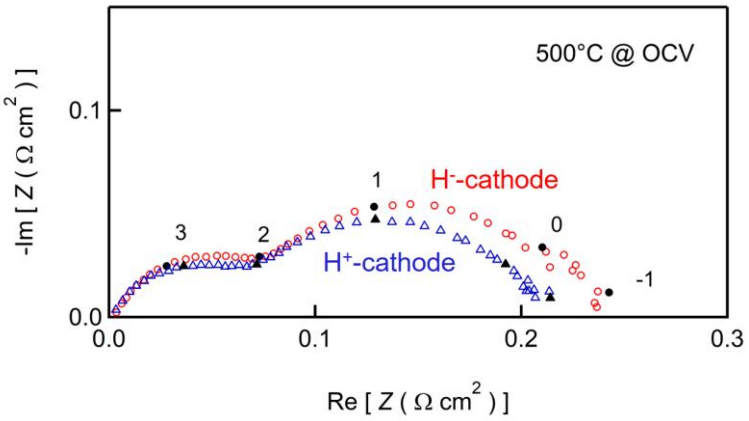

Figure 5-8. Comparison of polarization resistances between H-SOEC with H^+-cathode (blue triangle) and H^--cathode (red circle).

5.3.3. Faradaic Efficiency

The hydrogen production rate was calibrated using gas chromatography at 500°C under galvanostatic electrolysis at 600 mA cm^{-2}. Figure 5-8 illustrates the transients of the cell voltage, hydrogen evolution rate (v_{meas}), and Faradaic efficiency (η) under the galvanostatic electrolysis at 600 mA cm^{-2} for 4h at 500°C. The voltages for H-SOEC with H^+- and H^--cathode are stable at around 1.34 and 1.26 V, respectively. The nominal overpotentials, defined by the gap between the cell bias and the OCV, are equal to 0.35 and 0.28 for H^+- and H^--cathode cells, respectively.

H-SOEC with H^+-cathode acquires v_{meas} of about 1.4×10^{-4} mol cm^{-2} min^{-1} and η values of 73% for electrolysis at 500°C in 600 mA cm^{-2}. H-SOEC with H^--cathode gains v_{meas} and η equal to 1.6×10^{-4} mol cm^{-2} min^{-1} and 85%, respectively, in the same electrolysis condition, both of which are larger than those of the cell with H^+-cathode by at least 10%. Furthermore, this value is much larger than the previously results on the H-SOECs conducted under atmospheric conditions [8-16] (Figure 5-9). These results verify that H-SOEC based on an ionic heterojunction of an H^- ion-conducting cathode and H^+ conducting electrolyte can conduct highly efficient hydrogen production by steam electrolysis. The Hydrogen-permeable, H^- ion-conducting membrane cathodes can suppress the formation of hole

carriers in the adducent BZI electrolyte layer because $V_O^{\bullet\bullet}$ defects are accumulated near BZI/H-BZI interfaces sue to the very low p_{O2} at the cathode side (details are described in chapter 1).

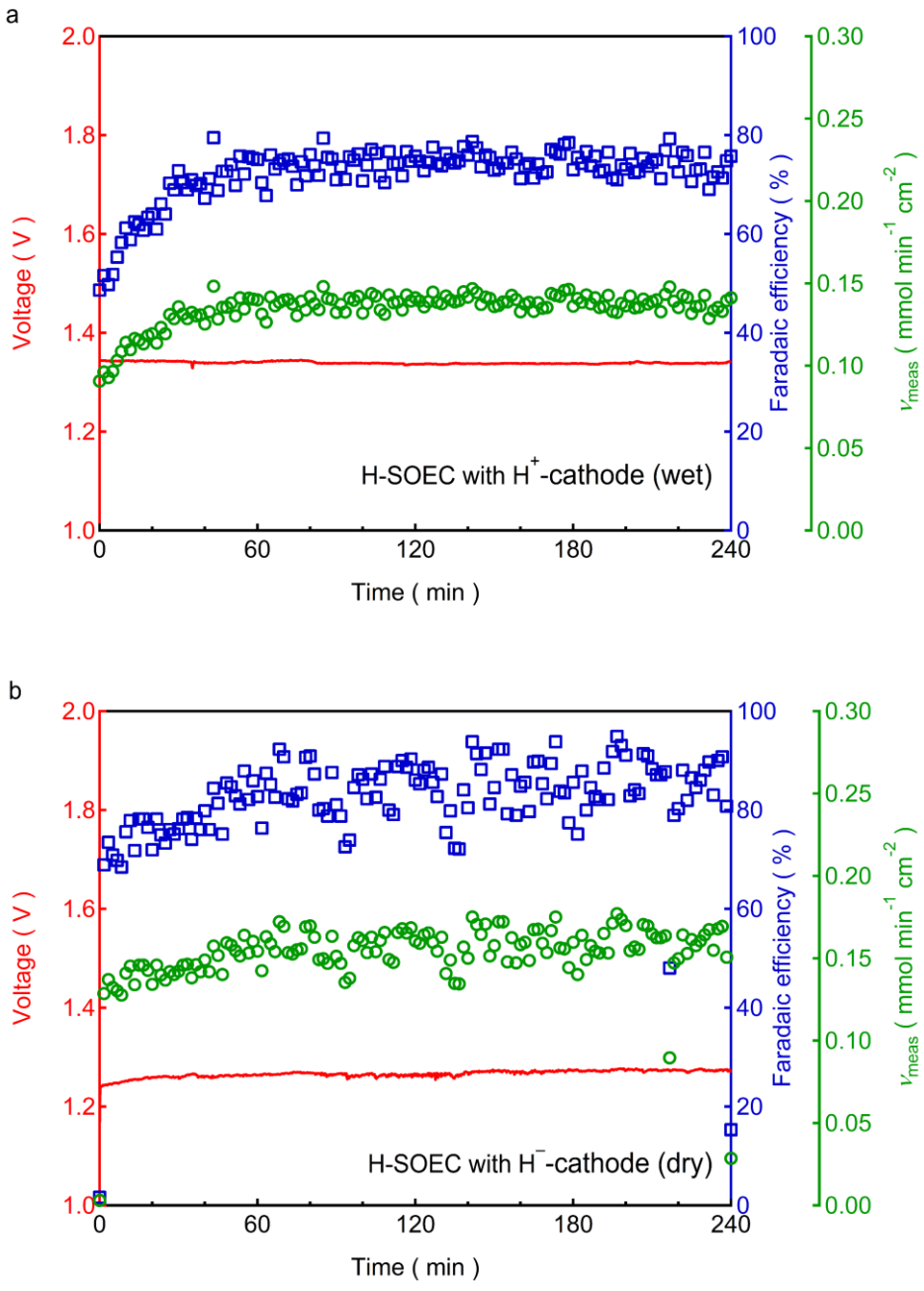

Figure 5-9. Faradaic efficiency (η) (blue, □), hydrogen evolution rate (v_{meas}) (green, ○) and cell voltage (red line) of H-SOEC with (a) H^+- and (b) H^--cathode, i.e., {20%-H_2O/20%-O_2/Ar, PBSCF | BLFZ/BZI (10 μm) | Ni-BZI, wet 10%-H_2/Ar} and {20%-H_2O/20%-O_2/Ar, PBSCF | BLFZ/BZI (10 μm) | Ni-(H-BZI), dry 10%-H_2/Ar}, respectively, measured at 500°C under galvanostatic conditions at 600mA cm^{-2}.

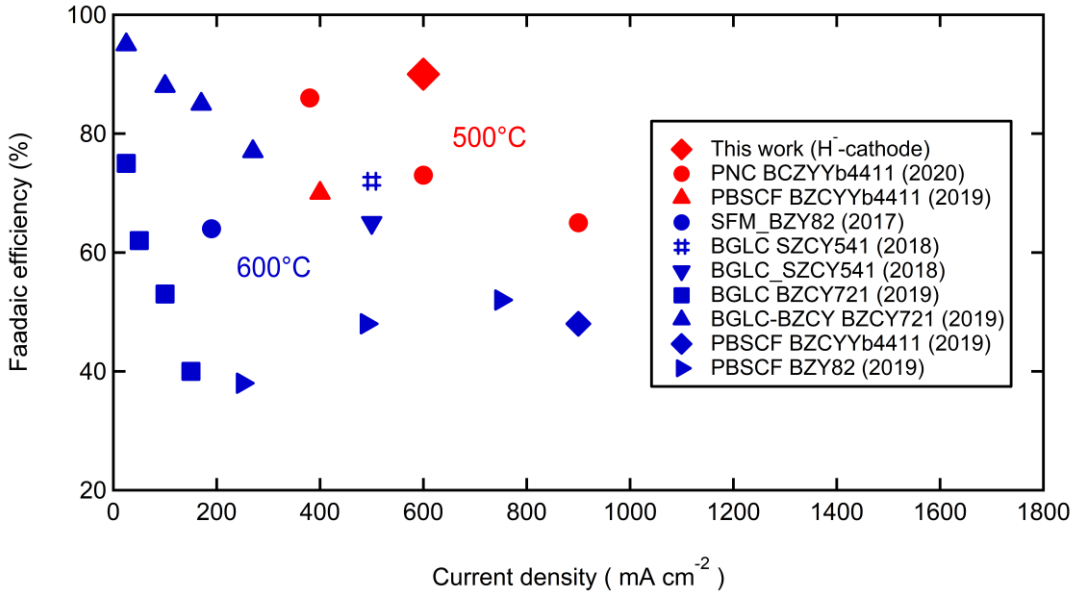

Figure 5-9. Comparison of the Faradaic efficiency of H-SOECs with Zr-rich side BZCM electrolytes [8-13].

5.4. Conclusions

H-SOEC with hydride ion electron mixed conducting H-BZI cathode was successfully fabricated by ceramic sintering process and post-treatment in dry hydrogen atmosphere. The H-SOECs with H^--cathode, having the configuration of {PBSCF | BLFZ/BZI (10 μm) | Ni-(H-BZI)}, yield the electrolysis currents of 1.68 and 0.84 A cm^{-2} at 600 and 500°C under 1.3 V, respectively. These values are higher than those of the H-SOEC with H^+-cathode, i.e., {PBSCF | BLFZ/BZI (10 μm) | Ni-BZI}, and moreover, higher than the previous results for cells with Zr-rich side $BaZr_xCe_{1-x-y}M_yO_{3-\delta}$ electrolyte. The H^--cathode cells achieved Faradaic efficiency of over 85% at 500°C under the current density of 600 mA cm^{-2}, which is the highest value of H-SOEC under atmospheric conditions. These results suggest that H-SOEC comprising an ionic heterojunction of an H^- ion-conducting cathode and H^+ conducting electrolyte can conduct efficiently steam electrolysis with small hole leakage. The current results provide a new strategy to develop H-SOECs with the efficiency equaling to 100%.

5.5. References

1. An, H., Lee, H. W., Kim, B. K., Son, J. W., Yoon, K. J., Kim, H., *et al.* A 5× 5 cm^2 protonic ceramic fuel cell with a power density of 1.3 W cm^{-2} at 600° C. *Nature Energy*, *3*(10), 870-875 (2018).
2. Bi, L., Shafi, S. P., & Traversa, E. Y-doped $BaZrO_3$ as a chemically stable electrolyte for proton-conducting solid oxide electrolysis cells (SOECs). *Journal of Materials Chemistry A*, *3*(11), 5815-5819 (2015).
3. Duan, C., Kee, R., Zhu, H., Sullivan, N., Zhu, L., Bian, L., *et al.* Highly efficient reversible protonic ceramic electrochemical cells for power generation and fuel production. *Nature Energy*, *4*(3), 230-240 (2019).
4. Babiniec, S. M., Ricote, S., & Sullivan, N. P. Characterization of ionic transport through $BaCe_{0.2}Zr_{0.7}Y_{0.1}O_{3-\delta}$ membranes in galvanic and electrolytic operation. *International Journal of Hydrogen Energy*, *40*(30), 9278-9286 (2015).
5. Zhu, L. L., Huang, Y. E., Gong, L. K., Huang, X. Y., Qi, X. H., Wu, X. H., & Du, K. Z. Ligand Control of Room-Temperature Phosphorescence Violating Kasha's Rule in Hybrid Organic–Inorganic Metal Halides. *Chemistry of Materials*, *32*(4), 1454-1460 (2020).
6. Wang, N., Toriumi, H., Sato, Y., Tang, C., Nakamura, T., Amezawa, K., *et al.* $La_{0.8}Sr_{0.2}Co_{1-x}Ni_xO_{3-\delta}$ as the Efficient Triple Conductor Air Electrode for Protonic Ceramic Cells. *ACS Applied Energy Materials*, *4*(1), 554-563 (2020).
7. Tang, C., Akimoto, K., Wang, N., Fadillah, L., Kitano, S., Habazaki, H., & Aoki, Y. The effect of an anode functional layer on the steam electrolysis performances of protonic solid oxide cells. *Journal of Materials Chemistry A*, *9*(24), 14032-14042 (2021).
8. Vøllestad, E., Strandbakke, R., Tarach, M., Catalán-Martínez, D., Fontaine, M. L., Beeaff, D., *et al.* Mixed proton and electron conducting double perovskite anodes for stable and efficient tubular proton ceramic electrolysers. *Nature Materials*, *18*(7), 752-759 (2019).
9. Ding, H., Wu, W., Jiang, C., Ding, Y., Bian, W., Hu, B., *et al.* Self-sustainable protonic ceramic electrochemical cells using a triple conducting electrode for hydrogen and power production. *Nature Communications*, *11*, 1907 (2020).
10. Leonard, K., Okuyama, Y., Takamura, Y., Lee, Y. S., Miyazaki, K., Ivanova, M. E., *et al.* Efficient intermediate-temperature steam electrolysis with Y: $SrZrO_3$–$SrCeO_3$ and Y: $BaZrO_3$–$BaCeO_3$ proton conducting perovskites. *Journal of Materials Chemistry A*, *6*(39), 19113-19124 (2018).
11. Lei, L., Tao, Z., Wang, X., Lemmon, J. P., & Chen, F. Intermediate-temperature solid oxide electrolysis cells with thin proton-conducting electrolyte and a robust air electrode. *Journal of Materials Chemistry A*, *5*(44), 22945-22951 (2017).
12. Choi, S., Davenport, T. C., & Haile, S. M. Protonic ceramic electrochemical cells for hydrogen

production and electricity generation: exceptional reversibility, stability, and demonstrated faradaic efficiency. *Energy & Environmental Science*, *12*(1), 206-215 (2019).

13. Leonard, K., Druce, J., Thoreton, V., Kilner, J. A., & Matsumoto, H. Exploring mixed proton/electron conducting air electrode materials in protonic electrolysis cell. *Solid State Ionics*, *319*, 218-222 (2018).

Chapter 6

General Conclusion

This thesis aims to design the anode and cathode materials of H-SOECs for significantly improving the Faradaic efficiency of H-SOECs. The hole carriers of H^+-conducting BZCM electrolytes has been known to increase with increasing the potentials and/or p_{O2} at the anode side, and its migration lower the Faradaic efficiency. Hence the lowered Faradaic efficiency is fatal issue for BZCM base H-SOECs. This feature is more evident in the high Zr-content BZCM than in the high Ce-content one, despite the former being desirable for H-SOEC applications due to excellent tolerance to humidity atmosphere. First, I attempted to develop new anode material with enhanced hydration capability. The anode reaction area can be extended to overall the surface of anodes by applying such materials, which results in decreasing the anode overpotential, thereby hole leakage. Second, I aimed to develop a new cathode involving hydrogen permeability by H^- ion electron mixed conductivity. Such a cathode is expected to decrease significantly both p_{O2} and p_{H2O} in the adjacent BZCM layer so that lower the hole leakage current. The primary achievements of this thesis were summarized as follows.

In chapter 1, the climate change issue was outlined, and the significance of hydrogen energy in a low-carbon society were described. Finally, the chapter also proposed the advantages and feasibility of high-temperature steam electrolysis and clarified the issues of H-SOEC. Finally, the objectives and approaches of this study were described.

In chapter 2, H-SOECs consisting of $BaZr_{0.6}Ce_{0.2}Y_{0.2}O_{3-\delta}$ (BZCY622) dense electrolyte thin films was evaluated in terms of Faradaic efficiency. The thin film cells with porous cermet supports were prepared by a reactive sintering at a relatively low sintering temperature (1400°C) with $Zn(NO_3)_2$ as a sintering aid. The Faradaic efficiency was limited at around 60%, although the current density increased by 2 times with a use of $La_{0.5}Sr_{0.5}CoO_{3-\delta}$ (LSC) functional layer (AFL, ~60 nm) at the anode/electrolyte interface.

In chapter 3, I attempted to develop a new anode with partial proton conductivity to reduce the cathode overpotential and decrease thereby the hole concentration near the anode/electrolyte interface. It is known that p-type semiconductors with O 2*p* hole carriers are generally effective for the oxygen-evolution reaction, and high valence state transition metal oxides are suitable for generation of O 2*p* holes. Moreover, the oxides with partial proton conduction are advantageous for the H-SOEC anode because they increase the proton-accessible electrode area. $Ba_3Mn_2O_8$ ($Ba_3(MnO_4)_2$) is a high-valent Mn(V) oxide and has a structure that is similar to the scheelite type structure of proton conducting $LaTaO_4$. Based on these I evaluated $Ba_3(MnO_4)_2$ anodes for H-SOECs. $Ba_3(MnO_4)_2$ was found to have relatively large negative hydration enthalpy equaling −140 kJ mol^{-1}, which is similar to the value of most famous proton conductor $BaCe_{0.9}Y_{0.1}O_{3-\delta}$. exhibited the proton uptake of 0.2 mole fraction by hydration in the temperatures below 670°C in 3%-H_2O/air, which suggested that it had a partial proton conductivity. Therefore, a bulk cell was fabricated using $BaZr_{0.4}Ce_{0.4}Y_{0.2}O_{3-\delta}$ (BZCY442) sinter electrolyte and $Ba_3(MnO_4)_2$ composite anode with n-type $Sn_{0.95}Sb_{0.05}O_{2-\delta}$ conductive fillers. Compared to representative O^{2-}/e^- conducting $Sm_{0.5}Sr_{0.5}CoO_{3-\delta}$, the $Ba_3(MnO_4)_2$ composite anodes exhibited small polarization resistance at 700°C, confirming that the composite electrode was active as an anode of H-SOECs. Further electrochemical analysis verified that the pronounced activity was originated from the charge transfer catalytic activity of the high valence Mn(V) and the extension of the reaction areas by partial proton conductivity. Meanwhile, the Faradaic efficiency remained at around 75% with $Ba_3(MnO_4)_2$ anode, which provided a conclusion that it was difficult to depress the holes only by reducing anode overpotential.

Alternatively, the importance of H^- ion-conducting cathode was argued in chapter 4 and 5. Steam electrolysis could be performed by feeding a dry hydrogen gas to the cathode side, when the Ni-BZCM cermet cathode was replaced by the hydrogen permeable solid electrodes that was capable of reversible intake/release of hydrogen gas. In this case, p_{O2} at cathode/electrolyte interfaces must be extensively decreased because the oxygen vacancies are accumulated near the interface and water vapor were not

supplied at the cathode side. Hence Faradaic efficiency is expected to increase due to formation of hole depletion layer in electrolyte near the cathode.

In chapter 4, a H^- ion electron mixed conductor was explored for a potential hydrogen permeable cathode of H-SOECs. Though the broad survey of perovskite materials, $BaZr_{0.5}In._{0.5}O_{3-\delta}$ (BZI) was found to transformed to isomorphous $BaZr_{0.5}In(II)_{0.5}O_{2.25}H_{0.5}$ (hereafter H-BZI) oxyhydride upon heating in dry hydrogen at 800°C. The precise composition and structures of the oxyhydride were investigated by means of Neutron diffraction structure refinement, and the In valence state was confirmed by EXAFS and ESR analysis. H-BZI exhibited clear electronic conduction due to the hole hoping between In(II) and In(III) state. Combined electrochemical measurements and EXAFS local structure analysis revealed that the H^- ion occupying oxide anion site can be diffusive by hopping along the nearest neighbor path because of the oxygen deficiency equaling the threshold of 0.75 mole fraction. Thus, H-BZI membranes supported on porous Ni-(H-BZI) cermet exhibited remarkable hydrogen permeance at temperatures above 500°C, which was larger than those of the proton conducting (BS)ZCM base membranes at least by 3 times.

In chapter 5, I demonstrated high Faradaic efficiencies of the H-SOECs with H^- ion electron mixed conducting H-BZI cathodes. The thin film cells comprising BZI thin film supported on a porous NiO-BZI cathode supports and $PrBa_{0.5}Sr_{0.5}Co_{1.5}Fe_{0.5}O_{5+\delta}$ (PBSCF) anode were fabricated by conventional sintering process. H^+ conducting Ni-BZI cermet cathode type cells were prepared by the prereduction of NiO to Ni in the cathode at 600°C in wet H_2 atmosphere, and thus evaluated by feeding wet 10%-H_2/Ar gases to the cathode side. The cells gained Faradaic efficiency of 73% under galvanostatic current of 0.6 A cm^{-2} and currents of 0.56 A cm^{-2} under 1.3 V biasing at 500°C. On the other hand, H^--conducting Ni-(H-BZI) cathode type cells were prepared by the pre-hydrogenation treatment of NiO-BZI cathodes at 800°C in dry H_2 atmosphere, and thus the performances were evaluated by feeding dry 10%-H_2/Ar gases to the cathode side. The resultant cells yielded Faradaic efficiency of 85% under galvanostatic current of 0.6 A cm^{-2} and currents of 0.84 A cm^{-2} under 1.3 V biasing at 500°C, which was ~10% larger than that of H^+ conducting cathode cells. These results proved that the hole carriers

sufficiently depressed near the electrolyte/cathode by applying H^- ion electron mixed conducting H-BZI cathode.

In conclusion, it was demonstrated that the efficiency of H-SOECs can be significantly improved by the design of a hydrogen permeable membrane cathode support structure. The author believes that the findings in this thesis and future elucidation of the H^- ion/H^+ heterojunction will provide new design principles for H^- ion-conducting hydrogen permeable membranes and heterojunction H-SOECs. Furthermore, the author hopes these will provide knowledge that plays a crucial role in increasing the efficiency of future advanced H-SOECs.

List of Publications

1. H. Toriumi, T. Kobayashi, S. Hinokuma, T. Ina, T. Nakamura, K. Amezawa, C. Zhu, H. Habazaki, Y. Aoki "High-valence-state manganate (v) $Ba_3Mn_2O_8$ as an efficient anode of a proton-conducting solid oxide steam electrolyzer" *Inorganic Chemistry Frontiers* **2019**, 6, 1587–1597.
2. H. Toriumi, S. Jeong, S. Kitano, H. Habazaki, Y. Aoki, "Enhanced Performance of Protonic Solid Oxide Steam Electrolysis Cell of Zr-Rich Side $BaZr_{0.6}Ce_{0.2}Y_{0.2}O_{3-\delta}$ Electrolyte with an Anode Functional Layer" *ACS omega*, **2022**, 7, 9944–9950.
3. H. Toriumi, G. Kobayashi, T. Saito, T. Kamiya, T. Sakai, T. Nomura, S. Kitano, H. Habazaki, Y. Aoki, "Barium Indate-Zirconate Perovskite Oxyhydride with Enhanced Hydride-Ion/Electron Mixed Conductivity" *Chemistry of Materials,* (accepted)

Other Publications

1. N. Wang, S. Hinokuma, T. Ina, H. Toriumi, M. Katayama, Y. Inada, C. Zhu, H. Habazaki, Y. Aoki, "Incorporation of bulk proton carriers in cubic perovskite manganite driven by interplays of oxygen and manganese redox", Chemistry of Materials, **2019**, 31, 8383-8393.
2. N. Wang, H. Toriumi, Y. Sato, C. Tang, T. Nakamura, K. Amezawa, S. Kitano, H. Habazaki, Y. Aoki, "$La_{0.8}Sr_{0.2}Co_{1-x}Ni_xO_{3-\delta}$ as efficient triple conductor air electrodes for protonic ceramic cells" *ACS Applied Energy Materials*, **2021**, 4, 554–563.
3. M. Saito, C. Kura, H. Toriumi, S. Hinokuma, T. Ina, H. Habazaki, Y. Aoki, "Formation of Mobile Hydridic Defects in Zirconium Nitride Films with n-Type Semiconductor Properties" *ACS Appl. Electron. Mater.*, **2021**, 3, 3980–3989.
4. Y. Aoki, K. Takase, H. Kiuchi, Y. Sato, H. Toriumi, S. Kitano, D. Kowalski, H. Habazaki, "In-situ activation of a manganese perovskite oxygen reduction catalyst in concentrated alkaline media" *J. Am. Chem. Soc.*, **2021**, 143, 6505–6515.

Acknowledgements

Foremost, I would like to express my sincere gratitude to my supervisor: Associate Professor Yoshitaka Aoki. I have received the opportunity to carry out research with him for six years in the Laboratory of Interfacial Electrochemistry. Thanks to his continuous supervision, fruitful discussion, and hearty encouragement, I could accomplish several works and finalize this thesis.

I also gratefully acknowledge my dissertation committees: Professor Hiroki Habazaki, Professor Kiyoharu Tadanaga and Professor Kei Murakoshi for their thoughtful reviews on this thesis and valuable discussion, which helped improve the quality of the thesis.

I sincerely appreciate Professor Hiroki Habazaki, Professor Emeritus Masahiro Seo, Professor Chunyu Zhu, and Assistant Professor Sho Kitano. Thanks to their kind help, useful advice and discussion, the present research could be accomplished.

I am genuinely grateful to Professor Genki Kobayashi (Institute for Molecular Science) and Dr. Satoshi Hinokuma (National Institute of Advanced Industrial Science and Technology) for their kind teaching of analysis of neutron refinement and XAFS, respectively, and valuable discussion.

My thanks are also extended to all the members of Laboratory of Interfacial Electrochemistry who helped me and made my research life so enjoyable; Dr. Damian Kowalski, Dr. Aikira Koyama, Dr. Katsutoshi Nakayama, Dr. Chiharu Kura, Dr. SeongWoo Jeong, Dr. Yuki Sato, Kazumasa Kikutani, Taisei Kobayashi, Tomoyuki Yamaguchi, Atsushi Kasuga, Kentaro Takase, Keisuke Wada, Tomohiro Inoue, Xiangjun Shen, Miku Saito, Manami Takata, Hikaru Kobayashi, Naofumi Yamada, Cheong Kim, Laras Fadillah, Ning Wang, Chunmei Tang, Ruijie Zhu, Shinichi Nishimura, Naohiro Hasuo, Tatsuyuki Takano, Junpei Ikeura, Kensuke Sakuraba, Katsuya Akimoto, Randrianasolo Falitiana, Masahiro Nishimoto, Ryota Yamamoto, Takahiro Mori, Yuta Yato, Daisuke Endo, Naoki Kamitani, Reiko Takusari, Shuya Fujita, Xiong Zetao, JaeWon Jeon, Kai Shuto, Takuya Takahashi, Mikio Nagae, Hiroya Motohashi, Hisato Matsuya, Ryosuke Maeda, Tomoomi Eguchi, Yuta Nagasaka, Keita

Nishizawa, Yoko Iwata, Miki Oda, Yukako Yamashita, Midori Mizuki, Mariko Tone and all intern students. All students and professors who met at conferences discussed my research sincerely.

Special thanks are expressed to my seniors; Dr. Chiharu Kura, Taisei Kobayashi, Tomoyuki Yamaguchi, Dr. Akira Koyama, Dr. Ning Wang, Dr. Cheong Kim, Dr. SeongWoo Jeong, Dr. Yuki Sato and my doctoral colleagues; Chunmei Tang, Ruijie Zhu, for their kind help and useful discussion.

I would like to deeply acknowledgement the financial supports by Japan Society for the Promotion of Science for young scientists (Grant-in-Aid for JSPS fellow) and Mistry of Education, Culture, Sports, Science and Technology (MEXT).

I would like to spend the last section on my personal gratitude to my family for their constant support.